

Nitrogen line spectroscopy in O-stars

II. Surface nitrogen abundances for O-stars in the Large Magellanic Cloud ^{★,★,★}

J.G. Rivero González¹, J. Puls¹, F. Najarro², and I. Brott³

¹ Universitätssternwarte München, Scheinerstr. 1, 81679 München, Germany, e-mail: jorge@usm.uni-muenchen.de

² Centro de Astrobiología, (CSIC-INTA), Ctra. Torrejón a Ajalvir km 4, 28850 Torrejón de Ardoz, Spain

³ University of Vienna, Department of Astronomy, Türkenschanzstr. 17, 1180 Vienna, Austria

Received; Accepted

ABSTRACT

Context. Nitrogen is a key element to test the impact of rotational mixing on evolutionary models of massive stars. Recent studies of the nitrogen surface abundance in B-type stars within the *VLT-FLAMES survey of massive stars* have challenged part of the corresponding predictions. To obtain a more complete picture of massive star evolution, and to allow for further constraints, these studies need to be extended to O-stars.

Aims. In this paper, we investigate the N IV λ 4058 emission line formation, provide nitrogen abundances for a substantial O-star sample in the Large Magellanic Cloud, and compare our (preliminary) findings with recent predictions from stellar evolutionary models.

Methods. Stellar and wind parameters of our sample stars are determined by line profile fitting of hydrogen, helium and nitrogen lines, exploiting the corresponding ionization equilibria. Synthetic spectra are calculated by means of the NLTE atmosphere/spectrum synthesis code *FASTWIND*, using a new nitrogen model atom. We derive nitrogen abundances for 20 O- and 5 B-stars, by analyzing all nitrogen lines (from different ionization stages) present in the available optical spectra.

Results. The dominating process responsible for emission at N IV λ 4058 in O-stars is the strong depopulation of the lower level of the transition, which increases as a function of \dot{M} . Unlike the N III triplet emission, resonance lines do not play a role for typical mass-loss rates and below. We find (almost) no problem in fitting the nitrogen lines, in particular the ‘f’ features. Only for some objects, where lines from N III/N IV/N V are visible in parallel, we need to opt for a compromise solution.

For five objects in the early B-/late O-star domain which have been previously analyzed by different methods and model atmospheres, we derive consistent nitrogen abundances. The bulk of our sample O-stars seems to be strongly nitrogen-enriched, and a clear correlation of nitrogen and helium enrichment is found. By comparing the nitrogen abundances as a function of $v \sin i$ (‘Hunter-plot’) with tailored evolutionary calculations, we identify a considerable number of *highly* enriched objects at low rotation.

Conclusions. Our findings seem to support the basic outcome of previous B-star studies within the *VLT-FLAMES survey*. Due to the low initial abundance, the detection of strong Nitrogen enrichment in the bulk of O-stars indicates that efficient mixing takes place already during the very early phases of stellar evolution of LMC O-stars. For tighter constraints, however, upcoming results from the *VLT-FLAMES Tarantula survey* need to be waited for, comprising a much larger number of O-stars that will be analyzed based on similar methods as presented here.

Key words. stars: early-type - stars: abundances - line: formation - stars: atmospheres - stars: winds, outflows

1. Introduction

One of the main products of the *VLT-FLAMES survey* of massive stars¹ (hereafter *FLAMES I*) was the determination of light element abundances from statistically significant samples of Galactic, Large and Small Magellanic Cloud (LMC, SMC) B-stars, covering a broad range of rotational velocities.

The inclusion of rotational mixing into massive star evolution (e.g., Heger & Langer 2000; Meynet & Maeder 2000; Brott et al. 2011a) brought better agreement with spectroscopic analyses that provide evidence for a characteristic enrichment of helium and nitrogen in many early-type stars (reviewed by,

e.g., Herrero 2003, Herrero & Lennon 2004 and Morel 2009). Several recent studies based on the nitrogen diagnostics performed within the *FLAMES I* survey have severely challenged the predicted effects though. In this context, nitrogen is a key element to test the predictions of rotational mixing, since it should become strongly enriched at the stellar surface of rapidly rotating stars already in fairly early evolutionary phases, whilst for slow rotation almost no enhancement should occur before the red supergiant phase. Actually, a significant number of both un-enriched fast rotators and highly enriched slow rotators have been found within the population of LMC core-hydrogen burning objects (Hunter et al. 2008a, 2009; Brott et al. 2011b).² These results imply that standard rotational mixing might be not dominant, and/or that other enrichment processes might be decisive as well (Brott et al. 2011b).

To further constrain these findings and to provide a general picture of massive star evolution, these studies need to be ex-

^{*} Based on observations collected at the European Southern Observatory Very Large Telescope, under programmes 68.D-0369, 171.D-0237 (*FLAMES*) and 67.D-0238, 70.D-0164, 074.D-0109 (*UVES*).

^{**} Appendix A, B and C are only available in electronic form at <http://www.edpsciences.org>

¹ see Evans et al. 2006 for an introductory publication and Evans et al. 2008 for a brief summary on the outcome of this project

² as well as slowly rotating, highly enriched supergiants, discussed by Vink et al. (2010)

tended to O-type stars. Because of their shorter lifetimes, the time-range where this enrichment takes place can be narrowed down, and one might be able to constrain the mixing scenario even better than it is possible from B-stars alone. In this respect, the LMC is an ideal testbed, since the nitrogen baseline abundance is low and even a strong enrichment is easier to measure/confirm than, e.g., in the Milky way.

Interestingly, most previous abundance studies of massive stars are strongly biased towards intermediate and early type B-stars. Indeed, when inspecting the available literature, metallic abundances, in particular of nitrogen, are scarcely found for O-stars. The situation for LMC objects is even worse, and data for only a few supergiants (Pauldrach et al. 1994; Crowther et al. 2002; Evans et al. 2004) and giants (Walborn et al. 2004) are available. One of the reasons for this lack of information is that the determination of nitrogen abundances is a non-trivial task, due to the complexity of N III/N IV line formation related to the impact of various processes that are absent or negligible at cooler spectral types where N II is the dominant ion.

To provide more insight into this matter, we started a series of publications dealing with nitrogen spectroscopy in O-type stars. In the first paper of this series (Rivero Gonzalez et al. 2011, hereafter Paper I), we concentrated on the formation of the optical N III emission lines at $\lambda\lambda 4634 - 4640 - 4642$, which are fundamental for the definition of the different morphological ‘f’-classes (Walborn 1971b). It turned out that the canonical explanation in terms of dielectronic recombination (Mihalas & Hummer 1973) no longer or only partly applies when modern atmosphere codes including line-blocking/blanketing and winds are used. The key role is now played by the stellar wind, which induces a (relative) overpopulation of the upper level of the transition, via pumping from the ground state rather than by dielectronic recombination as long as the wind-strength is large enough to enable a significantly accelerating velocity field already in the photospheric formation region.

The main goal of the present paper is to provide nitrogen abundances for a considerable number of O-stars in the LMC. For this purpose, we use the corresponding sample from Mokiem et al. (2007a, hereafter Mok07), mostly based on observations within the FLAMES I survey. So far, this is the largest sample of O-stars studied in the LMC by means of quantitative hydrogen and helium line spectroscopy, and allows us to determine nitrogen abundances for a significant number of objects. However, its size is still not comparable with the amount of corresponding B-stars, and does not allow us to extend the B-star results (that challenged rotational mixing) towards the O-star domain in a statistically sufficient way. Rather, it will yield a first impression on potential problems. A statistically significant analysis will become possible within the VLT-FLAMES Tarantula survey (Evans et al. 2011, ‘FLAMES II’), which provides an unprecedented sample of ‘normal’ O-stars and emission-line stars.

This paper is organized as follows. In Sect. 2, we describe the tools used to determine nitrogen abundances, both the atmospheric code and the nitrogen model atom. In particular, we study the formation of the N IV $\lambda 4058$ emission line in parallel with the N IV $\lambda 6380$ absorption line. Sect. 3 presents the stellar sample and the observations used within this study. The procedure to determine stellar and wind parameters together with nitrogen abundances is outlined in Sect. 4. In Sect. 5, we comment in detail on the individual objects. Sect. 6 provides a discussion of our results, and Sect. 7 summarizes our findings and conclusions.

2. Prerequisites for nitrogen diagnostics

2.1. The code

For this work, we use a recently updated version (v10.1) of the atmosphere/line formation code FASTWIND (see Santolaya-Rey et al. 1997 and Puls et al. 2005 for previous versions). This code has been specifically designed for the optical and IR spectroscopic analysis of hot stars of spectral types early A to O, and accounts for NLTE conditions, spherical symmetry and mass-loss. The current version incorporates a variety of updates and improvements compared with previous versions, which are briefly summarized in the following.

At first note that FASTWIND differentiates between so-called ‘explicit’ and ‘background’ elements, where the former are those used as diagnostic tools (in the present context: H, He and N) and are treated with high precision, by detailed atomic models and by means of comoving frame transport for the line transitions. The background elements (i.e., the rest) are used ‘only’ for the line-blocking/blanketing calculations, and have been treated so far by means of the Sobolev approximation. Though this is reasonable in the wind regime, the Sobolev approximation becomes doubtful in regions where the velocity field is strongly curved, which is the case in the transition zone between photosphere and wind. As we have convinced ourselves, the induced errors are not important for the background radiation field, but they can have a certain influence on the temperature structure. Applying the Sobolev approximation in regions with a strong velocity field curvature results, on average, in too strongly populated upper levels of line transitions (see, e.g., Santolaya-Rey et al. 1997). In turn, this leads to overestimated heating rates, which can result in too high temperatures in the transition region (and sometimes even below). To avoid this problem, the new FASTWIND version treats also the most important lines from the background elements in the comoving frame.

A second modification refers to the *photospheric* line acceleration. So far, this quantity (being important for the photospheric density stratification – higher line acceleration, lower density) has been calculated from the Rosseland opacities, which is strictly justified only at large optical depths. In the new version, an additional iteration cycle to calculate the photospheric structure is performed, now by using the *flux-weighted* mean from the current NLTE opacities.

By calculating a large grid of OB-star models, and comparing with solutions from the previous FASTWIND version, it turned out that both improvements affect mostly dwarfs/giants in the effective temperature range $30 \text{ kK} \leq T_{\text{eff}} \leq 35 \text{ kK}$. In particular the optical He II lines become stronger, mostly due to the somewhat lower (electron-) densities. Interestingly, this is just the domain where previous FASTWIND solutions showed the largest deviations from other codes (Simón-Díaz & Stasińska 2008). Comparing the new structures to results from TLUSTY, excellent agreement has been found. For dwarfs/giants with effective temperatures outside the ‘problematic’ region, and for all supergiants, the differences to previous results from earlier FASTWIND versions are small.

The last major improvement concerns the implementation of dielectronic recombination, both for the background and the explicit elements, and was already described and successfully tested in Paper I.

2.2. The nitrogen model atom

To perform our analysis, we implemented a new nitrogen model atom into `FASTWIND`, consisting of the ionization stages $N\text{II}$ to $N\text{V}$, which has already been used for the calculations performed in Paper I. The level structures of both $N\text{IV}$ and $N\text{V}$ have been taken from the `wm-basic` atomic database (Pauldrach et al. 1994).

$N\text{II}$ has been adapted to `FASTWIND` from a previous model ion, developed by Becker & Butler (1989). We had no intention to develop a ‘perfect’ $N\text{II}$ model, since most of our analyses deal with O-star spectra where $N\text{II}$ becomes invisible, and particularly because N. Przybilla and co-workers have already constructed such a model (based on an earlier version, see Przybilla & Butler 2001) which will be incorporated into our code after release. However, a series of tests were performed to ensure the goodness of the model ion, see Sect 2.2.1.

For $N\text{II}$, we consider 50 LS-coupled terms, up to principal quantum number $n = 4$ and angular momentum $l = 3$, where all fine-structure sub-levels have been packed. Detailed information about the selected levels is provided in Table A.1 and Fig. A.1. We account for some hundred permitted electric dipole radiative transitions. For the bulk of the transitions, oscillator strengths are taken from calculations performed by Becker & Butler (1989), but for some transitions related to strong $N\text{II}$ lines oscillator strengths have been taken from NIST.³ Radiative intercombinations are neglected. Roughly one thousand collisional bound-bound transitions are considered, with corresponding rates using the van Regemorter (1962) approximation in the radiatively permitted case and following the semi-empirical expression by Allen (1973) in the forbidden one. Radiative ionization cross sections have been derived by Becker & Butler (1989), and adapted to the representation suggested by Seaton (1958). Collisional ionization cross-sections are calculated using the Seaton (1962) formula in terms of the photoionization cross-section at threshold.

$N\text{III}$ has been already described in Paper I. In brief, it consists of 41 packed terms up to $n = 6$ and $l = 4$ (doublet and quartet system).

$N\text{IV}$. Also this model ion consists of 50 LS-coupled terms, up to principal quantum number $n = 6$ and angular momentum $l = 4$, with all fine-structure sub-levels packed into one term. Table A.2 provides detailed information about the selected levels. Two spin systems (singlet and triplet) are treated simultaneously (Fig. A.2). All allowed electric dipole radiative transitions between the 50 levels are considered, as well as radiative intercombinations, with a total of 520 transitions. Corresponding oscillator strengths have been drawn from either NIST when available or otherwise from the `wm-basic` database.⁴ Furthermore, we consider roughly one thousand bound-bound collisional transitions between all levels, with effective collision strengths among the 12 lowest LS-states from R-matrix com-

putations by Ramsbottom et al. (1994). Transitions without detailed data and collisional ionizations are treated as in $N\text{II}$.

Photoionization cross-sections have been taken from calculations by Tully et al. (1990), via TOPbase,⁵ the OPACITY Project on-line database (Cunto & Mendoza 1992). For excited levels with no OPACITY Project data available ($5g\ ^1G$, $5g\ ^3G$, $6s\ ^1S$, and $6g\ ^3G$, see Table A.2), resonance-free cross-sections are used, provided in terms of the Seaton (1958) approximation with parameters from the `wm-basic` database. Finally, the most important dielectronic recombination and reverse ionization processes are implicitly accounted for by means of exploiting the OPACITY Project photo cross-sections. Only for the few levels with no such data available, we apply the ‘explicit’ method, using the stabilizing transitions on top of resonance-free photo cross-section (see, e.g., Paper I), with corresponding data from `wm-basic`.

$N\text{V}$. Our model of this lithium-like ion (one doublet spin system) consists of 27 levels, including LS-coupled and packed terms up to $n = 7$ and $l = 6$ (see Table A.3 for details and Fig. A.3 for a Grotrian diagram). All allowed electric dipole radiative transitions are accounted for, with a total number of 102 radiative bound-bound transitions and oscillator strengths from `wm-basic`. Collisional excitations and ionizations are treated as in $N\text{II}$, whilst photo cross-sections (in terms of the Seaton 1958 approximation) have been taken from the `wm-basic` atomic database.

Our complete nitrogen model atom (from $N\text{II}$ to $N\text{V}$) comprises 178 LS-coupled levels, with more than 1100 radiative and more than 3800 collisional bound-bound transitions. To calculate the final synthetic profiles, Voigt profiles are adopted, with central wavelengths according to NIST, radiative damping parameters from the Kurucz database,⁶ and collisional damping parameters (broadening by electron impact) computed according to Cowley (1971).

2.2.1. Testing the $N\text{II}$ model ion

To test our somewhat simple $N\text{II}$ model ion,⁷ we compared synthetic line profiles with corresponding ones from `TLUSTY` (Hubeny 1998) and `DETAIL/SURFACE` (Giddings 1981; Butler & Giddings 1985), the latter based on the newly developed $N\text{II}$ model by Przybilla et al. (see Sect. 2.2).

A summary of the various tests is provided in Table 1. We started by comparing with line profiles from the `BSTAR2006` model grid (Lanz & Hubeny 2007). This grid has been calculated using the model atmosphere code `TLUSTY` (Hubeny 1988; Hubeny & Lanz 1995), a code that assumes plane-parallel geometry, hydrostatic and radiative equilibrium, and calculates line-blanketed NLTE model atmospheres and corresponding synthetic profiles. Due to its restrictions, only objects with negligible winds can be analyzed.

We used this grid of models as reference because it covers the parameter range at which $N\text{II}/N\text{III}$ are the dominant ionization stages, and the $N\text{II}$ lines are clearly visible in the synthetic spectra. In addition, the `BSTAR2006` grid has been used in numerous studies aiming at the determination of stellar abundances and parameters in B-stars (e.g., Lanz et al. 2008).

³ <http://www.nist.gov/phylab/data/asd.cfm>, firstly described in Kelleher et al. (1999)

⁴ see Pauldrach et al. (1994). In brief, the atomic structure code `SUPERSTRUCTURE` (Eissner & Nussbaumer 1969; Eissner 1991) has been used to calculate all bound state energies in LS and intermediate coupling as well as related atomic data, particularly oscillator strengths including those for stabilizing transitions.

⁵ <http://cdsweb.u-strasbg.fr/topbase/topbase.html>

⁶ www.pmp.uni-hannover.de/cgi-bin/ssi/test/kurucz/sekur.html

⁷ important, e.g., for our comparison with B-star nitrogen abundances from alternative analyses, see Sect. 6.2

Table 1. N II test series (see text).

Series	Atomic model	Photospheric stratification	NLTE/line formation
FW	see Sect. 2.2	FASTWIND	FASTWIND
FW2	see Sect. 2.2	TLUSTY	FASTWIND
TL	TLUSTY	TLUSTY	TLUSTY
Prz	Przybilla et al.	KURUCZ	DETAIL/SURFACE

A grid of FASTWIND models has been calculated, covering the temperature range $20 \text{ kK} \leq T_{\text{eff}} \leq 30 \text{ kK}$, using a typical step size of 2.5 kK, and gravities representative for dwarfs and giants. Since TLUSTY does not account for the presence of a wind, we used negligible mass-loss rates, $\dot{M} = 10^{-9} \dots 10^{-10} M_{\odot} \text{yr}^{-1}$. Because FASTWIND allows for employing external photospheric structures, we created a second grid using the TLUSTY photospheric structure, smoothly connected to the wind structure as calculated by FASTWIND, with the usual β velocity law. For consistency with the TLUSTY grid, all models have been calculated with the ‘older’ solar nitrogen abundance, $[N] = 7.92$ (Grevesse & Sauval 1998), where $[N] = \log N/H + 12$ with respect to particle numbers. Note that all tests have been performed with the complete nitrogen model atom involving the ions N II to N V as described in Sect 2.2.

It turned out that there are large differences between the synthetic N II line profiles calculated by TLUSTY (TL) and FASTWIND (FW), even though the hydrogen/helium lines agree very well (except for the forbidden component of He I which is stronger in FW-models). The latter code predicts stronger N II profiles, which is also true for the FASTWIND results based on the TLUSTY photospheric structure (FW2, see Figs. B.2 to B.7).

For dwarfs, there are almost no differences between the profiles from the FW and FW2 models. This is readily understood, since the photospheric stratification of electron temperature, T_e , and electron density, n_e , are essentially the same (see Fig. B.1, panel 1, 3, 5), i.e., FASTWIND and TLUSTY predict the same structures.

On the other hand, models for giants at higher T_{eff} display (mostly) weak differences. E.g., at $T_{\text{eff}} = 27.5 \text{ kK}$ and $\log g = 3.0$, there is a small disagreement of the electron densities in photospheric regions ($\tau_{\text{Ross}} \leq 10^{-5}$), even though the temperatures agree quite well (Fig. B.1, panel 6). In particular, the TLUSTY and thus the FW2 structure shows a lower electron density at optical depths where the photospheric lines are formed, because of a higher photospheric radiative line pressure in this model.

Because of the lower electron density, the lower recombination rates (at $T_{\text{eff}} = 27.5 \text{ kK}$, N III is the dominant ion) lead to somewhat weaker N II profiles in the FW2 models compared to the FW ones, see Fig. B.7. Nevertheless, differences to the profiles as predicted by TL itself are still large, and we conclude that the photospheric structure is not the origin of the discrepancies.

As an independent check, we compared our results with spectra calculated by N. Przybilla (priv. comm.) for two of our grid models, denoted by Prz in the following. These spectra are based on the NLTE/line formation code DETAIL/SURFACE, and the N II model ion recently developed by Przybilla et al.. We consider this atomic model as the superior one in the present context, because large effort on improving and testing the atomic data has been spent, and corresponding synthetic spectra perfectly match high resolution/high signal-to-noise observations from various B-stars (Przybilla et al. 2008).

Figures B.2 and B.4 show that the agreement between the FW and Prz profiles is excellent, which leaves us with the conclusion that there might be problems in the N II atomic data used in the BSTAR2006 grid. Important studies using TLUSTY have been carried out during the past years (e.g., Dufton et al. 2006; Trundle et al. 2007; Hunter et al. 2009), including the determination of N II abundances in LMC and SMC B-stars. Actually, these studies utilized a different model atom, developed by Allende Prieto et al. (2003), which has been tested by N. Przybilla at our request, with a positive outcome. Thus, the aforementioned analyses should be free from uncertainties related to a potentially insufficient atomic model.

2.3. Diagnostic nitrogen lines in the optical

Table 2 presents a set of 51 nitrogen lines visible in the optical (and adjacent) spectra of OB-stars, along with the position of potential blends. Included are the connected levels (for corresponding term designations, see Appendix A) and multiplet numbers, to provide an impression of how much independent lines are present.

Lines from N II (visible in the spectra of B and late O-stars) have been selected after careful comparisons with profiles calculated by N. Przybilla (priv. comm., see Sect. 2.2.1). Only one of the suggested lines, N II $\lambda 3995$, is completely isolated, and remains uncontaminated even at high rotation rates. Moreover, this is one of the strongest N II lines located in the optical region, making it a good choice for deriving nitrogen abundances. Other useful lines are N II $\lambda 5667$ and $\lambda 5679$, where the former is moderately strong and the latter has roughly the same strength as N II $\lambda 3995$.

The subset comprising lines from N III has been discussed in Paper I. Prominent lines from N III, N IV and N V are among the most well-known features in O-stars, and can be used to infer nitrogen abundances as well as effective temperatures for the earliest subtypes, from the reaction of the N IV/N V ionization equilibrium.⁸ In a similar line of reasoning, Walborn et al. (2002) used the N IV $\lambda 4058$ emission line in combination with N III $\lambda \lambda 4634-4640-4642$ to split the degenerate O3 spectral type (Walborn 1971a) into three different types O2, O3, and O3.5, relying on the N IV/N III emission line ratio.⁹ Thus, a detailed understanding and modelling of N IV $\lambda 4058$ (together with the N III triplet, see Paper I) is mandatory, to safely employ this powerful diagnostics.

N IV $\lambda 4058$ and N IV $\lambda 6380$ connect the ‘neighbouring’ levels of the singlet series $1s^2 2s3l$ with $l = s, p, d$ (levels #8, 9, and 12 in Table A.2). N IV $\lambda 4058$ (if present) is observed in emission in the majority of stars, and has been suggested to be formed by photospheric NLTE processes (see below) rather than by emission in an extended atmosphere, in analogy to the N III triplet emission. Note that there is no detailed analysis of the line formation process. So far, only Taresch et al. (1997) and Heap et al. (2006) simulated the behavior of this line as a function of effective temperature. Heap et al. found emission for this line at $T_{\text{eff}} > 40,000 \text{ K}$ for $\log g = 4.0$ and $[N] = 7.92$, using the plane-

⁸ At the earliest O-types the standard technique for deriving effective temperatures based on He I and He II line-strengths becomes difficult or even impossible, due to vanishing He I and rather insensitive He II lines from $T_{\text{eff}} = 45 \text{ kK}$ on.

⁹ This classification scheme has been criticized by Massey et al. (2004, 2005) who found that for stars with similar effective temperature and surface gravity the N IV/N III emission line ratio can vary over the full range as defined for O2 and O3.5.

Table 2. Diagnostic nitrogen lines in the optical (and adjacent) spectrum of early B- and O-type stars, together with potential blends.

Ion	Transition	Multiplet	Line	Wavelength(Å)	Blends	Used
N II	N29 - N216	12	1	3994.99	-	+
	N211 - N219	15	2	4447.03	O II λ 4446.81, 4447.67, 4448.19, O III λ 4447.79	+
	N28 - N215	5	3	4601.47	O II λ 4602.13, 4603.23, N III λ 4604.18	+
	N28 - N215	5	4	4607.16	O II λ 4609.44, 4610.20, N III λ 4605.16, Ne II λ 4606.70	+
	N28 - N215	5	5	4621.39	O II λ 4621.27, N III λ 4621.04, 4623.05, Si II λ 4621.72	+
	N28 - N215	5	6	4630.54	O III λ 4630.77, N III λ 4630.61, Si IV λ 4631.24	+
	N28 - N215	5	7	4643.09	O II λ 4641.81, 4643.89, N III λ 4641.85	-
	N212 - N218	19	8	5005.15	O III λ 5006.84	-
	N214 - N221	24	9	5007.33	O III λ 5006.84	-
	N28 - N214	4	10	5045.10	N II λ 5046.53	-
	N28 - N212	3	11	5666.63	C II λ 5662.47	-
	N28 - N212	3	12	5676.01	N II λ 5679.55	-
	N28 - N212	3	13	5679.55	N II λ 5676.01	-
	N28 - N212	3	14	5710.77	Si II λ 5707.20	-
	N215 - N220	28	15	5941.65	N II λ 5940.24, N III λ 5943.44	-
	N III	N320 - N333	17	1	4003.58	O II λ 4007.46
N38 - N310		1	2	4097.33	O II λ 4097.26, 4098.24, H δ λ 4101.74	+
N313 - N322		6	3	4195.76	O II λ 4192.52, 4196.26, Si III λ 4195.59, He II λ 4200.00	+
N313 - N322		6	4	4200.07	He II λ 4200.00	-
N321 - N334		18	5	4379.11	O II λ 4378.03, 4378.43, C III λ 4379.47, N II λ 4379.59	+
N312 - N316		3	6	4510.88	N III λ 4510.92, Ne II λ 4511.42	+
N312 - N316		3	7	4514.86	O III λ 4513.83, Ne II λ 4514.88, C III λ 4515.81, 4516.77	+
N312 - N316		3	8	4518.14	Ne II λ 4518.14, O III λ 4519.62	+
N310 - N311		2	9	4634.14	Si IV λ 4631.24, O IV λ 4632	+
N310 - N311		2	10	4640.64	O II λ 4638.86, Si III λ 4638.28	+
N310 - N311		2	11	4641.85	O II λ 4641.81, 4643.39, N II λ 4643.08	+
N322 - N330		21	12	5320.82	O II λ 5322.53	-
N322 - N330		21	13	5327.18	-	-
N319 - N325		14	14	6445.34	-	-
N319 - N325		14	15	6450.79	C IV λ 6449.90	-
N319 - N325		14	16	6454.08	O II λ 6457.05, N II λ 6457.68	-
N319 - N325		14	17	6467.02	-	-
N IV	N47 - N410	1	1	3478.71	-	+
	N47 - N410	1	2	3482.99	-	+
	N47 - N410	1	3	3484.96	-	+
	N49 - N412	3	4	4057.76	C III λ 4056.06, 4059.56	+
	N48 - N49	2	5	6380.77	O III λ 6378.34, 6383.30, DIBs λ 6376.08, 6379.32	+
	N413 - N416	5	6	5200.41	O IV λ 5198.22	-
	N413 - N416	5	7	5204.28	N IV λ 5205.15	-
	N413 - N416	5	8	5205.15	N IV λ 5204.28, O II λ 5206.65	-
	N410 - N411	4	9	7103.24	-	+
	N410 - N411	4	10	7109.35	-	+
	N410 - N411	4	11	7111.28	-	+
	N410 - N411	4	12	7122.98	-	+
	N410 - N411	4	13	7127.25	-	+
	N410 - N411	4	14	7129.18	-	+
	N V	N53 - N54	1	1	4603.73	N III λ 4604.18, 4605.16, N IV λ 4606.33
N53 - N54		1	2	4619.98	Si III λ 4619.66, N III λ 4621.04, 4623.05	+
N518 - N525		9	3	4943.17	O IV λ 4941.29	-
N519 - N526		10	4	4943.97	O IV λ 4941.29	-
N520 - N527		10.01	5	4945.29	-	-

Notes. Line numbers for N II, N IV and N V refer to important transitions as indicated in Figs. A.1, A.2 and A.3, respectively, and for N III to the corresponding figure (B.1) in Paper I. Multiplet numbers for N II/N III are from Moore (1975), and for N IV/N V from Moore (1971). Lines used within the present work are labeled by '+'. Lower and upper levels of the transitions are denoted by a combination of ion and level number according to Tables A.1, A.2 and A.3, e.g., 'N29' means level #9 of N II.

parallel atmospheric code TLUSTY, supporting the idea that the emission is of photospheric origin and that velocity fields are not required to explain the basic effect. Other arguments for the photospheric origin of N IV λ 4058 are the agreement with other, absorption line profiles as a function of $v \sin i$, unshifted radial velocities, and lack of P Cygni profiles (N. Walborn, priv. comm.).

Interestingly, N IV λ 6380 appears clearly in absorption in O-star spectra, and seems to play a similar role as the N III absorption lines at λ 4097 – 4103 in the N III emission line problem (see Paper I). We note that N IV λ 6380 can be significantly affected by the presence of two Diffuse Interstellar Bands (DIBs) at λ 6376.08, 6379.32 (Herbig 1975; Krelowski et al. 1995), the latter being stronger if reddening is important. Fortunately, the stars analysed in this paper are subject to low reddening, and

these DIBs only minorly affect some of the observed N IV $\lambda 6380$ lines (e.g. N11-038, Fig. C.8).

As for the previous pair of N IV lines, N IV $\lambda 6380$ and N IV $\lambda 4058$, also the N IV multiplets around 3480 Å and 7103-7129 Å are formed between levels of the same series (here within the triplet system – levels #7, 10, and 11 in Table A.2), and seem to mimic the behavior of these lines: at least in the earliest O-star regime they are prominent features, where the former multiplet appears in absorption and the latter in emission. Both line complexes are widely used in WR-star analyses, and the emission in the latter multiplet is a strong feature in most WR spectra. The lack of emission at this multiplet and also at N IV $\lambda 4058$ has been used for classification purposes in different WR-star studies (e.g., Negueruela & Clark 2005). Likewise, the multiplet around 3480 Å has been used by Walborn et al. (2004) to infer both T_{eff} and nitrogen abundances for a set of O2 stars.

The remaining N IV lines listed, N IV $\lambda \lambda 5200 - 5204 - 5205$, belong also to the triplet system, and appear, if present, in absorption (for O-stars). Unfortunately, most spectra used within this study do not cover this spectral region. For the few field stars where this range is available to us (see Sect. 3.2), this multiplet is not visible.

Finally, N V lines at $\lambda \lambda 4603-4619$ are produced by transitions between the fine-structure components of $3s^2S$ and $3p^2P^0$ (levels #3 and 4 in Table A.3). These doublet lines are strong absorption features in the earliest O-stars, showing sometimes extended absorption in their blue wings or even pronounced P-Cygni profiles (e.g., N11-031, Fig. C.7), revealing that they can be formed in the wind. Thus, it is clear that mass-loss and wind-clumping will influence the formation of these lines. Besides, we also list N V $\lambda \lambda 4943 - 4945$ which become important, (almost) isolated diagnostic lines in the spectra of very early, nitrogen rich O- and WNL-stars. Unfortunately, the corresponding wavelength range has not been observed for the bulk of our sample stars (see Sect 3.2), whilst no features are visible in the few early-type spectra (field stars) where this range is available. Note that in order to use these lines, we would need to extend our N V model ion, including high-lying levels, to allow for cascading processes into the corresponding upper levels at $n = 7$ (which are our present uppermost ones).

2.4. Understanding the N IV $\lambda 4058/\lambda 6380$ line formation

In the following, we discuss the most important mechanisms that explain the presence of emission at N IV $\lambda 4058$, in particular the decisive role of mass-loss. Our analysis is based on the model-grid as described in Sect. 4.2, and refers to LMC background abundances plus a solar (Asplund et al. 2005) nitrogen abundance, $[N] = 7.78$,¹⁰ chosen in order to obtain pronounced effects.

All the important levels and the corresponding transitions involved in the N IV emission problem are summarized in Fig. 1. A comparison with the analogous diagram for N III (Fig. 1 in Paper I) shows a number of similarities but also differences. In addition to what has already been outlined, the upper level of the emission line ($3d \rightarrow 3p$) is fed by only weak dielectronic recombination, with almost no influence on the population of 3d (contrasted to the N III case), and there is no resonance line connected to 3d (which turned out to be crucial for N III). Instead, the *lower* level of $\lambda 4058$, 3p, is connected with the ground-state. Similar

¹⁰ roughly 0.9 dex above the LMC baseline abundance, $[N]_{\text{baseline}} = 6.9$, following Hunter et al. (2007).

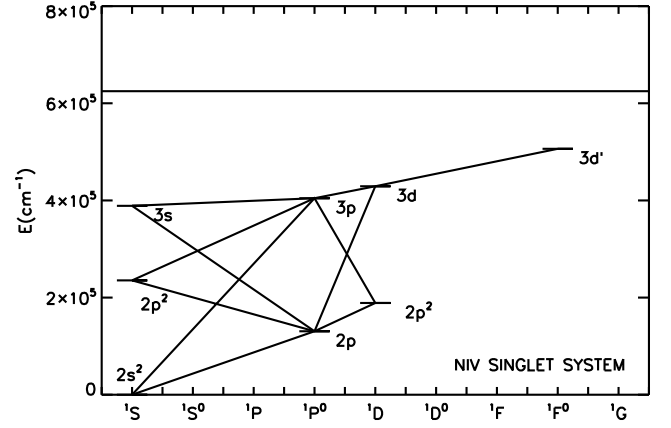


Fig. 1. Simplified Grotrian diagram displaying the most important transitions involved in the N IV emission line problem. The horizontal line marks the N V ionization threshold. N IV $\lambda 4058$ is formed by the transition $3d^1D \rightarrow 3p^1P^0$, while the absorption line at $\lambda 6380$ originates from the transition $3p^1P^0 \rightarrow 3s^1S$. An efficient drain of 3p is provided by the ‘two-electron’ transitions $3p^1P^0 \rightarrow 2p^2^1S, ^1D$. Cascade processes from $3d^2^1F^0$ and pumping from $2p^1P^0$ are the major routes to overpopulate the $3d^1D$ state. See text.

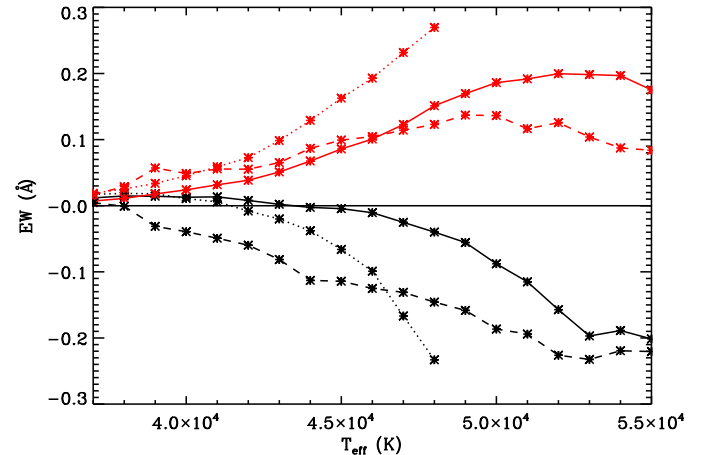


Fig. 2. Equivalent width (positive for absorption) of N IV $\lambda 4058$ (black) and N IV $\lambda 6380$ (red) as a function of T_{eff} . Solid and dotted curves refer to low \dot{M} (model series ‘A’) with $\log g = 4.0$ and 3.7 , respectively, and dashed curves to supergiant mass-loss rates (model series ‘E’), with $\log g = 4.0$.

to N III, on the other hand, there are two strong ‘two-electron’ transitions able to drain 3p, via $3p^1P^0 \rightarrow 2p^2^1S, ^1D$.

2.4.1. Basic considerations

In agreement with the results from Heap et al. (2006), our simulations (see Fig. 2) show that N IV $\lambda 4058$ turns from weak absorption (around $T_{\text{eff}} \approx 37$ kK) into weak emission around $T_{\text{eff}} \approx 42$ kK, for models with (very) low mass-loss rate and $\log g = 4.0$. As usual, we define equivalent widths to be positive for absorption and to be negative for emission lines. We find a 2 kK difference w.r.t. the turning point, which can be attributed,

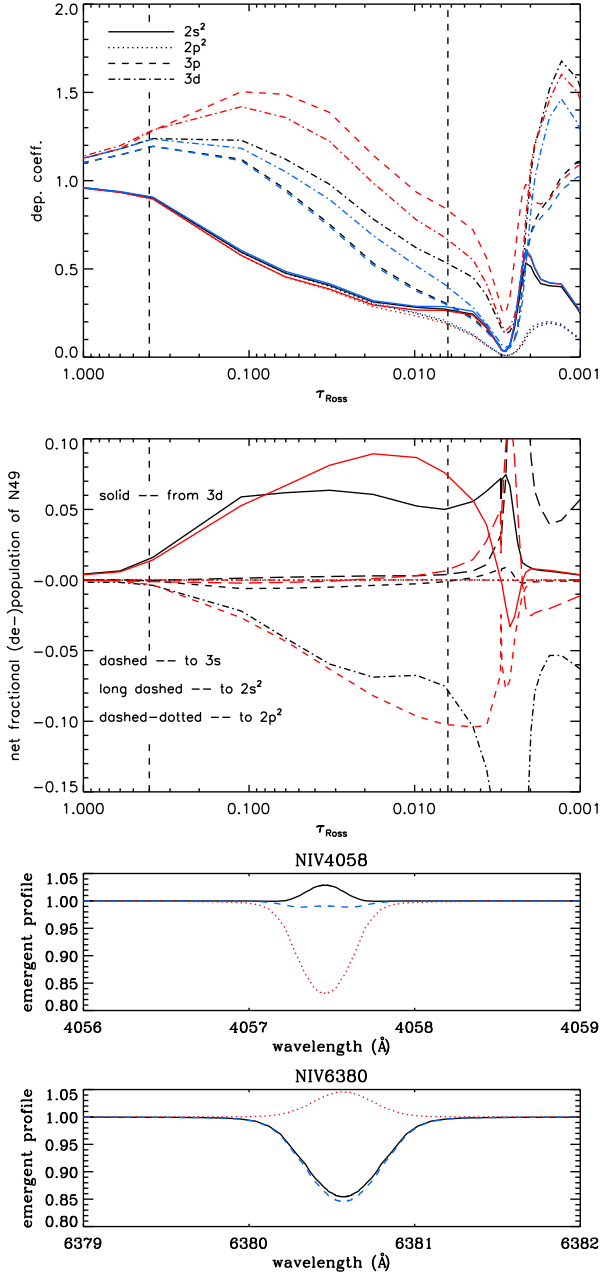


Fig. 3. Departure coefficients, fractional net rates and line profiles for N IV $\lambda 4058/\lambda 6380$ and involved processes, for model ‘A4540’. Designation for $2p^2$ refers to $2p^2 \ ^2D$ only since the other fine-structure component, $2p^2 \ ^2S$, behaves similarly. *Upper panel:* NLTE departure coefficients as a function of τ_{Ross} . The onset of the wind is clearly visible at $\tau_{\text{Ross}} \approx 0.003$. Black curves: standard model with $b_{3d} > b_{3p}$; red curves: draining transitions $3p \rightarrow 2p^2$ suppressed, leading to $b_{3d} < b_{3p}$; blue curves: transition $2p \rightarrow 3d$ suppressed. *Middle panel:* fractional net rates to and from $3p$, for the standard model (black) and the model with suppressed draining transitions (red). *Lower panel:* line profiles for N IV $\lambda 4058$ and $\lambda 6380$, for the three models displayed in the upper panel, with similar color coding.

to a major part, to the lower nitrogen content of our models and different background abundances. Towards hotter temperatures, the emission strength increases monotonically until a maximum around $T_{\text{eff}} \approx 53$ kK has been reached, after which the emission

stabilizes and finally decreases. For lower gravities and/or higher mass-loss rates, the line turns into emission at lower T_{eff} , so that, for a given T_{eff} , the emission strength increases with decreasing $\log g$ and increasing mass-loss rate, \dot{M} . Since the absorption strength of N IV $\lambda 6380$ increases in a similar way (though with a much weaker impact of \dot{M} , and only until $T_{\text{eff}} \approx 50$ kK), both lines appear (for a given T_{eff}) as anti-correlated, at least for a large range of temperatures. In contrast, the corresponding transitions of N III were found to be correlated (Paper I).

The behaviour of both lines and the corresponding level structure implies an efficient drain of level $3p$ that enhances the emission at $\lambda 4058$ as well as prevents emission/increases absorption at $\lambda 6380$, and is provided by the two ‘two-electron’ transitions $3p \rightarrow 2p^2 \ ^1D, \ ^1S$, similar to the case of N III.¹¹

To investigate this mechanism in more detail, and to avoid ‘contamination’ by wind effects, we concentrate at first on a low- \dot{M} model with decent emission at N IV $\lambda 4058$, with $T_{\text{eff}} = 45,000$ K and $\log g = 4.0$.¹² In the upper panel of Fig. 3, we provide the NLTE departure coefficients, b , of involved levels, where black curves refer to our standard model. Obviously, level $3d$ is overpopulated with respect to $3p$ ($b_{3d} > b_{3p}$) over the complete line formation region. On the other hand, levels $2p^2 \ ^1D$, $2p^2 \ ^1S$, and $2p$ (the latter two not displayed) are (mostly collisionally) coupled to the ground state, which in itself is strongly depopulated, due to rather large ionizing fluxes (see below). This situation closely resembles the situation in N III, where strongly depopulated draining levels (for non-blocked models) favoured a depopulation of the analogous level $3p$.

To further clarify the impact of the different processes, we investigate the corresponding *net rates* responsible for the population and depopulation of level $3p$ (Fig. 3, middle panel, black curves). As in Paper I, we display the dominating individual net rates (i.e., $n_j R_{ji} - n_i R_{ij} > 0$ for population, with index i the considered level) as a fraction of the *total* population rate. Indeed, the drain by level $2p^2 \ ^1D$ (dashed-dotted) and/or level $2p^2 \ ^1S$ (not displayed) are the most important processes that depopulate level $3p$ in the line formation region. In contrast, the resonance line does not contribute to any (de-)population of level $3p$, since it is (almost) in detailed balance (long dashed line).

To check the validity of our scenario, we calculated an alternative model where the two draining transitions have been suppressed, by using very low oscillator strengths. Indeed, the upper panel of Fig. 3 (red curves) shows that now b_{3d} is smaller than b_{3p} , and $\lambda 4058$ goes into absorption (lower panel, red color). From the fractional net rates, we see that the preferred decay route has switched from $3p \rightarrow 2p^2$ (standard model, black) to $3p \rightarrow 3s$ (red, dashed), though level $3p$ retains a much larger population.

The upper level of $\lambda 4058$, $3d$, is predominantly fed by cascading from $3d' \ ^1F^0$, and also by pumping from level $2p$, whilst dielectronic recombinations are negligible. Suppressing the population from level $2p$ leads to less emission (Fig. 3, lower panel, blue colors), due to a less populated level $3d$ (upper panel).

Let us now consider the behaviour of the absorption line at $\lambda 6380$, resulting from the transition $3p \rightarrow 3s$, again by means of

¹¹ though in Paper I we argued that in case of N III this mechanism becomes suppressed in realistic model atmospheres with near-solar background abundances.

¹² At cooler T_{eff} , this line is in absorption because of a lower N IV ionization fraction implying deeper formation depths, which are closer to LTE.

Fig. 3. As mentioned earlier, this line shows an anti-correlation¹³ with N IV λ 4058, in contrast to the behaviour of the corresponding N III lines which appear as correlated. In Paper I we argued that the latter correlation results from the proportionality of the level populations of 3p and 3s. That is, when b_{3p} decreases (e.g., due to increased ‘two-electron’ drain), b_{3s} decreases in parallel due to less cascading, and the absorption at λ 4097 becomes weaker in concert with an increase in the triplet emission. Vice versa, an increase of 3p implies less emission of the triplet lines and more absorption at λ 4097, respectively.

Such a reaction requires the transition $3p \rightarrow 3s$ to be optically thin, dominated by spontaneous decays, which is no longer true for N IV λ 6380. Due to a mostly significant optical depth, the radiative net rate is no longer dominated by spontaneous decays, but depends also on absorption and induced emission processes. Now, an increased population of 3p leads to less increase of b_{3s} ,¹⁴ and the absorption becomes *weaker* because of an increased source function $\propto b_{3p}/b_{3s}$. Vice versa, a decrease in the population of 3p leads to more absorption at λ 6380 in parallel with more emission at λ 4058. This behaviour becomes particularly obvious if we investigate the reaction of the absorption line when suppressing the draining transitions. In this case, 3p becomes strongly overpopulated (Fig. 3, upper panel, red color), and λ 4058 goes into absorption whilst λ 6380 becomes an emission line, due to a significantly increased source function (more pumping than in the original scenario). We checked that if the absorption and stimulated emission terms in the $3p \rightarrow 3s$ transitions are neglected, λ 6380 displays more absorption instead, in accordance with our previous arguments.

Note, however, that this anti-correlation is not complete. E.g., if one changes processes which have an effect on 3d alone, the absorption strength of λ 6380 remains unaltered. Thus, by suppressing $2p \rightarrow 3d$, only b_{3d} is affected (upper panel, blue vs. black curves), and there is less emission at λ 4058 while the absorption at λ 6380 remains at the previous level (lower panel).

Summarizing, we interpret the different correlations between emission and absorption line-strength in N III and N IV as due to optical depth effects in the $3p \rightarrow 3s$ transition. As long as this is optically thin, cascade effects dominate, and both lines appear as correlated (N III). Larger optical depths introduce a counteracting ‘source-function effect’, and the lines become anti-correlated (N IV). The rather large degree of such anti-correlation supports the importance of the draining transitions, since these are able to influence both the absolute population of the involved levels as well as their ratios in a very efficient way, by providing additional decay channels for level 3p.

2.4.2. The impact of wind effects

So far, we discussed the possibility of obtaining emission at N IV λ 4058 via solely photospheric NLTE processes. In Paper I, the presence of a wind (actually, a steep rise of the velocity field in the outer photosphere) turned out as crucial to explain the observed N III triplet emission in Of-stars, enabling an efficient pumping of the *upper* level by the corresponding resonance line. To investigate how the presence of a wind affects the

¹³ when certain parameters/processes are changed for a given T_{eff} , e.g., the strength of the draining levels, the background opacities and so on. The *overall* increase of these line-strengths as a function of T_{eff} is related to the increasing ionization fractions.

¹⁴ The net radiative rate (downward) is proportional to $A(1 - \bar{J}/S)$, with Einstein coefficient for spontaneous decay, A , scattering integral \bar{J} and source function, S .

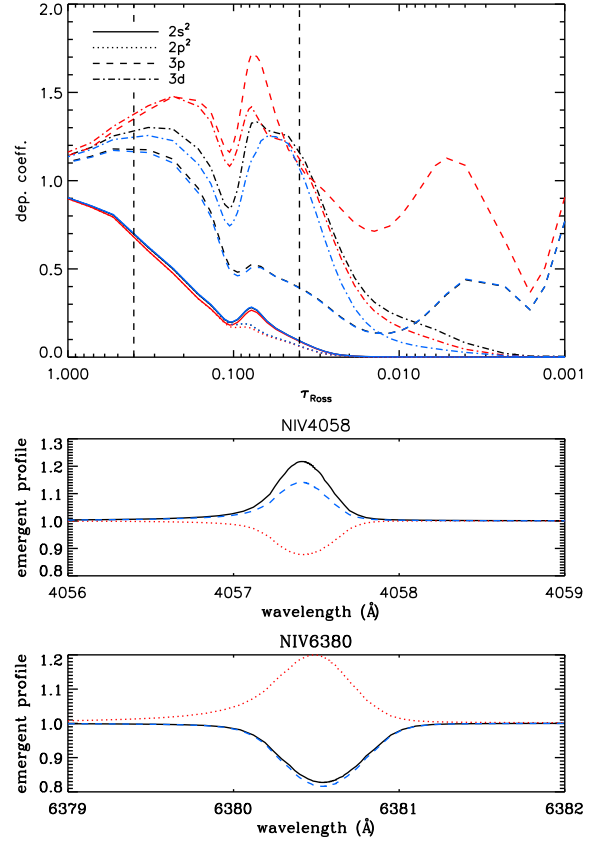


Fig. 4. Departure coefficients (top) and line profiles for N IV λ 4058/ λ 6380 (bottom) for the dense-wind model ‘E4540’. Level designations, lines, and color coding as in Fig. 3.

emission at N IV λ 4058, we compare our previous model ‘A4540’ with model ‘E4540’, which has the same stellar parameters but a considerably larger, supergiant-like mass-loss rate. It turns out that the inclusion of such a strong wind has a pronounced effect. Comparing Fig. 4 (lower panel) with Fig. 3, model ‘E4540’ (black) results in much more emission than ‘A4540’, increasing the equivalent width of λ 4058 from -7 to -114 mÅ. Also for higher T_{eff} the impact of \dot{M} remains significant. The absorption line N IV λ 6380 is affected by the wind as well, though less pronounced. The absorption becomes slightly stronger (by 18% in the equivalent width), i.e., the anti-correlation discussed above is still present. This is valid not only for model ‘E4540’, but also for hotter models (Fig. 2), until the wind-emission begins to contaminate N IV λ 6380.

The origin of such stronger emission at λ 4058 becomes clear if one inspects the involved departure coefficients (Fig. 4, upper panel, black curves). Again, the onset of the wind is clearly visible (at $\tau_{\text{Ross}} \approx 0.1$), now much deeper than in the ‘A’ model, and the line formation region is located in between $\tau_{\text{Ross}} \sim 0.40 \dots 0.04$. Compared to the ‘A’ model, ‘E4540’ displays a larger ground-state depopulation, where the ground-state remains coupled with the draining levels $2p^2$ as well as with level $2p$ (not displayed). This leads, particularly in the transition region between photosphere and wind, to an extreme depopulation of 3p. Since level 3d becomes strongly overpopulated, mostly due to feeding by $3d \rightarrow 1F^0$ (which is severely overpopulated as well), the resulting line source function is quite large and partly even in inversion, which explains the pronounced emission at N IV λ 4058.

All these differences are caused by the onset of the wind. At first note that the N IV continuum ($\lambda < 160 \text{ \AA}$) is strongly coupled with the He II continuum. As already realized by Gabler et al. (1989), increasing mass-loss leads to more He II ground-state depopulation, to higher fluxes in the He II continuum and thus also to higher fluxes in the N IV continuum. Consequently, the N IV ground-state becomes strongly depopulated, and the nitrogen ionization equilibrium switches from N IV (being the dominant stage in the deeper photosphere) towards N V from the transition region on. This also favours the overpopulation of 3d, by means of increased recombinations to high-lying levels with subsequent cascades via $3d^1 \text{ F}^0$.

One might now argue that the inclusion of the wind could amplify the impact of the resonance transition(s), by producing deviations from detailed balance leading to strong pumping, similar to the case of N III. Unlike the situation in N III, however, such an effect would lead to less line emission or even absorption at N IV $\lambda 4058$, since here the resonance line is connected to the lower level, 3p. As it turns out, however, this effect is not present, since the resonance line is too strong (N IV is the dominant ion until the transition region) to leave detailed balance before the wind has reached a significant speed. Only then, the resonance transition becomes dominant in populating level 3p, but this occurs already far beyond the formation region of N IV $\lambda 4058$. Close to the formation region, there is only a moderate population of 3p by the resonance line, similar to the population from 3d itself. Even this additional population is counteracted (actually, even slightly overcompensated) by enhanced drain towards $2p^2$, not only in the formation region of $\lambda 4058$ but also in those outer regions where the resonance line strongly pumps.

These arguments are supported by the fact that N IV $\lambda 6380$ is only slightly affected by the wind, where the increased absorption results mostly from a diminished source function due to a less populated 3p level. Performing the same tests as for the thin wind case, i.e., either suppressing the drain or suppressing the population of 3d via $2p \rightarrow 3d$ leads to similar results, as can be seen from the red and blue curves and profiles in Fig. 4, respectively.

We conclude that \dot{M} is a key parameter for modeling the N IV emission line, where in contrast to N III the basic mechanism (for typical mass-loss rates and below) is always due to the depopulation of the lower level by the ‘two-electron’ transitions. This drain becomes stronger as a function of \dot{M} , because of increasing ionizing fluxes leading to more ground-state depopulation.

3. Stellar sample and observations

3.1. The stellar sample

Table 3 lists our stellar sample which has been drawn from the analysis of LMC O-/early B-stars by Mok07.

Three of the 28 stars from the original sample have been discarded from the present analysis, for two reasons. First, from our analysis we suspect that N11-004 and N11-048 might be (SB1) binaries, where the former object shows discrepant line shifts and for the latter we were not able to reproduce accurately the observed He lines (shape and strength). A possible binarity of N11-048 was also suggested by Mok07, because of similar reasons. The other discarded star, Sk-67° 166, is the only object in the original sample which seems to be strongly evolved (helium content $Y_{\text{He}} = \text{N}(\text{He})/\text{N}(\text{H}) = 0.20 \dots 0.28$, Crowther et al. 2002 and Mok07, respectively), and has a very dense wind, with both H_α and He II $\lambda 4686$ in strong emission. We

confirm the stellar/wind parameters as derived by Mok07 (almost perfect fit quality of H/He lines), but did not succeed in a reasonable fit for the nitrogen lines. A comparison with the analysis by Crowther et al. (2002) shows similar discrepancies. Because of this problem and because of its highly evolved evolutionary status, which does not match with all other objects in our sample, we decided to discard this object from our present analysis and will re-consider it in a future attempt.

The remaining sample consists of 20 O-stars, mostly giants or dwarfs, and 5 early B-type supergiants or giants. All of the B-stars and 15 O-stars are associated with the cluster N11, and the others are field stars. The early B-stars have been included in our sample to allow us for a comparison with previous analyses of such stars (Hunter et al. 2009) in order to check the consistency of different codes and methods in the transition region between O- and B-types (Sect. 6.2).

Table 3 gives information about spectral type, V-magnitude, interstellar extinction and absolute visual magnitude, and has been taken from Mok07. Spectral types for N11 objects are based on Evans et al. (2006), slightly revised by Mok07 in collaboration with C. Evans (priv. comm.), and for the field stars from Walborn et al. (1995), and Massey et al. (1995, 2005). For the field star Sk-70° 69 we added the (f) designation since the present spectra show clear emission at N III $\lambda 4634-4640-4642$ and He II $\lambda 4686$ in absorption.

3.2. Observations

Most of the observations (for objects denoted by ‘N11-’) have been carried out within the FLAMES I survey, and are described in detail in Evans et al. (2006). In brief, the data were obtained using the Fibre Large Array Multi-Element Spectrograph (FLAMES) at the VLT, for six wavelengths settings with an effective resolving power of $R \approx 20,000$. The S/N ratios are in the ranges 50-200 for LMC objects. After sky subtraction, each wavelength range was co-added and normalized by means of a cubic spline.¹⁵ The final merged spectra cover two spectral ranges, 3850-4750 Å and 6300-6700 Å.

To improve the sampling in luminosity and temperature, Mok07 augmented the N11 sample by LMC O-type field stars, which were observed using the UVES spectrograph at the VLT as part of the ESO programmes 67.D-0238, 70.D-0164, and 074.D-0109 (P.I. P. Crowther). Spectra were obtained for four different wavelength settings, at an effective resolving power of $R \approx 40,000$. The final product provides coverage between 3300-5600 Å and 6300-10400 Å for all stars except for Sk-70° 69, where ‘only’ the region between 3300-5600 Å and 6300-6700 Å had been observed. The typical S/N ratios achieved for all spectra lie in the range 60-80.

4. Analysis

4.1. Methodology

In an ideal world, we could have used the stellar and wind parameters as obtained by Mok07 from H/He lines, and simply derived the nitrogen abundances on top of atmospheric models with these parameters. Unfortunately, there are reasons to re-analyze all programme stars. At first, the present FASTWIND version (see Sect. 2.1) is somewhat different from the version used

¹⁵ We performed additional re-normalizations for different wavelength ranges.

Table 3. Sample stars used within this study, along with spectral type, V-magnitude, interstellar extinction A_V , and absolute visual magnitude M_V . All quantities have been taken from Mok07.

Star	Cross-IDs	Spectral Type	V	A_V	M_V
N11-026	-	O2 III(f*)	13.51	0.47	-5.46
N11-031	P3061/LH10-3061	ON2 III(f*)	13.68	0.96	-5.78
N11-038	P3100	O5 II(f*)	13.81	0.99	-5.68
Sk-66° 100	-	O6 II(f)	13.26	0.34	-5.58
N11-032	P3168	O7 II(f)	13.68	0.65	-5.47
N11-045	-	O9 III	13.97	0.50	-5.03
BI253	-	O2 V((f*))	13.76	0.71	-5.45
BI237	-	O2 V((f*))	13.89	0.62	-5.23
N11-060	P3058/LH10-3058	O3 V((f*))	14.24	0.81	-5.07
Sk-70° 69	-	O5 V((f))	13.95	0.28	-4.83
N11-051	-	O5 Vn((f))	14.03	0.19	-4.66
N11-058	-	O5.5 V((f))	14.16	0.28	-4.62
Sk-66° 18	-	O6 V((f))	13.50	0.37	-5.37
N11-065	P1027	O6.5 V((f))	14.40	0.25	-4.35
N11-066	-	O7 V((f))	14.40	0.25	-4.35
N11-068	-	O7 V((f))	14.55	0.28	-4.23
N11-061	-	O9 V	14.24	0.78	-5.04
N11-123	-	O9.5 V	15.29	0.16	-3.37
N11-087	P3042	O9.5 Vn	14.76	0.62	-4.36
N11-029	-	O9.7 Ib	13.63	0.56	-5.43
N11-036	-	B0.5 Ib	13.72	0.40	-5.18
N11-008	Sk-66° 15	B0.7 Ia	12.77	0.84	-6.57
N11-042	P1017	B0 III	13.93	0.22	-4.79
N11-033	P1005	B0 III _n	13.68	0.43	-5.25
N11-072	-	B0.2 III	14.61	0.09	-3.98

Notes. Primary identifications for N11 objects are from Evans et al. (2006). Identifications starting with "SK", "BI", "P", and "LH" are from Sanduleak (1970), Brunet et al. (1975), Parker et al. (1992), and Walborn et al. (2002, 2004), respectively.

by Mok07, and the parameters need certain (mostly small) alterations in order to reach a similar fit quality to the H/He lines. Second, we used a somewhat different fitting strategy with respect to the 'free' parameters, which changes the optimum fit. In contrast to Mok07, we derived and fixed the projected rotational velocity, $v \sin i$, independently from the actual fitting procedure (Sect. 4.3), whereas Mok07 included $v \sin i$ as a free parameter in their fitting algorithm. Moreover, during our fit procedure we allowed for the presence of extra line-broadening ('macro-turbulence', v_{mac}), not considered by Mok07. Differences in $v \sin i$ and v_{mac} can lead to certain differences in the outcome of the fit, since the profile shapes might change (e.g., Fig. 4 in Puls 2008). Third, and most important, is the fact that we now aim at a consistent fit for the H/He *and* nitrogen lines. Thus, and in the sense of a compromise solution (minimization of the differences between observed and synthetic spectra for *all* lines), different stellar parameters which result in a modest change of the fit quality of H/He alone¹⁶ can lead to a significant improvement with respect to the complete set of lines.

In so far, we opted for an entire re-analysis, performed mostly by a simple 'fit-by-eye' method where we try to accomplish the best fit to the strategic lines by visual inspection (for a discussion, see Mokiem et al. 2005). Since we start from the parameter set as provided by Mok07 (highest 'fitness'¹⁷ with re-

spect to their assumptions), our new solution should be located at or close to the *global* maximum of the corresponding merit function as well and not only at a local one. Note that our derivation of nitrogen abundance and micro-turbulence for most of the cooler sample stars relies on a more objective method (Sect. 4.4).

Mok07 themselves used an automated fitting method (developed by Mokiem et al. 2005) based on a genetic algorithm optimization routine to obtain the stellar/wind parameters by evolving a population of FASTWIND models over a course of generations, until the best fit to H/He is found. Seven free parameters were considered to obtain the highest 'fitness': effective temperature, T_{eff} , surface gravity, $\log g$, helium content, Y_{He} , projected rotational velocity, $v \sin i$ (see above), micro-turbulent velocity, v_{mic} , mass-loss rate, \dot{M} , and velocity-field exponent, β .

4.2. Model calculations and grids

All models used within this analysis are calculated with FASTWIND, augmented by few CMFGEN models for comparison purposes (Sect. 5). For these calculations, H, He and N are treated as explicit elements. A description of our H/He model atoms can be found in Puls et al. (2005), and our nitrogen model atom has been described in Sect. 2.2 and in Paper I.

To allow us for studying the combined reaction of all diagnostic H/He/N lines on variations of the stellar/wind parameters and nitrogen abundances, and also for understanding the N IV $\lambda 4058$ emission line process (Sect 2.4), we generated a grid of models.¹⁸ The grid is constructed using various nitrogen abundances centered at the solar value $[\text{N}] = 7.78$ (from $[\text{N}] = 6.98$ to 8.58 with step size 0.2 dex and including the LMC nitrogen baseline abundance, $[\text{N}]_{\text{baseline}} = 6.9$), and a background metallicity, $Z = 0.5Z_{\odot}$, corresponding roughly to the *global* metallic abundance of the LMC (cf. Mokiem et al. 2007b). The individual abundances of the background elements (in terms of mass fractions) are scaled by the same factor with respect to the solar abundance pattern (see Massey et al. 2004).

For a given Z , the grid is three-dimensional with respect to T_{eff} , $\log g$, and $\log Q$, where Q is the so-called wind-strength parameter (or optical depth invariant), $Q = \dot{M}/(v_{\infty}R_*)^{1.5}$. This parameter allows us to condense the dependence on \dot{M} , terminal velocity, v_{∞} , and stellar radius, R_* , into one representative quantity.¹⁹ The grids cover the temperature range from 25 to 55 kK (with increments of 1 kK), and a gravity range between 3.0 and 4.5 (with increments of 0.2 dex). For $\log Q$, the different wind strengths are denoted by a letter (from 'A' to 'E'), with $\log Q = -14.0, -13.5, -13.15, -12.8, -12.45$, respectively, if \dot{M} is calculated in $M_{\odot}\text{yr}^{-1}$, v_{∞} in km s^{-1} , and R_* in R_{\odot} . Models with quantifier 'A' correspond to thin winds, resulting in lines that are (almost) unaffected by the wind, whereas 'E'-models correspond to a significant wind-strength typical for O-type supergiants. Other parameters have been adopted as follows: a solar helium abundance, $Y_{\text{He}} = 0.10$; v_{esc} as a function of the photospheric escape velocity, v_{esc} (see Kudritzki & Puls 2000); the stellar radius, R_* , as a function of spectral type and luminosity class, corresponding to prototypical values; the velocity field exponent, β , from empirical values (Kudritzki & Puls 2000), with $\beta = 0.9$ for O-stars, and higher values towards later types; and the micro-turbulence, $v_{\text{mic}} = 10 \text{ km s}^{-1}$.

¹⁶ In particular at earliest spectral types, the sensitivity of H/He on changes in the atmospheric parameters is rather weak.

¹⁷ which quantifies the quality of the solutions resulting from a genetic algorithm optimization, see Mokiem et al. (2005) and references therein.

¹⁸ following the basic philosophy described by Puls et al. (2005).

¹⁹ relying on the fact that the wind-emission from recombination dominated (i.e., ρ^2 -) processes remains unaffected as long as the wind-strength parameter does not vary (see Puls et al. 1996, 2005).

Table 4. Fundamental parameters for the LMC sample, assuming unclumped mass-loss.

Star	ST	Secondary T_{eff} diag.	T_{eff} (kK)	$\log g$ (cgs)	$\log g_{\text{true}}$ (cgs)	R_* (R_{\odot})	$\log L_*$ (L_{\odot})	Y_{He}	v_{mic} (km s^{-1})	$v \sin i$ (km s^{-1})	v_{mac} (km s^{-1})	\dot{M} ($10^{-6} M_{\odot} \text{yr}^{-1}$)	β	v_{∞} (km s^{-1})
N11-026	O2 III(f [*])	N III/N IV/N V	49.0	4.00	4.00	11.3	5.82	0.10	10.0	72	60	1.56	1.08	[3120]
		N IV/N V	52.0	4.10	4.10	11.0	5.89					1.49		
N11-031	ON2 III(f [*])	N III/N IV	47.8	3.95	3.95	13.4	5.92	0.11	10.0	71	60	2.02	1.08	3200
		N IV/N V	56.0	4.00	4.00	12.2	6.12					2.20		
N11-038	O5 II(f ⁺)	N III/N IV	40.5	3.70	3.71	14.0	5.67	0.08	10.0	100	50	1.21	0.98	[2600]
Sk-66° 100	O6 II(f)	N III/N IV	39.0	3.70	3.71	13.7	5.59	0.19	10.0	59	60	0.83	1.27	2075
N11-032	O7 II(f)	N III/N IV	36.0	3.50	3.51	13.6	5.44	0.09	10.0	60	70	0.97	0.80	[1920]
N11-045	O9 III	-	32.3	3.32	3.33	12.0	5.15	0.07	10.0	64	80	0.69	0.80	[1550]
BI253	O2 V((f [*]))	N IV/N V	54.8	4.18	4.20	10.7	5.97	0.08	10.0	230	-	1.53	1.21	3180
BI237	O2 V((f [*]))	N IV/N V	53.2	4.11	4.12	9.7	5.83	0.09	10.0	140	-	0.62	1.26	3400
N11-060	O3 V((f [*]))	N III/N IV/N V	48.0	3.97	3.97	9.5	5.63	0.12	10.0	68	40	0.51	1.26	[2740]
		N IV/N V	51.0	4.10	4.10	9.2	5.71					0.48		
Sk-70° 69	O5 V((f))	N III/N IV	42.3	3.93	3.94	9.1	5.38	0.14	10.0	131	-	0.43	0.80	2750
N11-051	O5 Vn((f))	N III/N IV	41.4	3.70	3.83	8.6	5.42	0.08	10.0	350	-	0.41	0.80	[2110]
N11-058	O5.5 V((f))	N III/N IV	40.8	3.75	3.76	8.4	5.24	0.10	6.0*	62	60	0.01	1.00	[2470]
Sk-66° 18	O6 V((f))	N III/N IV	39.7	3.76	3.76	12.2	5.52	0.14	10.0	75	40	1.08	0.94	2200
N11-065	O6.5 V((f))	N III/N IV	41.0	3.85	3.85	7.4	5.14	0.13	10.0	60	50	0.05	1.00	[2320]
N11-066	O7 V((f))	N III/N IV	37.0	3.70	3.71	7.9	5.02	0.10	10.0	59	50	0.14	0.80	[2315]
N11-068	O7 V((f))	N III/N IV	37.0	3.70	3.71	7.5	4.98	0.10	10.0	30	50	0.13	1.12	[3030]
N11-061	O9 V	-	34.0	3.55	3.55	11.5	5.20	0.09	5.0	54	80	0.52	0.80	[1900]
N11-123	O9.5 V	-	34.3	4.20	4.21	5.4	4.56	0.09	10.0	115	-	0.08	0.80	[2890]
N11-087	O9.5 Vn	-	32.7	4.04	4.08	8.8	4.90	0.10	10.0	260	-	0.11	0.80	[3030]
N11-029	O9.7 Ib	N II/N III	29.0	3.20	3.21	15.8	5.20	0.08	10.0	46	60	0.28	1.23	[1580]
N11-036	B0.5 Ib	N II/N III	25.8	3.11	3.11	15.5	4.98	0.08	12.1*	39	40	0.11	0.80	[1710]
N11-008	B0.7 Ia	N II/N III	26.3	3.00	3.00	29.5	5.57	0.10	4.7*	46	60	0.62	1.30	[2390]
N11-042	B0 III	N II/N III	29.2	3.59	3.59	11.9	4.97	0.08	5.0	21	25	0.19	1.19	[2310]
N11-033	B0 III _n	-	26.7	3.20	3.34	15.7	5.05	0.10	5.0	256	-	0.25	1.03	[1540]
N11-072	B0.2 III	N II/N III	29.8	3.70	3.70	8.1	4.67	0.10	2.7*	14	10	0.25	1.30	[2100]

Notes. $\log g_{\text{true}}$ is the surface gravity corrected for centrifugal effects. Secondary T_{eff} diagnostics, used in parallel with the He I/He II ionization equilibrium, is indicated for each star. For three stars, two parameter sets are provided, due to problems of reaching a simultaneous fit for all considered lines from three ionization stages. For N11-026 and N11-060, the first entry is our preferred one, and the second entry is a (disfavoured) alternative, whilst for N11-031 we consider both solutions as possible. (see Sect. 5). Brackets around v_{∞} : derived from scaling via v_{esc} . Asterisks following v_{mic} : value obtained in parallel with nitrogen abundance. For errors, see text.

4.3. Determination of stellar and wind parameters

The different steps performed in our analysis can be summarized as follows, and are detailed in the next sections.

First, we determine $v \sin i$ for each object. Then we use the results from Mok07 in combination with our model grid to roughly constrain the stellar (T_{eff} , $\log g$, [N]) and wind-strength parameters ($\log Q$), by inspecting the synthetic and observed H/He and nitrogen line profiles (Y_{He} , β and v_{mic} already specified within the grid.) During this step, we determine the extra line-broadening parameter, v_{mac} , by reproducing the profile shape of the weaker lines.

Subsequently, the stellar/wind parameters, now including Y_{He} and β , are fine-tuned by calculating a grid of much higher resolution around the initial guess and adopting v_{∞} from Mok07. After the fundamental parameters have been fixed and, in case, v_{mac} has been adjusted, we fit the nitrogen abundance, using two different methods (for cooler and hotter objects, respectively), and also update v_{mic} , which Mok07 solely derived from H/He lines. In certain cases, we need to re-adapt the stellar/wind parameters to obtain the (almost) final solution. Now, we are able to calculate the stellar radius from M_V and the synthetic fluxes, and we can update the mass-loss rate to its final value, by scaling with the new radius. A final consistency check with the new M and R_* values is performed to ensure the stability of our results.

Tables 4 and 6 list all quantities derived in this way, and Table 5 yields the main differences between our and the Mok07

results. Note that these quantities refer to unclumped winds, whilst in Sect. 4.5.1 we discuss the impact of wind clumping.

Projected rotational velocities and macro-turbulence. Before we are able to perform the actual (fine-)analysis, we need to constrain the line broadening parameters, i.e., $v \sin i$ and v_{mac} (v_{mic} will be - when possible - inferred in parallel with the nitrogen abundances, see Sect 4.4). As outlined above, Mok07 derived $v \sin i$ directly from their automated fitting method, from the H/He lines. More suitable is to use metal lines, since these are not affected by Stark-broadening. Only in case of high rotational velocities or high temperatures, where metallic lines are blended or are very weak, He I lines might be used. Thus, we derived $v \sin i$ from scratch, employing the Fourier method (Gray 1976), as implemented and tested in the OB-star range by Simón-Díaz et al. (2006) and Simón-Díaz & Herrero (2007). This method has the advantage to easily discriminate the rotational contribution from other broadening mechanisms that affect the line shapes. In dependence of temperature and rotational velocity of the star, we used lines from O II, N II, C II, and Si III for B- and late O-type stars. For earlier O-types, higher ionization states are predominant, and mostly N III/N IV and Si IV lines have been considered, together with He I lines for the earliest types.

To finally reproduce the actual profile shape, in most cases some extra line-broadening is needed, conventionally called macro-turbulence. Though the physical origin of this broaden-

ing remains still to be proven, there are some strong indications that it is associated with (high order, non-radial) stellar pulsations (Aerts et al. 2009; Simón-Díaz et al. 2010). To account for this effect, we used a radial-tangential description of v_{mac} to fit the profile *shapes* of nitrogen (and partly helium) lines, using our first estimates on the stellar and wind parameters (see above) and the new $v \sin i$ values. For the fastest rotators of our sample, however, corresponding values could not be constrained, since large $v \sin i$ produce either too weak nitrogen lines, or these lines, together with He I lines, loose their sensitivity to distinct changes in v_{mac} .

As expected, most of our $v \sin i$ values turn out to be systematically lower than those provided by Mok07 (Table 5), by typically 30-40%. The derived range of v_{mac} values is consistent with results from similar investigations, e.g., Dufton et al. (2006); Simón-Díaz et al. (2006); Lefever et al. (2007); Markova & Puls (2008); Simón-Díaz et al. (2010). The uncertainty of our estimates is typically on the order of $\pm 10 \text{ km s}^{-1}$, being larger for stars with relatively low rotational speeds.

Effective temperatures. This parameter is mostly constrained by the He I/He II ionization equilibrium. For this purpose, we primarily use He I $\lambda\lambda$ 4471, 4713, 4387 and He II $\lambda\lambda$ 4200, 4541. In most cases, we did not meet the so-called He I singlet problem (Najarro et al. 2006). As a consistency check on T_{eff} and especially for the hotter stars, where the He I lines can no longer serve as an efficient temperature indicator, we make additional use of the nitrogen ionization equilibrium, by means of the lines listed in Table 2. For B- and late O-stars, we investigate N II/N III, for mid O-stars N III/N IV, and for early O-stars N IV/N V or even - in a few cases -N III/N IV/N V (see Table 4 for the specific diagnostics applied to a particular object). To this end, we either use our coarse grid or our specific ‘fine-grid’ models, with a similar gridding of nitrogen abundances ($[N] = 6.9 \dots 8.58$). By exploiting this additional information, i.e., roughly ‘fitting’ the nitrogen lines of different ions at a unique abundance, we are able to fine-tune T_{eff} (and also some of the other parameters, see below). For objects where only lines from one ionization stage are present (N11-033, 045, 061, 087, 123), such a consistency check only allows for rather weak constraints, if at all.

We estimate a typical uncertainty for T_{eff} according to the grid resolution, $\Delta T_{\text{eff}} \approx 1 \text{ kK}$. For N11-066 and N11-068 we can only provide rough estimates on the stellar parameters, consistent with the nitrogen ionization equilibrium, and we adopt a larger error, $\Delta T_{\text{eff}} \approx 2 \text{ kK}$. For some problematic stars, N11-026, N11-031, and N11-060, we consider an even larger error, about 4 kK, in agreement with Mok07 (see Sect. 5).

Surface gravities. We derived $\log g$ using the classical approach, from the Stark-broadened wings of the Balmer lines, basically H γ and H δ , which should be uncontaminated by wind-emission. As for T_{eff} , we use nitrogen lines as a final consistency check. These surface gravities need to be corrected for stellar rotation, applying a centrifugal correction (see Repolust et al. 2004 and references therein). The estimated error for $\log g$ is 0.1 dex.

Helium abundances. To ensure the reliability of the final parameters, especially T_{eff} and $\log g$, and for our discussion on the abundance enrichment, we need to revisit the helium line fits, since inconsistent helium abundances can influence these parameters. A small sub-grid was constructed around the stellar parameters derived in previous steps, for different Y_{He} , from 0.08

Table 5. Differences between the fundamental parameters as derived here and by Mok07.

Star	ΔT_{eff} (kK)	$\Delta \log g$ (cgs)	ΔY_{He}	$\Delta v \sin i$ (km s^{-1})	$\Delta \log \dot{M}$ ($10^{-6} M_{\odot} \text{yr}^{-1}$)	$\Delta \beta$
N11-026	-4.3	-	-0.01	-37	-0.06	-
N11-031	2.8	0.10	0.01	-45	-0.28	0.19
N11-038	-0.5	-0.02	-0.02	-45	-0.10	-
Sk-66° 100	-	-	-	-25	-0.03	-
N11-032	0.8	0.05	-	-36	0.08	-0.23
N11-045	-	-	-	-41	0.10	-
BI253	1.0	-	-0.01	39	-0.10	-
BI237	-	-	-0.01	14	-0.10	-
N11-060	2.3	0.05	-	-38	-0.01	-
Sk-70° 69	-0.9	0.06	-0.03	-	-0.38	0.02
N11-051	-1.0	-0.05	-	17	-0.39	0.20
N11-058	-0.5	-0.14	-	-23	-1.18	-0.42
Sk-66° 18	-0.5	-	-	-7	-	-
N11-065	-0.7	-0.04	-0.04	-23	-0.86	0.20
N11-066	-2.3	-0.17	-0.01	-12	-0.47	-
N11-068	-2.9	-0.43	-	-24	-0.42	-
N11-061	0.4	0.04	-	-33	0.39	-1.00
N11-123	-0.5	-0.02	-	5	-	-
N11-087	-	-	-	-16	-0.10	-
N11-029	-0.4	-0.03	0.01	-31	0.22	-0.40
N11-036	-0.5	-0.20	-	-15	-	-
N11-008	0.3	0.02	-	-35	0.09	-0.57
N11-042	-1.0	-0.10	-0.02	-21	-0.02	-
N11-033	-0.5	-0.01	0.02	-	0.02	-
N11-072	-1.0	-0.08	-0.02	-	0.02	0.46

Notes. Positive values indicate larger values from this study. Dashes: no difference compared to the Mok07 analysis. For N11-031, the comparison is made with respect to the cooler solution (see Sect. 5).

(corresponding to the approximate LMC baseline abundance, see Sect. 6) to 0.14, in steps of 0.02. A rough estimate on the error is half this stepsize.

Terminal velocities cannot be reliably derived from the optical, and have been adopted from Mok07. For the field stars, values have been inferred from UV P Cygni profiles, by Massa et al. (2003) and Massey et al. (2005). For Sk-66° 18, it was measured by Mok07 using UV O VI lines. For the FLAMES N11 stars, only N11-031 could be analyzed with respect to this parameter, by Walborn et al. (2004). For all other stars, v_{∞} has been estimated from v_{esc} , following Kudritzki & Puls (2000).

Velocity field exponent β . The sample used within this study does not contain any star with such a dense wind that H α is in emission, therefore an accurate determination of this parameter is difficult²⁰ for optical spectroscopy. We applied the following philosophy. If the combination \dot{M} - β provided by Mok07 resulted in reasonable H α -fits, we kept β . Otherwise, we set β to prototypical values, $\beta = 0.8 \dots 1.30$, in dependence of spectral type and results from earlier analyses performed in our group. Moreover, for some of the sample stars, N11-008, N-029, N11-058, and N11-061, the automated fitting method used by Mok07 resulted in quite large values for β (e.g., N11-061: $\beta=1.8$), whilst for N11-051 a rather low value, $\beta = 0.6$, was inferred. We consider such values as either unphysical or indicating a substantial amount

²⁰ if not impossible, due to the \dot{M} - β degeneracy (e.g., Markova et al. 2004), and effects from wind clumping (e.g., Puls et al. 2006).

of wind clumping. In all these cases, we modified β as outlined above (see also Sect. 5).

Mass-loss rates are derived from fitting the synthetic H_α profiles to the observations, given β (see above). Usually He II $\lambda 4686$ is used as a consistency check. It turned out that for many sample stars we were not able to successfully fit both lines at the same \dot{M} , since He II $\lambda 4686$ showed more absorption than consistent with the observations when H_α was fitting. This might indicate a certain problem regarding He II $\lambda 4686$ in the new FASTWIND version, or some impact of wind clumping. The problem needs to be investigated in future, but has no impact within the present study.

Another consistency check for \dot{M} is provided by the nitrogen lines, particularly by the N III and N IV emission lines (and sometimes also by the N V doublet), which are strongly affected by the wind strength. In the case of two stars, N11-058 and N11-065, which showed quite good line fits to H, He and N, the synthetic N IV $\lambda 4058$ profile displayed weak emission, whereas the observed one was clearly in weak absorption. Consistency could be achieved by lowering \dot{M} until this line could be acceptably fitted, leaving the remaining nitrogen lines and H_α almost unaltered. In both cases it turned out that H_α was already almost insensitive to reductions in \dot{M} . Other stars which showed a similar problem, N11-051, Sk-66° 18, and Sk-66° 100, could not be ‘cured’ by this approach, since in this case a reduced value of \dot{M} was no longer consistent with (unclumped!, see Sect. 4.5.1) H_α .

Since in all of our objects H_α is in absorption, leading to the well known \dot{M} - β degeneracy, we estimate quite a large error on \dot{M} , namely plus/minus a factor of two, which is typical in this situation (e.g., Markova et al. 2004). The impact of the error in R_* is negligible here, as outlined in the next paragraph.

Stellar radii. Since the effective temperatures derived within this work are different from those of Mok07 (overall, these differences are modest, except for N11-026, N11-031, and N11-068, see Table 5), this leads to different theoretical fluxes and thus to different stellar radii. Similar to Mok07, we followed Kudritzki (1980) and Herrero et al. (1992), and calculated the ‘new’ radii from the theoretical Eddington fluxes and the (de-reddened) absolute magnitudes from Table 3.

Once the radii have been re-determined, \dot{M} needs to be modified as well, to preserve the fit quality of H_α , which depends on the optical depth invariant Q (see above). Contrasted to the case of Galactic objects, where the error of M_V (due to unknown distances) dominates the error budget of \dot{M} , this plays a secondary role in our sample, due to sufficiently well-known distances and the rather large error introduced by the \dot{M} - β degeneracy.

4.4. Nitrogen abundances and micro-turbulences

After having determined the stellar and wind parameters and their uncertainties (some fine-tuning might still be necessary), we are now in a position to derive the nitrogen abundances and the corresponding micro-turbulent velocities, v_{mic} . Because the latter parameter significantly affects the strength of both He and metal lines and thus the implied abundances, it is useful to determine both quantities in parallel.

To carry out this analysis, we calculate a fine grid of typically 25 models, by combining different abundances centered at the rough estimates derived in Sect. 4.3, with five different values for $v_{\text{mic}} = 0.5, 1.0, 1.5, 2.0 \text{ km s}^{-1}$.

Table 6. Helium and nitrogen abundances for the LMC sample, with stellar parameters from Table 4.

Star	$v \sin i$	Y_{He}	[N]	$\Delta[\text{N}]$	$\Delta[\text{N}]^{\text{cl}}$	Literature
N11-026	72	0.10	7.80 ¹ 7.75 ²	+0.40 +0.40	0.25-0.30	-
N11-031	71	0.11	7.83 ¹ 8.30 ²	± 0.15 ± 0.15	-	8.00 \pm 0.18
N11-038	100	0.08	7.85	± 0.15	0.05-0.10	-
Sk-66° 100	59	0.19	8.48 ³	± 0.15	-	-
N11-032	60	0.09	7.87	± 0.15	0.05-0.10	-
N11-045	64	0.07	6.98	± 0.20	-	-
BI253	230	0.08	7.90	± 0.15	0.15-0.20	-
BI237	140	0.09	7.38	± 0.15	0.05-0.10	-
N11-060	68	0.12	8.20 ¹ 8.15 ²	+0.30 +0.30	0.05-0.10	-
Sk-70° 69	131	0.14	8.05 ³	± 0.15	0.15-0.20	-
N11-051	350	0.08	7.58 ³	± 0.20	-	-
N11-058	62	0.10	8.09	± 0.15	-	-
Sk-66° 18	75	0.14	8.48 ³	± 0.15	-	-
N11-065	60	0.13	8.17 ³	± 0.15	0.05-0.10	-
N11-066	59	0.10	8.17	± 0.20	0.05-0.10	-
N11-068	30	0.10	7.85	± 0.20	0.05-0.10	-
N11-061	54	0.09	7.18	± 0.15	-	-
N11-123	115	0.09	7.00	± 0.15	-	-
N11-087	260	0.10	7.38	-0.20 ⁴	-	-
N11-029	46	0.08	7.43	± 0.15	-	7.10 \pm 0.35
N11-036	39	0.08	7.85	± 0.17	-	7.76 \pm 0.11
N11-008	46	0.10	8.08	± 0.11	-	7.84 \pm 0.11
N11-042	21	0.08	7.00	± 0.15	-	6.92 \pm 0.24
N11-033	256	0.10	7.28	-0.20 ⁴	-	-
N11-072	14	0.10	7.68	± 0.15	-	7.38 \pm 0.06

⁽¹⁾ From N III/N IV, uncertainty from N V.

⁽²⁾ From N IV/N V, uncertainty from N III.

⁽³⁾ Improvement of N IV $\lambda 4058$ fit with weak clumping.

⁽⁴⁾ Uncertainty of upper limit.

Notes. [N] is our best-fitting value, $\Delta[\text{N}]$ the corresponding uncertainty, and $\Delta[\text{N}]^{\text{cl}}$ the change in [N] (always positive) if clumping with $f_\infty = 0.1$ is included in the models (Sect. 4.5.1). Values displayed in italics have been derived by the ‘curve-of-growth’ method. Literature values are from Walborn et al. (2004) for N11-031 and from Hunter et al. (2009) for the B-stars and N11-029. When two entries are provided, the first one corresponds to our preferred solution, except for N11-031 where we consider both solutions as possible.

When possible (see below), we use a ‘curve of growth’ method based on the equivalent widths of the lines, which has been applied in the past years to different sets of B-stars for obtaining various metallic abundances (e.g., Urbaneja 2004; Simón-Díaz et al. 2006; Markova & Puls 2008). In brief, this method uses synthetic and observed equivalent widths including uncertainties from *all* considered lines, to derive a unique pair of abundance and v_{mic} (incl. errors). Results from such analyses are indicated by an asterisk in the v_{mic} -column of Table 4.

Unfortunately, this procedure was not applicable to the bulk of the sample stars because of various reasons, e.g., blending and diluted lines due to fast rotation, almost invisible lines due to low nitrogen content, and peculiarities in the observed lines from some of the stars with highly ionized nitrogen. All these problems will be commented on in Sect. 5, and we opted for a determination of the nitrogen abundance/micro-turbulence pair by means of a visual inspection of the fit quality, using the same fine grid as described above.

We estimate the errors in v_{mic} as 3-5 km s^{-1} , both for the equivalent width and the visual method. To provide an impres-

sion on the impact of such errors on the derived nitrogen abundances, we note that a decrease in v_{mic} by 5 km s^{-1} leads to an increase of $[\text{N}]$ by 0.05-0.07 dex. For the error associated to $[\text{N}]$ when derived by ‘visual’ fitting, we decided to be quite conservative. Even though we are able to obtain quite good fits for the bulk of the stars implying an uncertainty of 0.1 dex, we rather adopt a larger value of 0.15 dex to roughly account for the additional dependence on the stellar and wind parameters. For two stars, N11-033 and N11-087, we can only provide an upper limit on the abundance, with an estimated uncertainty of 0.20 dex. This value is also adopted for N11-066, N11-068, and N11-045, N11-051. For the first two stars only rough estimates on their stellar parameters could be obtained, and for the latter two only one nitrogen multiplet could be used. Even larger uncertainties have been derived for two ‘problematic’ stars, N11-026 and N11-060, see Sect. 5.

Table 6 lists the obtained nitrogen abundances together with their estimated errors. When available, corresponding literature values have been added.

4.5. Additional considerations

4.5.1. Wind clumping

So far, we neglected wind clumping in our analysis. Since most of the nitrogen lines are formed in the intermediate or outer photosphere,²¹ at least for not too extreme winds as considered here, they should remain rather unaffected by *direct* clumping effects, though indirect effects could be important (see Paper I). Clumped winds have lower mass-loss rates compared to their unclumped counterparts, by a factor of $1/\sqrt{f_{\text{cl}}}$ if the clumping factor f_{cl} were radially constant, which could influence both the N III and the N IV emission lines, due to their sensitivity on \dot{M} . Given the multitude of evidence for wind-clumping (e.g., Puls 2008 and references therein), it is necessary to examine the impact of clumping on our abundance determinations.

We adopt the parametrization as used by Hillier & Miller (1999) and Hillier et al. (2003),

$$f(r) = f_{\infty} + (1 - f_{\infty}) \exp(-v(r)/v_{\text{cl}}) \quad (1)$$

where $f(r)$ is the volume filling factor,²² f_{∞} its asymptotic value (if $v_{\infty} \gg v_{\text{cl}}$) and v_{cl} the velocity where the volume filling factor reaches values close to e^{-1} , if $f_{\infty} \ll 1$. To allow for maximum effects, we set $v_{\text{cl}} = 30 \text{ km s}^{-1}$, close to the sonic speed for O-stars, and concentrated on models with $f_{\infty} = 0.1$, corresponding to \dot{M} reductions by a factor of roughly 0.3 (consistent with recent investigations allowing for macro-clumping, see Sundqvist et al. 2011).

Since most of our sample stars display thin winds, no major reaction due to clumping is to be expected. Indeed, a value of $f_{\infty} = 0.1$ did not induce any noticeable change in the spectrum for the bulk of the stars.

For stars N11-038, 032, BI237, N11-060, 065, 066, and 068, mostly the N III triplet is affected (for BI237, also N V), requiring 0.05 to 0.1 dex more nitrogen to preserve the *previous* fit quality of these lines. Since, on the other hand, the other nitrogen lines remain unmodified, the inclusion of clumping did not change our $[\text{N}]$ -values for these stars, but only improves or deteriorates the particular representation of the triplet lines.

²¹ Note that this might no longer be true for the N V doublet, e.g., N11-031.

²² which is, within the standard assumption of micro-clumping and a void inter-clump medium, the inverse of the clumping factor f_{cl} .

For BI253 and Sk-70° 69, clumping of the considered amount has a larger effect, particularly on the N III triplet, N IV $\lambda 4058$ and the N V doublet. Here, a clumping factor of $f_{\infty} = 0.1$ requires that $[\text{N}]$ needs to be increased by 0.15... 0.20 dex.

Finally, for N11-026 and N11-031, the inclusion of clumping affects the stellar parameters as well. Due to the lower \dot{M} , a hotter temperature (by 1 to 2 kK) is needed to preserve the He I fit. In case of N11-026 then, $[\text{N}]$ needs to be considerably increased, by 0.25 to 0.3 dex. This is the only case where we encountered a significant effect. For N11-031, on the other hand, at least the ‘cool solution’ (see Sect. 5) remained at the previous nitrogen abundance.

Besides these general effects, for a few stars, Sk-66° 100, Sk-70° 69, N11-051, Sk-66° 18 and N11-065, the inclusion of clumping (of a lesser degree than $f_{\infty} = 0.1$) favours a better fit to N IV $\lambda 4058$, see Sect 5.

4.5.2. Background abundances

One of the central results from Paper I was that the N III triplet emission increases with decreasing background metallicity, Z , due to reduced line-blocking. In this investigation we assume, following Mokiem et al. (2007b), a *global* Z of the LMC, $Z = 0.5 Z_{\odot}$. Since this value is somewhat controversial, and a $Z = 0.4 Z_{\odot}$ might be appropriate as well (e.g., Dufour 1984), we need to test the impact of this difference on the derived nitrogen abundances.

Overall, such lower background Z does not produce any extreme changes. As expected, the triplet emission increases, requiring a roughly 0.05 dex lower abundance to recover the previous fits. Interestingly, we also found that N IV $\lambda 4058$ and the N III quartet lines tend to more emission and weaker absorption, respectively, but to a lesser extent. The effect on the remaining nitrogen lines is marginal. Note that a lower $[\text{N}]$ value due to lower background abundances would partly cancel with the corresponding increase in the derived $[\text{N}]$ due to moderately clumped winds.

5. Comments on the individual objects

In the following, we give specific comments on the individual objects, regarding peculiarities and problems found during our analysis. We separate between B-/late O-stars and (hotter) O-stars, and sort by luminosity class and spectral type, starting at the hotter side. All nitrogen line fits (including corresponding limits according to Table 6) are displayed in Appendix. C, except for the objects N11-072, N11-032, and BI237 which have been included in the main paper, since they are exemplary for objects with different features. All spectra are corrected for radial velocity shifts.

We selected those lines that were clearly visible, at least in most of the cases. In particular, for $T_{\text{eff}} \leq 35 \text{ kK}$, we used N II $\lambda\lambda$ 3995, 4447, 4601, 4607, 4621, 4630 and N III $\lambda\lambda$ 4003, 4097, 4195, 4379, $\lambda\lambda$ 4634 – 4640 – 4642, and $\lambda\lambda$ 4510 – 4514 – 4518. For $T_{\text{eff}} > 35 \text{ kK}$, we analyzed the lines from N III/N IV/N V: N III as before, N IV $\lambda\lambda$ 4058, 6380, and N V $\lambda\lambda$ 4603 – 4619 (see Table 2). Additionally, the N IV multiplets around 3480 Å and 7103-7129 Å have been used for the field stars observed with UVES (except for Sk-70° 69 where only N IV λ 3480 is available).

5.1. Late O- and B-supergiants/giants

5.1.1. Supergiants

N11-029 – O9.7 Ib. This is the only O-supergiant within our sample. Since it is of late nature, we discuss it here together with the B-supergiants. No major problem has been encountered, and the largest difference with respect to Mok07 concerns the large $\beta = 1.63$ derived in their analysis. We opted for a lower value, $\beta = 1.23$, still at the limit of prototypical values. To compensate for this modification, \dot{M} needs to be somewhat increased.

Figure C.1 shows the best fit for the nitrogen lines. An abundance of $[N] = 7.43 \pm 0.15$ has been inferred, mainly from $N_{II}\lambda 3995$ and the N_{III} quartet lines. The bulk of the N_{II} lines are not helpful since there are blended by O_{II} (Table 2). This is also the case for most of the N_{III} lines.

The most interesting feature, however, is the discrepancy for $N_{III}\lambda 4634$,²³ which shows an almost completely refilled profile but is predicted to be in absorption. To synthesize a profile with $E.W. \approx 0$ would require a higher T_{eff} or a lower $\log g$, inconsistent with the He ionization equilibrium. This seems to be the first observational evidence for one of the problems discussed in Paper I. For a certain temperature range (around 30 to 35 kK), FASTWIND spectra predict too few emission in the N_{III} triplet, compared to results from CMFGEN, due to (still) missing overlap effects between the N_{III} and O_{III} resonance lines around 374 Å (which are treated consistently in CMFGEN; for details, see Paper I).

For further tests, we calculated a CMFGEN model at the same stellar/wind parameters and abundances as derived in the present analysis. As expected, the corresponding synthetic profiles are closer to the observations (though still not as refilled as observed). To check whether the oxygen abundance plays a significant role, two different abundances were considered, $[O] = 8.66$ and 8.30 dex (solar and factor two lower). In agreement with our theoretical argumentation from Paper I, such a difference did not affect the predicted N_{III} triplet emission strength.

N11-036 – B0.5 Ib. The largest difference to Mok07 is that we derive a lower value for $\log g$ (by 0.2 dex) as well as a lower T_{eff} (by 500 K), by exploiting He I/He II in parallel with the N_{II}/N_{III} ionization equilibrium.

The nitrogen lines are well fitted, both for N_{II} and N_{III} (Fig. C.2). The only discrepancy found relates to an underprediction of absorption strength in $N_{II}\lambda 4607$, whereas the discrepancy at $N_{II}\lambda 4601$ is due to an O_{II} blend. Quite a large enrichment is found, $[N] = 7.85 \pm 0.17$.

N11-008 – B0.7 Ia. Again, we adapted the rather large velocity field exponent derived by Mok07, $\beta = 1.87$, to a more typical value of $\beta = 1.30$. We derive $v \sin i = 46 \text{ km s}^{-1}$, which is approximately half the value as obtained by Mok07, and compensate by invoking a $v_{\text{mac}} = 60 \text{ km s}^{-1}$.

The best fitting abundance, $[N] = 8.08 \pm 0.11$ (Fig. C.3), has been obtained by the ‘curve of growth method’, and yields reasonable fits except for $N_{II}\lambda 4447$, 4621, and $N_{III}\lambda 4003$ which are slightly overpredicted.

5.1.2. Giants

N11-042 – B0 III. We derive a lower projected velocity than Mok07, $v \sin i = 21 \text{ km s}^{-1}$, as well as a lower T_{eff} , together

with a corresponding decrease of $\log g$, for consistency with the N_{II}/N_{III} ionization equilibrium. For this cooler solution, the helium abundance needs to be lowered as well, $Y_{\text{He}} = 0.08$, close to the LMC He baseline abundance (see Sect. 6).

Due to the low rotational speed, we are able to clearly inspect all N_{II} and N_{III} lines (Fig. C.4) which are fitted almost perfectly. The only discrepancy occurs at $N_{III}\lambda 4097$, caused by a coincident O_{II} line. We are able to see two strong O_{II} absorption lines at both sides of $N_{III}\lambda 4640$, and to the left of $N_{III}\lambda 4379$ (where the former cannot be used for the diagnostics of similar stars with rapid rotation, N11-008, N11-029, N11-036, and N11-045).

A low nitrogen content has been derived, $[N] = 7.00 \pm 0.15$, consistent with the low helium abundance.

N11-033 – B0 III_n. We find a slightly cooler T_{eff} compared to Mok07, and our helium line fits suggest $Y_{\text{He}} = 0.10$.

Due to its large rotation, all nitrogen lines are severely diluted and almost ‘vanish’ from the spectrum (Fig. C.5), implying an upper limit of $[N] = 7.28$ from the N_{II} lines.

N11-072 – B0.2 III. This object shows a very sharp-lined spectrum, with the lowest $v \sin i$ value within our sample. A consistent solution for nitrogen and helium suggests a slightly cooler T_{eff} (by 1 kK) and lower $\log g$ (by 0.1 dex). Our best fit indicates $Y_{\text{He}} = 0.10$.

As for the similar object N11-042, we are able to obtain a good fit from the ‘curve of growth’ method, with $[N] = 7.68 \pm 0.15$, and a rather low $v_{\text{mic}} = 2.7 \text{ km s}^{-1}$. Thus, and in contrast to N11-042, this object is clearly enriched. Note that N11-072 and N11-042 belong to different associations, LH-10 and LH-9, respectively.

5.2. O-stars

5.2.1. Giants

N11-026 – O2 III(f*). This star is one of the four O2 stars in our sample, together with N11-031, BI237, and BI253, comprising the hottest objects. Unlike Mok07, we favour a cooler solution, $T_{\text{eff}} = 49 \text{ kK}$ (Mok07: 53 kK), and a somewhat lower \dot{M} . This comparably large difference for T_{eff} relies both on the better reproduction of He I $\lambda 4471$ and on the fit to the nitrogen lines, with three ionization stages visible (Fig. C.6). Mok07 considered such cooler solution as well (almost included in their error bars), which would have improved their fit to He I $\lambda 4471$, but argued in favour of the hotter one, accounting for the global fit quality. By considering nitrogen now, we find support for a lower T_{eff} , since for $T_{\text{eff}} \geq 50 \text{ kK}$ the N_{III} lines vanish from the spectrum (cf. BI237 and BI253).

The derived nitrogen abundance results from a compromise solution, $[N] = 7.80$, where this value is also the lower limit. Moreover, we estimate quite a large uncertainty (upper limit) of 0.4 dex, arising from our difficulties to fit all three ionization stages in parallel. We favour a solution that provides a good fit for the N_{III} quartet and the N_{IV} lines, whereas a larger abundance, $[N] = 8.20$, is needed to fit the N_{V} doublet. From Fig. C.6 it is clear that such a large abundance (red) is in disagreement with the remaining nitrogen lines. Of course, we also tried a fit at hotter temperatures. At $T_{\text{eff}} = 52 \text{ kK}$ (close to the result by Mok07), $\log g = 4.1$ (which is still consistent with the Balmer line wings) and $\dot{M} = 1.5 \cdot 10^{-6} M_{\odot} \text{ yr}^{-1}$, it is possible to fit both N_{IV} and N_{V} , for quite a similar abundance, $[N] = 7.75$. At this

²³ similar to $N_{III}\lambda 4640$ which is strongly blended by O_{II} .

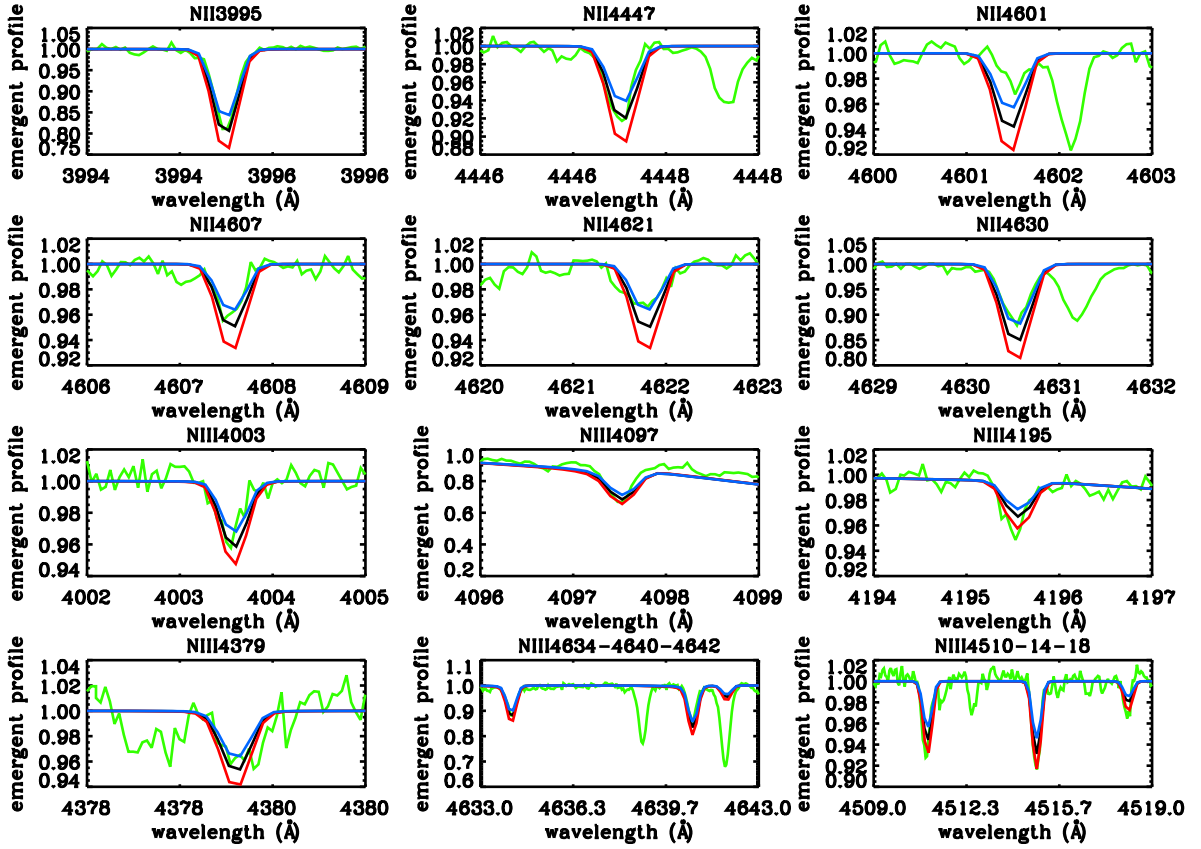


Fig. 5. N11-072 - B0.2 III. Observed (green) and best-fitting optical nitrogen spectrum (black). Blue and red spectra correspond to synthetic line profiles with $[N]$ at the lower and upper limit, respectively. For details, see Sect. 5.

temperature, however, all N III lines have vanished though. To recover them we would need to increase the abundance again, also by 0.4 dex. Because of the poorer prediction of He I $\lambda 4471$ we opt for the cooler solution. Since in both cases the implied nitrogen abundances are similar, this does not lead to severe problems for our further analysis, but requires larger error bars than typical.

N11-031 – ON2 III(f*). This star raised the most severe difficulties in our sample when trying to fit the nitrogen lines (Fig. C.7). Already its ‘ON’ designation indicates strong nitrogen features in its spectra, in this case N IV $\lambda 4058$, 3480 (for the latter, see Walborn et al. 2004), and the N V doublet lines. We were not able to consistently fit these strong features together with the remaining nitrogen lines. In contrast, N IV $\lambda 6380$ has almost the same strength as in N11-026.

If we try to reproduce the (rather weak, but clearly visible) He I $\lambda 4471$ in parallel with N III and N IV $\lambda 6380$, we obtain $T_{\text{eff}} = 47.8$ kK, a bit cooler than N11-026, whilst Mok07 derived $T_{\text{eff}} = 45$ kK, excluding T_{eff} values larger than 47 kK based on the helium ionization analysis.

If, on the other hand, we try to fit the problematic lines, we need a much higher T_{eff} . A consistent fit for all N IV lines (including N IV $\lambda 6380$) together with those from N V requires $T_{\text{eff}} = 56$ kK, $\log g = 4.00$, and $\dot{M} = 2.2 \cdot 10^{-6} M_{\odot} \text{yr}^{-1}$, together with a very high abundance, $[N] = 8.30$. Clearly, this set of stellar parameters neither reproduces the N III lines nor the weak He I $\lambda 4471$. N11-031 has been previously analyzed by Walborn et al. (2004) and Doran & Crowther (2011) using the N IV/N V lines (without discussion of He I and N III). The former authors obtained quite similar parameters, $T_{\text{eff}} = 55$ kK,

$\log g = 4.00$, and a somewhat lower $\dot{M} = 1.0 \cdot 10^{-6} M_{\odot} \text{yr}^{-1}$, presumably because of a clumped wind (though clumping has not been mentioned). At these parameters, they derived $[N] = 8.00 \pm 0.18$, which for our models would still be too low. Doran & Crowther (2011) only provided T_{eff} within their analysis, deriving $T_{\text{eff}} = 54.7$ kK for this object.

Because of the similarities with N11-026 (except for the two strong features), the fact that N IV $\lambda 6380$ ²⁴ behaves ‘normally’ and that He I $\lambda 4471$ is clearly visible, the cooler solution with $[N] = 7.83 \pm 0.15$ cannot be discarded so far. We checked our synthetic spectra by independent CMFGEN calculations. The results are quite similar, in particular the predicted N III emission lines are even a bit weaker than those produced by FASTWIND, again pointing to a cooler solution.

We also tried to attribute the problematic feature to the presence of X-rays, by means of CMFGEN calculations including typical X-ray strengths and distribution, but almost no effect on these lines has been found (basically because the line forming region is still inside or close to the photosphere).

Of course, it would be helpful to consider N IV $\lambda 3480$ as well, which unfortunately is not included in our dataset. A by-eye comparison with the corresponding profile displayed in Walborn et al. (2004, their Fig. 1) showed that both our cooler and hotter solutions are not incompatible with this spectrum.²⁵

²⁴ which turned out to be quite ‘reliable’ in the remaining objects, even for the hottest ones.

²⁵ Interestingly, our cooler solution predicts somewhat stronger absorption than the hotter one, even though the corresponding nitrogen abundance is significantly lower.

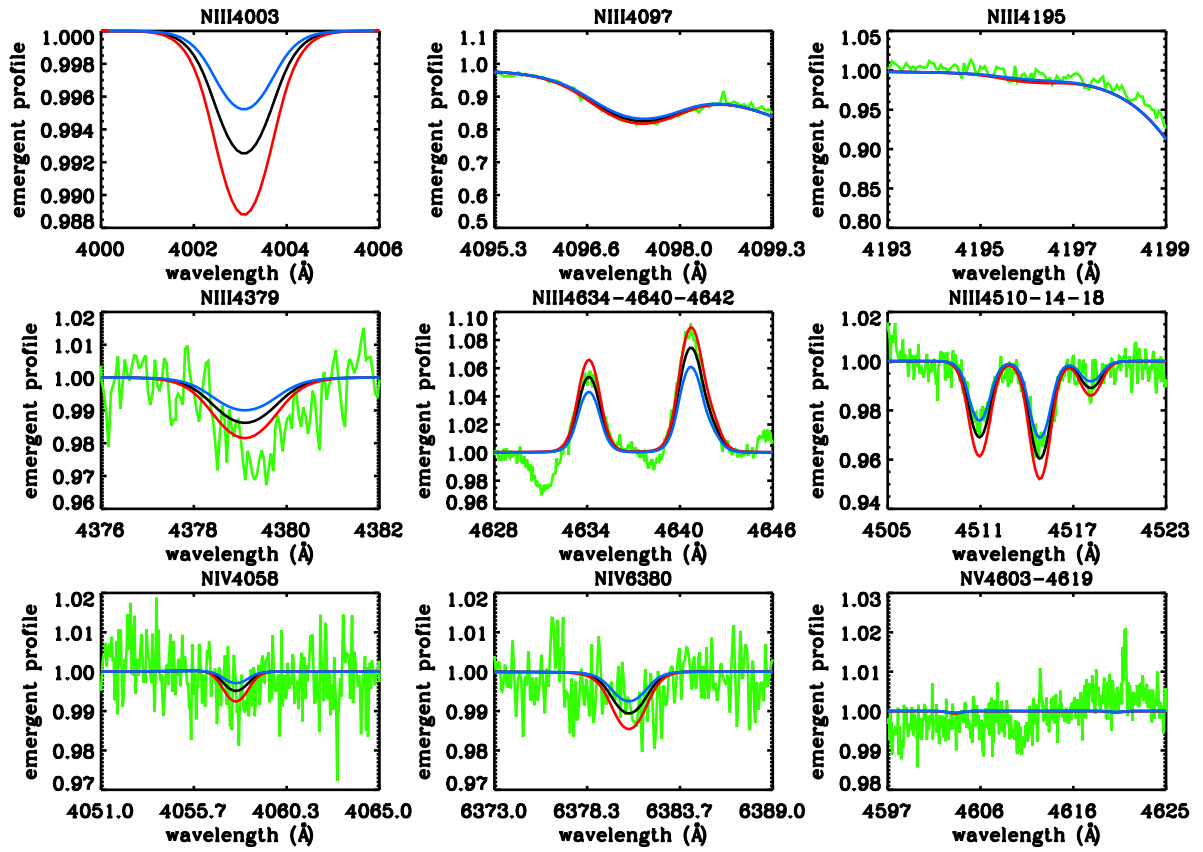


Fig. 6. N11-032 - O7 II(f). Same color coding as Fig. 5. For this star, N III λ 4003 has not been observed.

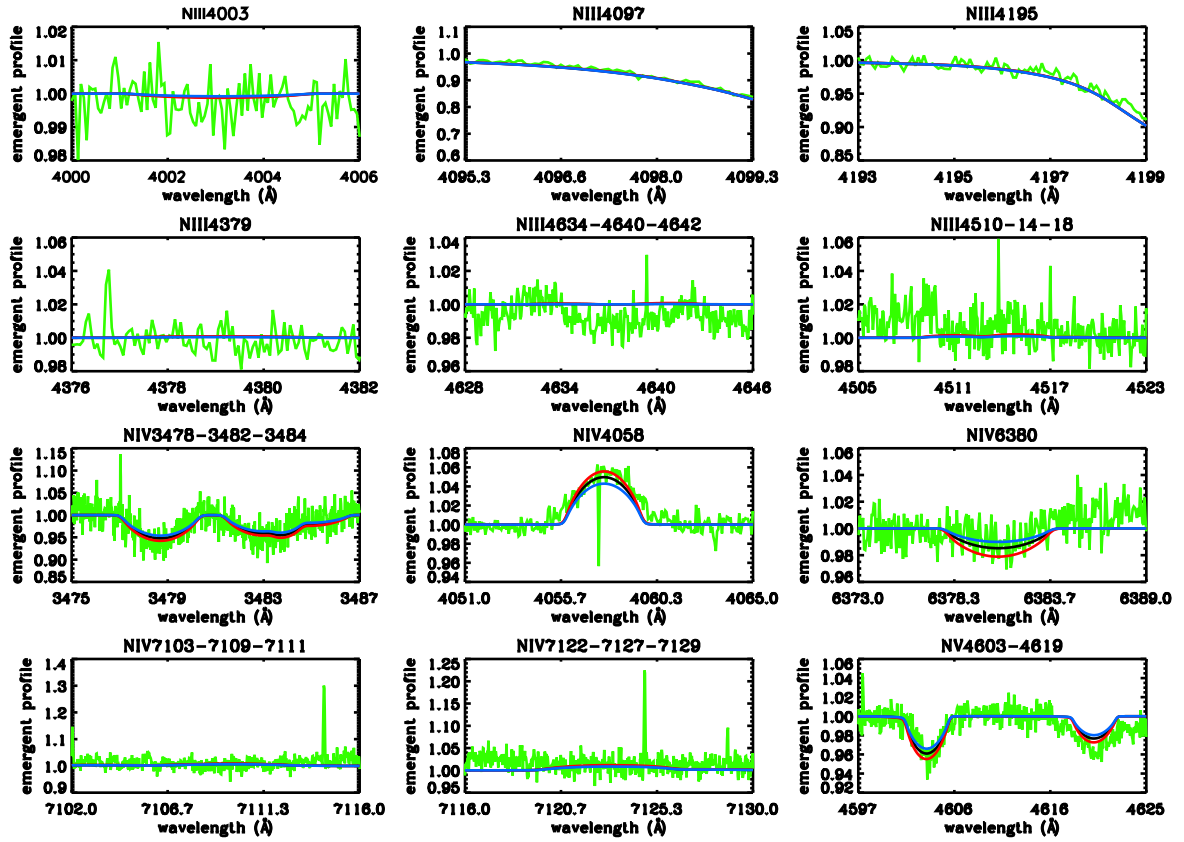


Fig. 7. BI237 - O2 V((f*)).

Thus, the nature of the strong N IV λ 4058 and N V doublet features remains open. Of course, binarity could be a plausible solution, where a cooler component could be responsible for He I and N III, and a hotter one for the intense N IV and N V lines. We note that this is the brightest ($M_V = -5.78$) object of the O-star sample and that other, previously thought single early O-stars, displaying both strong N V lines as well as the presence of He I in their optical spectra such as CygOB2-22 and HD 93129A, were subsequently resolved as binaries (Walborn et al. 2002, Nelan et al. 2004). Thus, the binarity scenario for N11-031 needs to be clarified in future investigations.

Note, however, that the other ON-stars discussed by Walborn et al. 2004, LH64-16 and NGC 346-3, seem to display very similar features, though the presence of He I is not as clearly visible as in our spectrum for N11-031. Similar, but less dramatic, problems are also found for those other sample stars where we were able to analyze N III/N IV/N V in parallel, namely N11-026 and N11-060 (see below). While the presence of such discrepancies in all these objects may point towards a less likely binary scenario for N11-031, we note that the differences in T_{eff} for the two alternative solutions reach 8,000 K in N11-031, and remain at moderate 3,000 K for the other two objects analyzed here.

We will reconsider N11-031 and other ON-stars in future investigations, to clarify the question how it is possible to have weak He I and N III in parallel with strong N IV and N V. For the remainder of this paper, however, we discuss the results for N11-031 in terms of both the cool and the hot solution, without preferring either of them.

N11-038 – O5 II(f⁺). The parameter set derived for this stars is quite similar to Mok07, with only slightly lower $Y_{\text{He}} = 0.08$ and $v \sin i = 100 \text{ km s}^{-1}$. This star displays a peculiar He I λ 4471 profile of triangular shape that could not be reproduced, even if invoking macro-turbulent broadening (as speculated by Mok07).

We obtain $[N] = 7.85 \pm 0.15$, similar to the case of N11-032, by means of quite a good fit to all lines from three ionization stages. Besides the peculiar He I λ 4471 profile, N IV λ 6380 shows contamination by the DIBs at $\lambda\lambda$ 6376.08, 6379.32, and the N V λ 4603 absorption is much stronger than predicted, contrasted to the other component.

Sk-66° 100 – O6 II(f) is one of the field stars within our sample. The inspection of the H/He fits suggests no major revision of the values provided by Mok07.

Figure C.9 shows the best fit to the nitrogen lines. An abundance of $[N] = 8.48 \pm 0.15$ was needed to obtain a consistent fit. This large value agrees well with the large He content found for this object, $Y_{\text{He}} = 0.19$. However, we also found some problems regarding the N IV fits, except for the multiplet around 3480 Å where the fit is perfect. Interestingly, we were able to ‘cure’ these problems by invoking a clumped wind with $f_{\infty} = 0.2$, with no significant changes in the remaining nitrogen lines.

N11-032 – O7 II(f). No major problems were found for this star. Our solution is slightly hotter than in Mok07, and we preferred a typical β value for O-stars, $\beta = 0.80$.

An excellent fit is obtained for this star of the (f) category (Fig. 6), resulting in $[N] = 7.87 \pm 0.15$ for both the N III triplet and the quartet lines. The fit quality of N III λ 4097 is remarkable as well. Note that for this star N III λ 4003 has not been observed.

Since the N IV lines are weak and rather noisy, we can only state that our simulations are consistent with the observations.

N11-045 – O9 III. Our analysis is in good agreement with Mok07. We confirm that a low He abundance (lower than the estimated LMC He baseline abundance) matches the observations.

The only clear N-abundance indicators are the N III quartet lines, since most other lines are weak and the spectrum is noisy (Fig. C.10). N III λ 4097 is also weakly visible, and consistent with the quartet lines. Around this T_{eff} , the N III triplet turns from absorption to emission, and thus this object does not belong to the ‘f’ category. The absence of lines, the fact that the star does not display a fast (projected) rotation, and the very low helium content is consistent with the very low nitrogen abundance, $[N] = 6.98 \pm 0.20$. These findings suggest that this object is of unevolved nature.

5.2.2. Dwarfs

BI253 – O2 V((f^{*})). This was one of the stars that were used by Walborn et al. (2002) to define the O2 spectral type. A slightly hotter solution (by 1 kK, $T_{\text{eff}} = 54.8 \text{ kK}$) than in Mok07 was obtained, by using the N IV/N V ionization equilibrium. This star was also analyzed by Massey et al. (2005) and Doran & Crowther (2011). The former authors provide only a lower limit on T_{eff} and a consistently lower $\log g$ ($T_{\text{eff}} \geq 48 \text{ kK}$ and $\log g = 3.9$), both in agreement with the error bars by Mok07, whilst Doran & Crowther (2011) derive a somewhat cooler solution (by 2 kK) compared to our findings.

Figure C.11 shows that N IV λ 6380, N IV λ 3480, the N IV multiplet around 7120 Å (where we reproduce the observed emission), and the N V lines are nicely fitted, with $[N] = 7.90 \pm 0.15$. At this T_{eff} and \dot{M} , no N III is visible in the spectrum (see also our discussion on N11-031). The feature located around N III λ 4634 corresponds to O IV λ 4632. On the other hand, we were not able to reproduce the rather broad emission of N IV λ 4058 (a larger $v \sin i$ is inconsistent with the remaining lines). For this star, we compared again with a CMFGEN model at similar parameters, in particular with the same $[N]$. Contrasted to our solution, the width of the N IV emission line could be fitted, whilst the other lines indicated either a hotter temperature or a higher abundance.

BI237 – O2 V((f^{*})). As for BI253, the nitrogen ionization equilibrium favours the hotter solution proposed by Mok07 ($T_{\text{eff}} = 53.2 \text{ kK}$) rather than the cooler limit derived by Massey et al. (2005). Our result is also consistent with the work by Doran & Crowther (2011). This object is quite similar to BI253 with a somewhat thinner wind.

Figure 7 displays a good fit for the nitrogen lines. N IV λ 4058 does not show a broad profile as in BI253, and we are able to perform an excellent fit to this line. We derive a lesser enrichment than for BI253, with $[N] = 7.38 \pm 0.15$.

N11-060 – O3 V((f^{*})). With $T_{\text{eff}} = 48 \text{ kK}$, which is about 2 kK hotter than in Mok07, we found a consistent description of H/He and nitrogen. As argued by Mok07, He I λ 4471 is similar to N11-031, and they derived a similar T_{eff} around 45 kK for both stars. Our findings indicate a larger value for both stars, indicating the internal consistency.

Again, we encountered the problem already met for N11-026 and N11-031, i.e., it is rather difficult to fit the lines from three

different nitrogen ionization stages in parallel, see Fig. C.12. We opted for a compromise solution with $[N] = 8.20 \pm 0.30$, which is quite large but in line with the helium enrichment. Note that we also estimate quite a large upper limit, motivated by the following reasoning.

As for N11-026, we considered the impact of a hotter solution. With $T_{\text{eff}} = 51$ kK and $\log g = 4.1$, we are able to fit both N IV and N V at a similar abundance, $[N] = 8.15$. To recover the N III triplet lines at such hot temperatures, however, requires an increase of $[N]$ by roughly 0.3 dex. Thus, we are able to derive a quite similar nitrogen abundance for different T_{eff} , either using the N III/N IV or N IV/N V ionization equilibrium. The upper limit results from the condition to match either N V or N III, respectively.

Sk-70° 69 – O5 V(f). For this field star, we had some problems to reconcile H/He and N at the parameters provided by Mok07. Our final solution is cooler by 1 kK, and we derived $Y_{\text{He}} = 0.14$ which is lower than the $Y_{\text{He}} = 0.17$ estimated by Mok07.

Figure C.13 presents the best fit for all nitrogen lines, for $[N] = 8.05 \pm 0.15$. There are only two disagreements: the ‘right’ wing of N III λ 4634 is predicted a bit too narrow, and N IV λ 4058 is predicted to be in very weak emission, contrasted to the observations. We consider the fit as acceptable, particularly since in a clumped wind this weak emission becomes almost suppressed.

N11-051 – O5 Vn(f). This star is the fastest rotator in our sample, and we derived a slightly higher $v \sin i$ and cooler T_{eff} . As well, we used a prototypical value of $\beta = 0.8$ instead of the rather low $\beta = 0.6$ derived by Mok07, implying also a lower \dot{M} .

Unlike N11-033, where the fast rotation removes almost all information, this object shows the N III triplet in emission, which is quite well reproduced by our model, with $[N] = 7.58 \pm 0.20$ (Fig. C.14). At such high $v \sin i$, these lines are blended with C III λ 4647 – 4650 – 4652. Since carbon is not included in our calculations, it is not possible to predict the right wing of the blended profile. The fact that the carbon triplet has the same strength as the N III one indicates that this star could belong to the newly defined Ofc category (Walborn et al. 2010; Sota et al. 2011), which seems to be strongly peaked at spectral type O5 for all luminosity classes.

The only problem of our fitting procedure is found for N IV λ 4058, predicted to be in slight emission and actually not present in the observed spectra. Contrasted to the case of N11-058 and N11-065, it was not possible to circumvent this discrepancy by lowering \dot{M} , since the fit to H α becomes unacceptable then. By means of a clumped wind with lower \dot{M} , on the other hand, we can fit both H α and obtain a better result for N IV λ 4058, whilst not compromising the remaining nitrogen lines.

N11-058 – O5.5 V(f). To find a consistent solution for all H, He, and N lines, a very low $\dot{M} = 0.01 \cdot 10^{-6} M_{\odot} \text{yr}^{-1}$ is required (similar to the case of N11-065), and also a low $\log g$ (0.14 dex lower than Mok07), which is still consistent with the Balmer line wings but appears to be rather low for a dwarf.

This was the only O-star that could be analyzed by the ‘curve growth method’ with respect to $[N]$ and v_{mic} . The derived value of $v_{\text{mic}} = 6 \pm 3 \text{ km s}^{-1}$ is lower than for the other O-stars, though such a difference does not drastically affect the derived abundance, as argued in Sect.4.4. Quite a large abun-

dance, $[N] = 8.09 \pm 0.15$, was determined which fits all the lines (Fig. C.15).

Sk-66° 18 – O6 V(f). Our estimates agree well with those from Mok07. As for Sk-66° 100, we found a very large nitrogen abundance, $[N] = 8.48 \pm 0.15$ (Fig. C.16). Note that the N IV λ 4058 line is predicted in weak emission but appears in absorption. Again, lowering \dot{M} was not sufficient to cure this problem. A somewhat better fit to the this line was obtained for a weakly clumped wind with $f_{\text{cl}} = 2.3$, included in the figure.

N11-065 – O6.5 V(f). Our best fit to the He lines indicates $Y_{\text{He}} = 0.13$, lower than the value derived by Mok07, $Y_{\text{He}} = 0.17$. As already discussed in Sect. 4.3, a satisfactory reproduction of N IV λ 4058 requires a very low $\dot{M} = 0.05 \cdot 10^{-6} M_{\odot} \text{yr}^{-1}$. Since this line clearly appears in absorption, whereas our model with \dot{M} from Mok07 predicts much too less absorption, we lowered \dot{M} , but were able to preserve the fit to H α and the remaining nitrogen lines. By the inclusion of clumping we obtained an even better fit quality, with $[N] = 8.17 \pm 0.15$ from N III and N IV.

N11-066 – O7 V(f). T_{eff} and $\log g$ as derived by Mok07 turned out to be inconsistent with the N III/N IV ionization equilibrium. We had considerable problems to fit both N III and N IV lines at the same abundance, and particularly to reproduce the absorption within N IV λ 4058 and the N III quartet lines. To this end, a lower T_{eff} was mandatory, but only rough estimates using our coarse grid could be obtained, resulting in $T_{\text{eff}} = 37$ kK and $\log g = 3.7$ dex, which are 2.3 kK and 0.17 dex lower than the values provided by Mok07, respectively. The gravity is somewhat low for a dwarf but still inside the error bars assigned by Mok07. With these values, we determined $[N] = 8.17 \pm 0.20$, see Fig. C.18, which seems rather large for $Y_{\text{He}} = 0.1$.

N11-068 – O7 V(f). As for N11-066, we were only able to fit the H/He and N lines by means of the coarse grid. The differences to the results by Mok07 are significant, but still consistent with the observations and identical to those of N11-066 which has the same spectral type.

In contrast to N11-066, however, particularly the N III triplet shows weaker emission, and thus a lower $[N] = 7.85 \pm 0.20$ has been found, see Fig. C.19.

N11-061 – O9 V. Contrasted to Mok07, we chose a prototypical value for the velocity field exponent, $\beta = 0.8$, together with a larger value for \dot{M} . All H/He lines could be reproduced without difficulties.

The nitrogen analysis is quite similar to the case of N11-045, and we derived $[N] = 7.18 \pm 0.15$ from N III alone (Fig. C.20).

N11-123 – O9.5 V(f). Our parameters are very similar to Mok07, and Fig. C.21 shows our solution for N II/N III. Even though the rotation is not extreme, almost no nitrogen is visible, and the features overlapping with the ‘non-existent’ N II λ 4630 and N III λ 4640 are blends by O III and Si III, respectively. Thus, we infer a very low nitrogen content, $[N] = 7.00 \pm 0.15$, roughly corresponding to the LMC baseline abundance.

N11-087 – O9.5 Vn. Also for this rapid rotator, we found good agreement with Mok07. Due to rotation, all nitrogen lines are

diluted into the continuum (Fig. C.22), and only an upper limit for $[\text{N}]$ could be estimated, $[\text{N}] = 7.38$.

6. Discussion

6.1. Comparison with results from Mok07

In our discussion of the derived results, let us first concentrate on a brief comparison with the findings by Mok07 (see Table 5). Except for few cases, we derive somewhat cooler T_{eff} . To a certain extent, this might be attributed to the improved temperature structure in the new FASTWIND version, and also to the possibility to exploit the nitrogen ionization equilibrium. The largest changes concern N11-026 (4.3 kK cooler), and N11-031 (already the cooler solution is 2.8 kK hotter). For the earliest stars in our sample (two O2 dwarfs and two O2 giants), we determine a temperature range of $47.8 \leq T_{\text{eff}} \leq 54.8$, quite similar to Mok07, but now including N11-031, since we infer hotter solutions for this object. Massey et al. (2005) found a similar range, using two dwarfs and two giants. Gravities changed in parallel for most of the cases, with 0.10 and -0.43 dex as largest positive and negative difference, respectively. Stellar radii show a very good agreement, even for the two stars with the most extreme changes in T_{eff} (less than 5% difference in R_*).

Regarding \dot{M} , we derive values which are typically lower by less than a factor of two ($\Delta \log \dot{M} \approx -0.1 \dots -0.4$ dex), with a maximum change of -1.2 dex for N11-058 based on our analysis of the nitrogen lines. The agreement of the resulting Y_{He} values is good, except for two stars with differences considerably larger than the adopted errors. For both stars (Sk-70° 69 and N11-065), we find a lower helium content.

The largest differences relate to $v \sin i$ and v_{mic} . Differences around 30-40% in $v \sin i$ stress the importance of obtaining this parameter in a separate step, when using an automated fitting method. The substantial differences in v_{mic} , on the other hand, should not be regarded as worrisome though. To a major part, v_{mic} has not been literally derived during this work, but was only adopted (as $v_{\text{mic}} = 10 \text{ km s}^{-1}$), where the resulting fit quality did not indicate any problems with this value, within $\pm 5 \text{ km s}^{-1}$. Only for four mostly cooler stars we were actually able to infer more robust estimates, indicating quite a low $v_{\text{mic}} \approx 5 \text{ km s}^{-1}$. Note, however, that the latter value refers to nitrogen lines only, and inconsistencies in v_{mic} from H/He (used by Mok07) and metal lines have been found already in various studies.

Since the topic of a potential relation between v_{mic} and stellar type ($\log g$) is of recent interest,²⁶ because it might indicate (together with other evidence) the presence of sub-surface convection (Cantiello et al. 2009), a more thorough investigation is certainly required. A derivation from light elements will become difficult for the hotter O-stars though, due to the restricted number of visible lines and the complex formation mechanism of the ubiquitous (photospheric) emission lines. Here, it will become advantageous to exploit the information contained in the numerous UV Fe and Ni lines (e.g., Haser et al. 1998).

6.2. Overlap with B-star nitrogen analyses

To ensure the consistency between O-star nitrogen abundances from this (and upcoming) work and previous results from B-stars

²⁶ e.g., Mok07 found a weak correlation for objects with $\log g \leq 3.6$; see also Kilian et al. (1991), Gies & Lambert (1992), Daflon et al. (2004) for similar results for Galactic B-stars and Hunter et al. (2007) for LMC B-stars.

Table 7. Comparison between nitrogen abundances derived by means of FASTWIND and by Hunter et al. (2009), using their stellar parameters and N II diagnostics alone.

Star	Sp. Type	$[\text{N}]$ t.w.	$[\text{N}]$ Hunter
N11-029	O9.7 Ib	7.20	7.10
N11-036	B0.5 Ib	7.86	7.76
N11-008	B0.7 Ib	7.89	7.84
N11-042	B0 III	6.99	6.92
N11-072	B0.2 III	7.43	7.38

(using different codes, model atoms and analysis methods), a more thorough inspection of the cooler objects is certainly required. Indeed, we are able to compare with alternative nitrogen abundances from some overlapping objects (compiled by Hunter et al. 2009, see Table 6), which base on stellar parameters obtained by means of TLUSTY and using the Si III/Si IV ionization equilibrium (Hunter et al. 2007).

Already in the latter work, Hunter et al. (2007) realized that their T_{eff} -values were somewhat lower than corresponding results from Mok07 (who used exclusively H and He), but also pointed out that T_{eff} estimates based on He II λ 4541 would be in much closer agreement. This is even more true regarding our ‘new’ values, which lie in between the Hunter et al. estimates from Si and those from Mok07. Such differences in T_{eff} derived either from metals or from H/He are somewhat disturbing, due to their influence on the metallic abundances when using lines from one ionization stage only.

Anyhow, Hunter et al. (2007) decided to keep their cooler solution, to preserve the internal consistency of their analysis. Consequently, the nitrogen abundances derived in the present study are systematically larger, due to our higher T_{eff} (leading to intrinsically weaker N II lines), with $\Delta T_{\text{eff}} \approx 1 \text{ kK}$ for N11-008 and N11-072, and $\approx 2 \text{ kK}$ for N11-036. For N11-042, the T_{eff} is rather similar, and for this object the derived $[\text{N}]$ -values indeed overlap by better than 0.1 dex. Also for N11-029, our T_{eff} is rather similar, but we derive a 0.1 dex lower $\log g$, which leads to weaker N II lines.

To check our model atom and our diagnostic approach, we performed an additional analysis by reproducing the conditions adopted by Hunter et al. (2007), i.e., we used their stellar parameters (with negligible \dot{M} to mimic TLUSTY models) and N II lines only, within the ‘curve of growth’ method and adopting their N II equivalent widths and uncertainties. For N11-029 and N11-042, we could only perform a ‘by eye’ estimate because Hunter et al. considered one N II line alone. Corresponding results are compared in Table 7, and the agreement is almost excellent.

Thus, we conclude that the consistency of nitrogen abundances in the overlapping B- and O-star regime is satisfactory, and that the different codes and methods produce a reasonable agreement. However, there is a slight offset on the order of 0.1 to 0.2 dex, which we attribute mostly to different effective temperatures. Since our analysis is based on both N II and N III lines (in contrast to Hunter et al.), and has been performed in parallel with the analysis of H/He, we prefer our values though.

6.3. Nitrogen abundances

Figure 8 summarizes the basic outcome of our analysis, by displaying the derived nitrogen abundances as a function of spectral type and helium content, together with the LMC baseline abundance from Hunter et al. (2007). Evidently, there are only few cooler objects located close to the baseline, whereas the major-

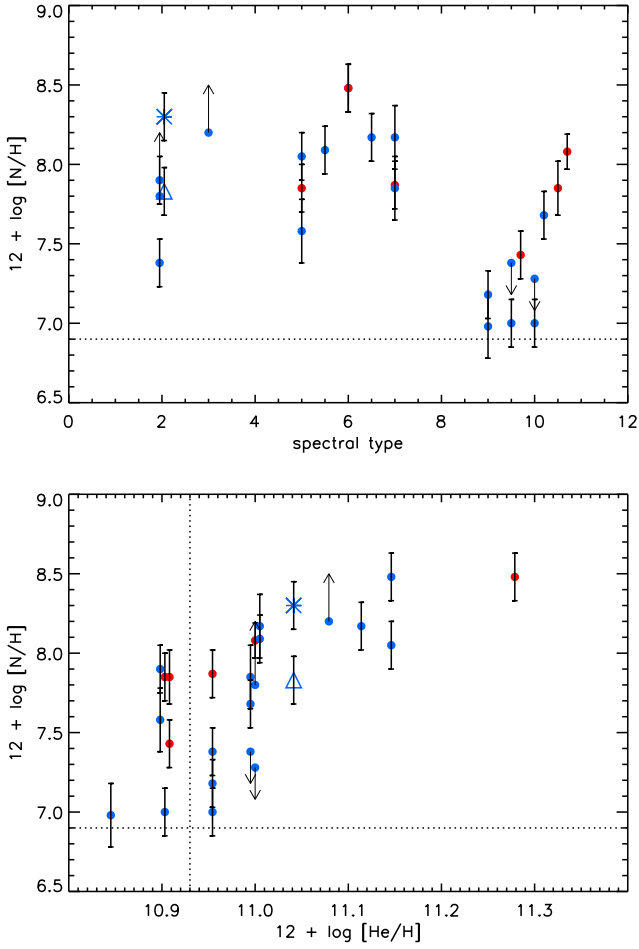


Fig. 8. Nitrogen abundances derived for our LMC sample. Upper panel: As a function of O-star spectral type (‘10-12’ correspond to B0-B2; for T_{eff} , see Table 6). Lower panel: As a function of helium content, $12 + \log(\text{He}/\text{H}) = 12 + \log(Y_{\text{He}})$. Red: luminosity class I-II; blue: III-V. Arrows indicate upper or lower limits. Alternative solutions for N11-031 (see Sect. 5) are indicated by a triangle and an asterisk for the cooler and hotter solution, respectively. The estimated ($1-\sigma$) error for $\log(Y_{\text{He}})$ is 0.05 dex. The dotted lines indicate the LMC nitrogen (Hunter et al. 2007) and the average helium (see text) baseline abundances. Some objects have been slightly shifted horizontally, because of better visibility.

ity of the objects (independent of luminosity class!) is strongly enriched, with $[\text{N}]$ in between 7.5 and 8.1.²⁷ Five objects display extreme enrichment, with $[\text{N}]$ from 8.17 to 8.5, which is close to the maximum nitrogen content given by the CNO equilibrium value for nitrogen, $[\text{N}]_{\text{max}} \approx 8.5$. However, this is well above the enrichment reached for a $40 M_{\odot}$ star with an initial rotational velocity of 275 km s^{-1} (Brott et al. 2011a).

The lower panel of Fig. 8 is more promising though. There seems to be a strong correlation between the nitrogen and the helium enrichment, here displayed logarithmically. The LMC helium abundance should be located, in terms of number fraction, around $Y_{\text{He}} = 0.08\text{--}0.094$ corresponding to $[\text{He}] = 10.90\text{--}10.97$ (Russell & Dopita

²⁷ Note that most stars have ‘normal’ or only moderately enriched helium abundances (see below) so that the high $[\text{N}]$ cannot be an effect of decreasing H content.

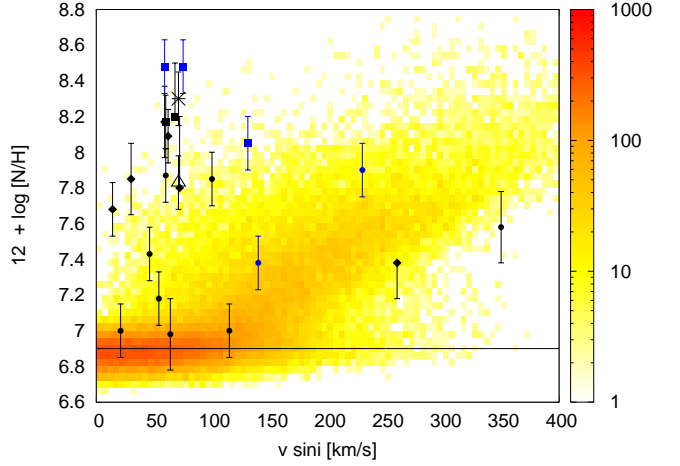


Fig. 9. ‘Hunter-plot’ displaying the nitrogen abundance vs. projected rotational speed. Population synthesis from Brott et al. (2011b), for $T_{\text{eff}} \geq 29 \text{ kK}$ and a magnitude limit $V \leq 15.29$, shown as a density plot in the background. The color coding corresponds to the number of stars per bin, with binsize $5 \text{ km s}^{-1} \times 0.04 \text{ dex}$. Overplotted are data from this study. Black: N11 stars; blue: field stars. Circles, diamonds and squares correspond to objects with low, intermediate and strong helium enrichment, respectively (see text). Alternative solutions for N11-031 (intermediate He enrichment) as in Fig. 8.

1990; Maeder & Meynet 2001; Vermeij & van der Hulst 2002; Peimbert 2003; Tsamis et al. 2003), and agrees quite well with our minimum values for the derived helium abundance. We found only five stars with considerable enriched nitrogen close to this value, three (super-)giants and two dwarfs, but note also the attributed uncertainty in helium content. Except for these objects, the correlation is almost perfect, and there is a certain clustering around the pair $[\text{He}]=11.0/[\text{N}]=8.0$.

A somewhat different view is provided in Fig. 9, which displays the so-called ‘Hunter-plot’, nitrogen-abundance vs. projected rotational speed, for all our sample stars with $T_{\text{eff}} \geq 29 \text{ kK}$. N-11 stars are indicated in black, field stars in blue. Circles, diamonds and squares correspond to objects with low ($Y_{\text{He}} < 0.1$), intermediate ($Y_{\text{He}} = 0.1$), and strong ($Y_{\text{He}} > 0.1$) helium enrichment, respectively.

The background of this figure consists of results from the recent population synthesis by Brott et al. (2011b), for all objects with $T_{\text{eff}} \geq 29 \text{ kK}$, and a magnitude limit (corresponding to our sample) of $V \leq 15.29$, shown as a density plot. The underlying simulation assumes a rather broad Gaussian rotational velocity distribution as derived for LMC early-type stars, peaking at 100 km s^{-1} with a standard deviation of $\sigma = 140 \text{ km s}^{-1}$ (Hunter et al. 2008b, 2009),²⁸ and random inclinations.

Such diagrams ($[\text{N}]$ vs. $v \sin i$, compared with evolutionary calculations) have been presented the first time by Hunter et al. (2008a), to summarize the outcome of the B-star analyses within the FLAMES-I survey, and to investigate the predicted effects of rotational mixing. One of their major findings was the unexpected presence of a significant number of objects with slow rotation and large enrichment, not predicted by (single-star) theory, so-called ‘group 2’ objects.

In the O-star case now, this problem becomes even more severe. We refrain here from a detailed statistical analysis, since

²⁸ Supergiants and stars above $25 M_{\odot}$ have been discarded from their analysis, to avoid effects from mass loss induced spin-down.

the number of investigated objects is too low, and postpone this objective until the results from the FLAMES Tarantula survey (with more than 200 ‘useful’ O-stars) have become available.

Nevertheless, the trend is obvious. Roughly one third of the objects are located at positions where they should be expected (those at the baseline and the ‘diagonal’), another one-third is located at the predicted upper limit, and the last one-third (beyond $[N] = 8.0$) extends to very large values where the predicted population density is almost zero. Let us note that the two objects with the largest $[N]$ enrichment (≈ 8.5 dex, which is (incidentally?) just the maximum nitrogen content given by the CNO equilibrium value) are two field stars, Sk-66° 100 and Sk-66° 18, one O6 giant and another O6 dwarf. Both stars did not present any difficulties in the nitrogen analysis, thus indicating a reasonable quality.

In terms of the original Hunter et al. sample, roughly two-third of our objects would be denoted by ‘group 2’.²⁹ The corresponding number of objects is so large that inclination effects w.r.t. $v \sin i$ should be irrelevant. Interestingly, however, the corresponding He-abundances are in line with our findings. The first group has a low abundance (Fig. 9, circles), the second group mostly consists of enriched objects (diamonds), and the third one comprises objects with considerable He enrichment (squares). Thus, in parallel with the derived correlation between *observed* nitrogen and helium content, the discrepancy between observations and theory becomes the stronger the larger the He-abundance is.

In evolutionary models is the amount of He transported to the surface strongly controlled by the parameter f_{μ} , which describes the inhibiting effect of mean molecular weight gradients (in this case, the H-He gradient) on the transport of elements (see Heger & Langer 2000). The models of Brott et al. (2011a) have adopted $f_{\mu} = 0.1$, from an earlier calibration of Yoon et al. (2006). Lowering the sensitivity to the mean molecular weight barrier would increase mixing of both, nitrogen and helium, to the surface, but also reduce the minimum mass and velocity required for chemical homogeneous evolution in the models (see also the discussion in Heger & Langer 2000). Given the present values of $[N]$ and Y_{He} , it might be possible to derive further constraints on f_{μ} in future work.

7. Summary

In this paper, we investigated the N IV $\lambda 4058$ emission line formation, determined the nitrogen abundance of a sample of 25 LMC O- and early B-stars, and performed a first comparison with corresponding predictions from stellar evolution including rotational mixing. The results of this work can be summarized as follows.

1. In O-stars, the dominating process responsible for the N IV line emission is the strong depopulation of the lower level by the ‘two-electron’ transitions $3p \rightarrow 2p^2$, of (mostly) photospheric origin. This drain increases as a function of \dot{M} , because of increasing ionizing fluxes (which are coupled to the He II continuum), leading to more depopulation of the ground and the coupled $2p^2$ states. Resonance lines (as for the N III emission triplet) do not play a role for typical O-star mass-loss rates and below.

Since in addition to nitrogen there are many other elements which display optical line emission in the hot star regime

(C, O, Si), it might be suspected that similar processes might be invoked, because of similar electronic configurations/transitions.

2. To infer the nitrogen abundances, we re-determined the stellar and wind parameters, by means of ‘by eye’ fits, starting with the values provided by Mok07, but exploiting in parallel the nitrogen ionization equilibrium and deriving $v \sin i$ in a first, separate step. Moreover, we accounted for extra line-broadening expressed in terms of v_{mac} . In addition to systematically lower $v \sin i$, we also derived mostly lower T_{eff} (partly because of using an improved FASTWIND version) and thus $\log g$, but differences to Mok07 are generally small, except for few objects.
3. Based on these parameters, we derived nitrogen abundances, mostly by varying the abundance and comparing with all nitrogen lines present in the spectrum. In a few cases, we were able to estimate $[N]$ and v_{mic} in parallel, by means of a curve-of-growth method.
4. Again in most cases, we found no problems in fitting the nitrogen lines, and reproduced the ‘f’ features quite well. Only for some of the (hotter) objects where lines from all three stages, N III, N IV and N V, are visible, we needed to aim at a compromise solution. Real problems were encountered for one star, N11-031 (ON2 III(f*)), where only either He I, N III and N IV $\lambda 6380$ (at cooler T_{eff}) or N IV and N V (at higher T_{eff}) could be fitted in parallel. The difference in the derived T_{eff} amounts to 8,000 K, which is far from satisfactory, and requires future effort to resolve the problem. A solution in terms of binarity, though somewhat unlikely, cannot be ruled out so far.
5. For some cooler objects already analyzed by Hunter et al. (2007) by means of TLUSTY using N II lines alone, we found differences in $[N]$ on the order of 0.1 to 0.3 dex, with larger values from our analysis. These differences could be exclusively attributed to different stellar parameters, mostly T_{eff} . Overall, however, are the nitrogen abundances in the overlapping B- and O-star domain consistent within a reasonable error.
6. Within our sample, we found only three cooler objects close to the LMC nitrogen baseline abundance, $[N]_{\text{baseline}} = 6.9$. The majority of the analyzed O-stars (independent of luminosity class) seems to be strongly enriched, with $[N] = 7.5$ to 8.1. Five objects indicate an extreme enrichment, with $[N] = 8.17$ to 8.5.
7. There is a rather good correlation between the derived nitrogen and helium surface abundances.
8. Comparing the nitrogen abundances as a function of $v \sin i$ with tailored evolutionary calculations, we found a significant number of highly enriched, low $v \sin i$ (‘group 2’) objects. Interestingly, the correlation between He and N becomes also visible in this comparison: Whilst most objects with unenriched He are located just in the region where the predicted population density is largest (accounting for selection effects), objects with enriched He are located at the upper limit of this distribution and above, and particularly those with the largest He enrichment lie well above this limit.

Due to the low initial (baseline) nitrogen abundance, the detection of strong nitrogen enrichment in the bulk of O-stars might indicate that efficient mixing takes place already during the very early phases of stellar evolution of LMC O-stars. Nevertheless, it would be premature to draw firm conclusions from our results, since the sample size is still low. Upcoming results from the VLT-FLAMES Tarantula survey (which will be derived in

²⁹ In contrast to the B-star ‘group 2’ objects, however, the deviations between predictions and ‘observations’ for some of the objects are much more extreme.

a similar way as presented here, drawing from our experience) will enable a more complete view. In particular, the determination of O-star nitrogen abundances in the LMC will place very tight constraints on the early evolutionary phases of O-stars and thus on the theory of massive star evolution.

Acknowledgements. We like to thank our anonymous referee and N. Walborn for valuable comments and suggestions. Many thanks to P. Crowther for providing us with the UVES spectra for the LMC field stars, and N. Przybilla for synthetic spectra based on his N II model ion and for performing test calculations with the N II data set developed by C. Allende Prieto. Many thanks also to John Hillier for providing the CMFGEN code, and particularly to Keith Butler for his advice and help on the nitrogen atomic data.

J.G.R.G. gratefully acknowledges financial support from the German DFG, under grant 418 SPA 112/1/08 (agreement between the DFG and the Instituto de Astrofísica de Canarias). J.P. and F.N. acknowledge financial support from the Spanish Ministerio de Ciencia e Innovación under projects AYA2008-06166-C03-02 and AYA2010-21697-C05-01.

References

- Aerts, C., Puls, J., Godart, M., & Dupret, M.-A. 2009, *A&A*, 508, 409
- Allen, C. W. 1973, *Astrophysical quantities* (London: University of London, Athlone Press, 1973, 3rd ed.)
- Allende Prieto, C., Lambert, D. L., Hubeny, I., & Lanz, T. 2003, *ApJS*, 147, 363
- Asplund, M., Grevesse, N., & Sauval, A. J. 2005, in *Astronomical Society of the Pacific Conference Series*, Vol. 336, *Cosmic Abundances as Records of Stellar Evolution and Nucleosynthesis*, ed. T. G. Barnes III & F. N. Bash, 25
- Becker, S. R. & Butler, K. 1989, *A&A*, 209, 244
- Brott, I., de Mink, S. E., Cantiello, M., et al. 2011a, *A&A*, 530, A115
- Brott, I., Evans, C. J., Hunter, I., et al. 2011b, *A&A*, 530, A116
- Brunet, J. P., Imbert, M., Martin, N., et al. 1975, *A&AS*, 21, 109
- Butler, K. & Giddings, J. R. 1985, *Newsl. Anal. Astron. Spectra*, 9
- Cantiello, M., Langer, N., Brott, I., et al. 2009, *A&A*, 499, 279
- Cowley, C. R. 1971, *The Observatory*, 91, 139
- Crowther, P. A., Hillier, D. J., Evans, C. J., et al. 2002, *ApJ*, 579, 774
- Cunto, W. & Mendoza, C. 1992, *Revista Mexicana de Astronomía y Astrofísica*, vol. 23, 23, 107
- Daflon, S., Cunha, K., & Butler, K. 2004, *ApJ*, 604, 362
- Doran, E. I. & Crowther, P. A. 2011, *Bulletin de la Societe Royale des Sciences de Liege*, 80, 129
- Dufour, R. J. 1984, in *IAU Symposium*, Vol. 108, *Structure and Evolution of the Magellanic Clouds*, ed. S. van den Bergh & K. S. D. de Boer, 353
- Dufton, P. L., Smartt, S. J., Lee, J. K., et al. 2006, *A&A*, 457, 265
- Eissner, W. 1991, *J. Phys. IV (France)*, 1, C1
- Eissner, W. & Nussbaumer, H. 1969, in *Premiere Reunion de l'Association Europeene de Spectroscopie Atomique No. No. 42 (Paris-Orsay: Faculte des Sciences)*
- Evans, C. J., Crowther, P. A., Fullerton, A. W., & Hillier, D. J. 2004, *ApJ*, 610, 1021
- Evans, C. J., Hunter, I., Smartt, S. J., et al. 2008, *ArXiv e-prints*, 803
- Evans, C. J., Lennon, D. J., Smartt, S. J., & Trundle, C. 2006, *A&A*, 456, 623
- Evans, C. J., Taylor, W. D., Hénault-Brunet, V., et al. 2011, *A&A*, 530, A108
- Gabler, R., Gabler, A., Kudritzki, R. P., Puls, J., & Pauldrach, A. 1989, *A&A*, 226, 162
- Giddings, J. R. 1981, PhD thesis, University of London, (1981)
- Gies, D. R. & Lambert, D. L. 1992, *ApJ*, 387, 673
- Gray, D. F. 1976, *The observation and analysis of stellar photospheres (Research supported by the National Research Council of Canada. New York, Wiley-Interscience, 1976. 484 p.)*
- Grevesse, N. & Sauval, A. J. 1998, *Space Science Reviews*, 85, 161
- Haser, S. M., Pauldrach, A. W. A., Lennon, D. J., et al. 1998, *A&A*, 330, 285
- Heap, S. R., Lanz, T., & Hubeny, I. 2006, *ApJ*, 638, 409
- Heger, A. & Langer, N. 2000, *ApJ*, 544, 1016
- Herbig, G. H. 1975, *ApJ*, 196, 129
- Herrero, A. 2003, in *Astronomical Society of the Pacific Conference Series*, Vol. 304, *Astronomical Society of the Pacific Conference Series*, ed. C. Charbonnel, D. Schaerer, & G. Meynet, 10
- Herrero, A., Kudritzki, R. P., Vilchez, J. M., et al. 1992, *A&A*, 261, 209
- Herrero, A. & Lennon, D. J. 2004, in *IAU Symposium*, Vol. 215, *Stellar Rotation*, ed. A. Maeder & P. Eenens, 209
- Hillier, D. J., Lanz, T., Heap, S. R., et al. 2003, *ApJ*, 588, 1039
- Hillier, D. J. & Miller, D. L. 1999, *ApJ*, 519, 354
- Hubeny, I. 1988, *Computer Physics Communications*, 52, 103
- Hubeny, I. 1998, in *Astronomical Society of the Pacific Conference Series*, Vol. 138, *1997 Pacific Rim Conference on Stellar Astrophysics*, ed. K. L. Chan, K. S. Cheng, & H. P. Singh, 139
- Hubeny, I. & Lanz, T. 1995, *ApJ*, 439, 875
- Hunter, I., Brott, I., Lennon, D. J., et al. 2008a, *ApJ*, 676, L29
- Hunter, I., Dufton, P. L., Smartt, S. J., et al. 2007, *A&A*, 466, 277
- Hunter, I., Lennon, D. J., Dufton, P. L., et al. 2008b, *A&A*, 479, 541
- Hunter, I., Lennon, D. J., Dufton, P. L., et al. 2009, *A&A*, 504, 211
- Kelleher, D. E., Mohr, P. J., Martin, W. C., et al. 1999, in *Society of Photo-Optical Instrumentation Engineers (SPIE) Conference Series*, Vol. 3818, *Society of Photo-Optical Instrumentation Engineers (SPIE) Conference Series*, ed. G. R. Carruthers & K. F. Dymond, 170
- Kilian, J., Becker, S. R., Gehren, T., & Nissen, P. E. 1991, *A&A*, 244, 419
- Krelowski, J., Sneden, C., & Hiltgen, D. 1995, *Planet. Space Sci.*, 43, 1195
- Kudritzki, R.-P. 1980, *A&A*, 85, 174
- Kudritzki, R.-P. & Puls, J. 2000, *ARA&A*, 38, 613
- Lanz, T., Cunha, K., Holtzman, J., & Hubeny, I. 2008, *ApJ*, 678, 1342
- Lanz, T. & Hubeny, I. 2007, *ApJS*, 169, 83
- Lefever, K., Puls, J., & Aerts, C. 2007, *A&A*, 463, 1093
- Maeder, A. & Meynet, G. 2001, *A&A*, 373, 555
- Markova, N. & Puls, J. 2008, *A&A*, 478, 823
- Markova, N., Puls, J., Repolust, T., & Markov, H. 2004, *A&A*, 413, 693
- Massa, D., Fullerton, A. W., Sonneborn, G., & Hutchings, J. B. 2003, *ApJ*, 586, 996
- Massey, P., Bresolin, F., Kudritzki, R. P., Puls, J., & Pauldrach, A. W. A. 2004, *ApJ*, 608, 1001
- Massey, P., Lang, C. C., Degioia-Eastwood, K., & Garmany, C. D. 1995, *ApJ*, 438, 188
- Massey, P., Puls, J., Pauldrach, A. W. A., et al. 2005, *ApJ*, 627, 477
- Meynet, G. & Maeder, A. 2000, *A&A*, 361, 101
- Mihalas, D. & Hummer, D. G. 1973, *ApJ*, 179, 827
- Mokiem, M. R., de Koter, A., Evans, C. J., et al. 2007a, *A&A*, 465, 1003
- Mokiem, M. R., de Koter, A., Puls, J., et al. 2005, *A&A*, 441, 711
- Mokiem, M. R., de Koter, A., Vink, J. S., et al. 2007b, *A&A*, 473, 603
- Moore, C. E. 1971, *Selected tables of atomic spectra - A: Atomic energy levels - Second edition - B: Multiplet tables; N IV, N V, N VI, N VII. Data derived from the analyses of optical spectra (NSRDS-NBS (National Standard Reference Series - National Bureau of Standards, Washington, DC: U.S. Department of Commerce, National Bureau of Standards, 1971))*
- Moore, C. E. 1975, *Selected tables of atomic spectra - A: Atomic energy levels - Second edition - B: Multiplet table; N I, N II, N III. Data derived from the analyses of optical spectra (NSRDS-NBS (National Standard Reference Series - National Bureau of Standards, Washington, DC: U.S. Department of Commerce, National Bureau of Standards, 1975))*
- Morel, T. 2009, *Communications in Asteroseismology*, 158, 122
- Najarro, F., Hillier, D. J., Puls, J., Lanz, T., & Martins, F. 2006, *A&A*, 456, 659
- Negueruela, I. & Clark, J. S. 2005, *A&A*, 436, 541
- Nelan, E. P., Walborn, N. R., Wallace, D. J., et al. 2004, *AJ*, 128, 323
- Parker, J. W., Garmany, C. D., Massey, P., & Walborn, N. R. 1992, *AJ*, 103, 1205
- Pauldrach, A. W. A., Kudritzki, R. P., Puls, J., Butler, K., & Hunsinger, J. 1994, *A&A*, 283, 525
- Peimbert, A. 2003, *ApJ*, 584, 735
- Przybilla, N. & Butler, K. 2001, *A&A*, 379, 955
- Przybilla, N., Nieva, M., & Butler, K. 2008, *ApJ*, 688, L103
- Puls, J. 2008, in *IAU Symposium*, Vol. 250, *Massive Stars as Cosmic Engines*, ed. F. Bresolin, P. A. Crowther, & J. Puls
- Puls, J., Kudritzki, R.-P., Herrero, A., et al. 1996, *A&A*, 305, 171
- Puls, J., Markova, N., Scuderi, S., et al. 2006, *A&A*, 454, 625
- Puls, J., Urbaneja, M. A., Venero, R., et al. 2005, *A&A*, 435, 669
- Ramsbottom, C. A., Berrington, K. A., Hibbert, A., & Bell, K. L. 1994, *Phys. Scr.*, 50, 246
- Repolust, T., Puls, J., & Herrero, A. 2004, *A&A*, 415, 349
- Rivero Gonzalez, J. G., Puls, J., & Najarro, F. 2011, *ArXiv e-prints*, [arXiv:1109.3595]
- Russell, S. C. & Dopita, M. A. 1990, *ApJS*, 74, 93
- Sanduleak, N. 1970, *Contributions from the Cerro Tololo Inter-American Observatory*, 89
- Santolaya-Rey, A. E., Puls, J., & Herrero, A. 1997, *A&A*, 323, 488
- Seaton, M. J. 1958, *MNRAS*, 118, 504
- Seaton, M. J. 1962, in *Atomic and Molecular Processes*, ed. D. R. Bates (New York, Academic Press), 375
- Simón-Díaz, S. & Herrero, A. 2007, *A&A*, 468, 1063
- Simón-Díaz, S., Herrero, A., Esteban, C., & Najarro, F. 2006, *A&A*, 448, 351
- Simón-Díaz, S. & Stasińska, G. 2008, *MNRAS*, 389, 1009
- Simón-Díaz, S., Uytterhoeven, K., Herrero, A., Castro, N., & Puls, J. 2010, *Astronomische Nachrichten*, 331, 1069
- Sota, A., Maíz Apellániz, J., Walborn, N. R., et al. 2011, *ApJS*, 193, 24
- Sundqvist, J. O., Puls, J., Feldmeier, A., & Owocki, S. P. 2011, *A&A*, 528, A64
- Taresch, G., Kudritzki, R. P., Hurwitz, M., et al. 1997, *A&A*, 321, 531
- Trundle, C., Dufton, P. L., Hunter, I., et al. 2007, *A&A*, 471, 625

- Tsamis, Y. G., Barlow, M. J., Liu, X.-W., Danziger, I. J., & Storey, P. J. 2003, MNRAS, 338, 687
- Tully, J. A., Seaton, M. J., & Berrington, K. A. 1990, Journal of Physics B Atomic Molecular Physics, 23, 3811
- Urbaneja, M. 2004, PhD thesis, Universidad de la Laguna, La Laguna, Spain
- van Regemorter, H. 1962, ApJ, 136, 906
- Vermeij, R. & van der Hulst, J. M. 2002, A&A, 391, 1081
- Vink, J. S., Brott, I., Gräfener, G., et al. 2010, A&A, 512, L7
- Walborn, N. R. 1971a, ApJ, 167, L31
- Walborn, N. R. 1971b, ApJS, 23, 257
- Walborn, N. R., Howarth, I. D., Lennon, D. J., et al. 2002, AJ, 123, 2754
- Walborn, N. R., Lennon, D. J., Haser, S. M., Kudritzki, R.-P., & Voels, S. A. 1995, PASP, 107, 104
- Walborn, N. R., Morrell, N. I., Howarth, I. D., et al. 2004, ApJ, 608, 1028
- Walborn, N. R., Sota, A., Maíz Apellániz, J., et al. 2010, ApJ, 711, L143
- Yoon, S.-C., Langer, N., & Norman, C. 2006, A&A, 460, 199

Appendix A: Details of the nitrogen model atom

This section provides some details of our N II, N IV and N V model ions (corresponding material for N III has been already presented in Paper I). Configurations and term designations are outlined in Tables A.1, A.2 and A.3, whilst Figs. A.1, A.2 and A.3 display the Grotrian diagrams for the N II singlet and triplet system (the quintet system comprises five levels only), the N IV singlet and triplet system, and the N V doublet system, respectively. In these figures, important optical transitions as given in Table 2 are indicated as well.

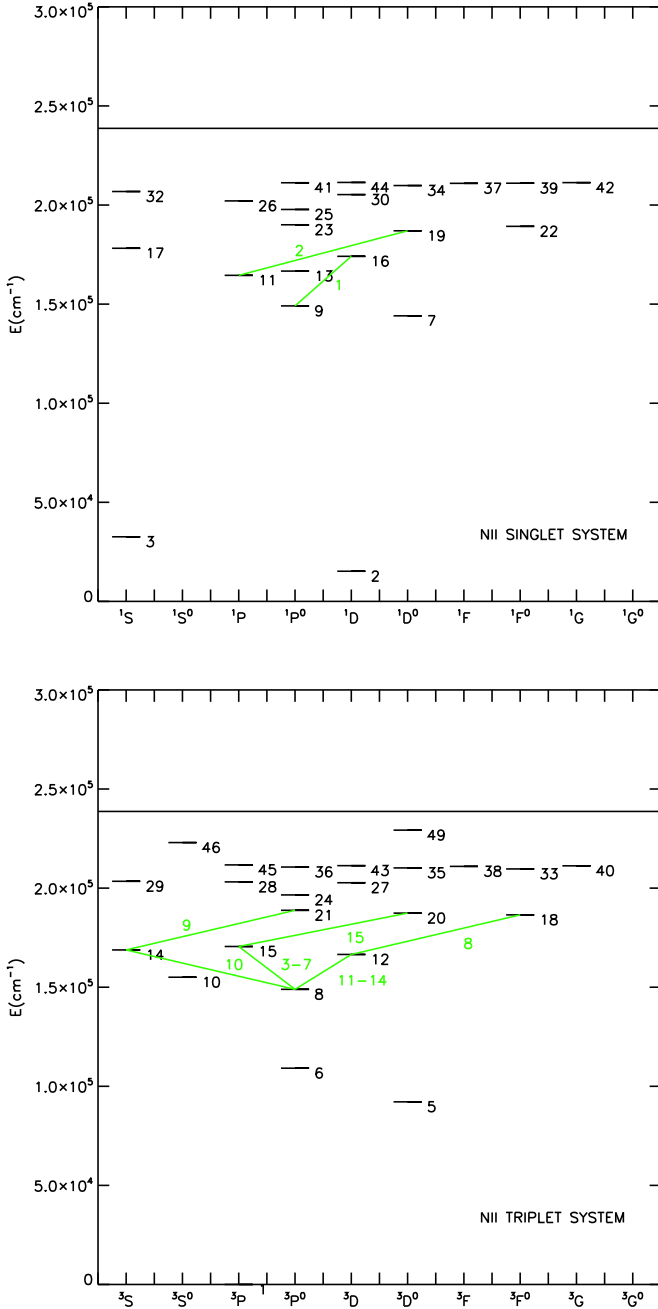


Fig. A.1. Grotrian diagrams for the N II singlet (upper panel) and triplet (lower panel) systems. Level designations refer to Table A.1. Important optical transitions are indicated by green lines and numbers referring to entries in Table 2.

Table A.1. Electronic configurations and term designations of our N II model ion. The level numbers correspond to the entries in the Grotrian diagrams in Fig. A.1, for the singlet and the triplet terms.

#	Configuration	Desig.	#	Configuration	Desig.
1	1s ² 2s ² 2p ²	2p ² ³ P	26	1s ² 2s ² 2p(2P ⁰) 4p	4p ¹ P
2	1s ² 2s ² 2p ²	2p ² ¹ D	27	1s ² 2s ² 2p(2P ⁰) 4p	4p ³ D
3	1s ² 2s ² 2p ²	2p ² ¹ S	28	1s ² 2s ² 2p(2P ⁰) 4p	4p ³ P
4	1s ² 2s 2p ³	2p ³ ⁵ S ⁰	29	1s ² 2s ² 2p(2P ⁰) 4p	4p ³ S
5	1s ² 2s 2p ³	2p ³ ³ D ⁰	30	1s ² 2s ² 2p(2P ⁰) 4p	4p ¹ D
6	1s ² 2s 2p ³	2p ³ ³ P ⁰	31	1s ² 2s 2p ² (⁴ P) 3s	3s' ⁵ S
7	1s ² 2s 2p ³	2p ³ ¹ D ⁰	32	1s ² 2s ² 2p(2P ⁰) 4p	4p ¹ S
8	1s ² 2s ² 2p(2P ⁰) 3s	3s ³ P ⁰	33	1s ² 2s ² 2p(2P ⁰) 4d	4d ³ F ⁰
9	1s ² 2s ² 2p(2P ⁰) 3s	3s ¹ P ⁰	34	1s ² 2s ² 2p(2P ⁰) 4d	4d ¹ D ⁰
10	1s ² 2s 2p ³	2p ³ ³ S ⁰	35	1s ² 2s ² 2p(2P ⁰) 4d	4d ³ D ⁰
11	1s ² 2s ² 2p(2P ⁰) 3p	3p ¹ P	36	1s ² 2s ² 2p(2P ⁰) 4d	4d ³ P ⁰
12	1s ² 2s ² 2p(2P ⁰) 3p	3p ³ D	37	1s ² 2s ² 2p(2P ⁰) 4f	4f ¹ F
13	1s ² 2s 2p ³	2p ³ ¹ P ⁰	38	1s ² 2s ² 2p(2P ⁰) 4f	4f ³ F
14	1s ² 2s ² 2p(2P ⁰) 3p	3p ³ S	39	1s ² 2s ² 2p(2P ⁰) 4d	4d ¹ F ⁰
15	1s ² 2s ² 2p(2P ⁰) 3p	3p ³ P	40	1s ² 2s ² 2p(2P ⁰) 4f	4f' ³ G
16	1s ² 2s ² 2p(2P ⁰) 3p	3p ¹ D	41	1s ² 2s ² 2p(2P ⁰) 4d	4d ¹ P ⁰
17	1s ² 2s ² 2p(2P ⁰) 3p	3p ¹ S	42	1s ² 2s ² 2p(2P ⁰) 4f	4f' ¹ G
18	1s ² 2s ² 2p(2P ⁰) 3d	3d ³ F ⁰	43	1s ² 2s ² 2p(2P ⁰) 4f	4f' ³ D
19	1s ² 2s ² 2p(2P ⁰) 3d	3d ¹ D ⁰	44	1s ² 2s ² 2p(2P ⁰) 4f	4f' ¹ D
20	1s ² 2s ² 2p(2P ⁰) 3d	3d ³ D ⁰	45	1s ² 2s 2p ² (⁴ P) 3s	3s' ³ P
21	1s ² 2s ² 2p(2P ⁰) 3d	3d ³ P ⁰	46	1s ² 2s 2p ² (⁴ P) 3p	3p' ³ S ⁰
22	1s ² 2s ² 2p(2P ⁰) 3d	3d ¹ F ⁰	47	1s ² 2s 2p ² (⁴ P) 3p	3p' ⁵ D ⁰
23	1s ² 2s ² 2p(2P ⁰) 3d	3d ¹ P ⁰	48	1s ² 2s 2p ² (⁴ P) 3p	3p' ⁵ P ⁰
24	1s ² 2s ² 2p(2P ⁰) 4s	4s ³ P ⁰	49	1s ² 2s 2p ² (⁴ P) 3p	3p' ³ D ⁰
25	1s ² 2s ² 2p(2P ⁰) 4s	4s ¹ P ⁰	50	1s ² 2s 2p ² (⁴ P) 3p	3p' ⁵ S ⁰

Table A.2. Electronic configurations and term designations of our N IV model ion. The level numbers correspond to the entries in the Grotrian diagrams in Fig. A.2.

#	Configuration	Desig.	#	Configuration	Desig.
1	1s ² 2s ²	2s ² ¹ S	26	1s ² 2p(2P ⁰ _{3/2}) 3d	3d' ¹ F ⁰
2	1s ² 2s 2p	2p ³ P ⁰	27	1s ² 2s 4p	4p ¹ P ⁰
3	1s ² 2s 2p	2p ¹ P ⁰	28	1s ² 2s 4d	4d ³ D
4	1s ² 2s 2p	2p ³ P	29	1s ² 2p(2P ⁰ _{3/2}) 3d	3d' ³ P ⁰
5	1s ² 2p ²	2p ² ¹ D	30	1s ² 2s 4d	4d ¹ D
6	1s ² 2p ²	2p ² ¹ S	31	1s ² 2p(2P ⁰ _{3/2}) 3p	3p' ¹ S
7	1s ² 2s 3s	3s ³ S	32	1s ² 2s 4f	4f ³ F ⁰
8	1s ² 2s 3s	3s ¹ S	33	1s ² 2p(2P ⁰ _{3/2}) 3d	3d' ¹ P ⁰
9	1s ² 2s 3p	3p ¹ P ⁰	34	1s ² 2s 4f	4f ¹ F ⁰
10	1s ² 2s 3p	3p ³ P ⁰	35	1s ² 2s 5s	5s ³ S
11	1s ² 2s 3d	3d ³ D	36	1s ² 2s 5s	5s ¹ S
12	1s ² 2s 3d	3d ¹ D	37	1s ² 2s 5p	5p ³ P ⁰
13	1s ² 2p(2P ⁰) 3s	3s' ³ P ⁰	38	1s ² 2s 5p	5p ¹ P ⁰
14	1s ² 2p(2P ⁰ _{3/2}) 3s	3s' ¹ P ⁰	39	1s ² 2s 5d	5d ³ D
15	1s ² 2p(2P ⁰ _{1/2}) 3p	3p' ¹ P	40	1s ² 2s 5d	5d ¹ D
16	1s ² 2p(2P ⁰) 3p	3p' ³ D	41	1s ² 2s 5g	5g ¹ G
17	1s ² 2p(2P ⁰ _{3/2}) 3d	3d' ³ S	42	1s ² 2s 5g	5g ³ G
18	1s ² 2p(2P ⁰ _{1/2}) 3d	3d' ¹ D ⁰	43	1s ² 2s 5f	5f ³ F ⁰
19	1s ² 2s 4s	4s ¹ S	44	1s ² 2s 5f	5f ¹ F ⁰
20	1s ² 2p(2P ⁰) 3p	3p' ³ P	45	1s ² 2s 6s	6s ³ S
21	1s ² 2p(2P ⁰) 3d	3d' ³ F ⁰	46	1s ² 2s 6s	6s ¹ S
22	1s ² 2p(2P ⁰ _{3/2}) 3p	3p' ¹ D	47	1s ² 2s 6p	6p ³ P ⁰
23	1s ² 2s 4p	4p ³ P ⁰	48	1s ² 2s 6p	6p ¹ P ⁰
24	1s ² 2s 4s	4s ³ S	49	1s ² 2s 6d	6d ³ D
25	1s ² 2p(2P ⁰) 3d	3d' ³ D ⁰	50	1s ² 2s 6g	6g ³ G

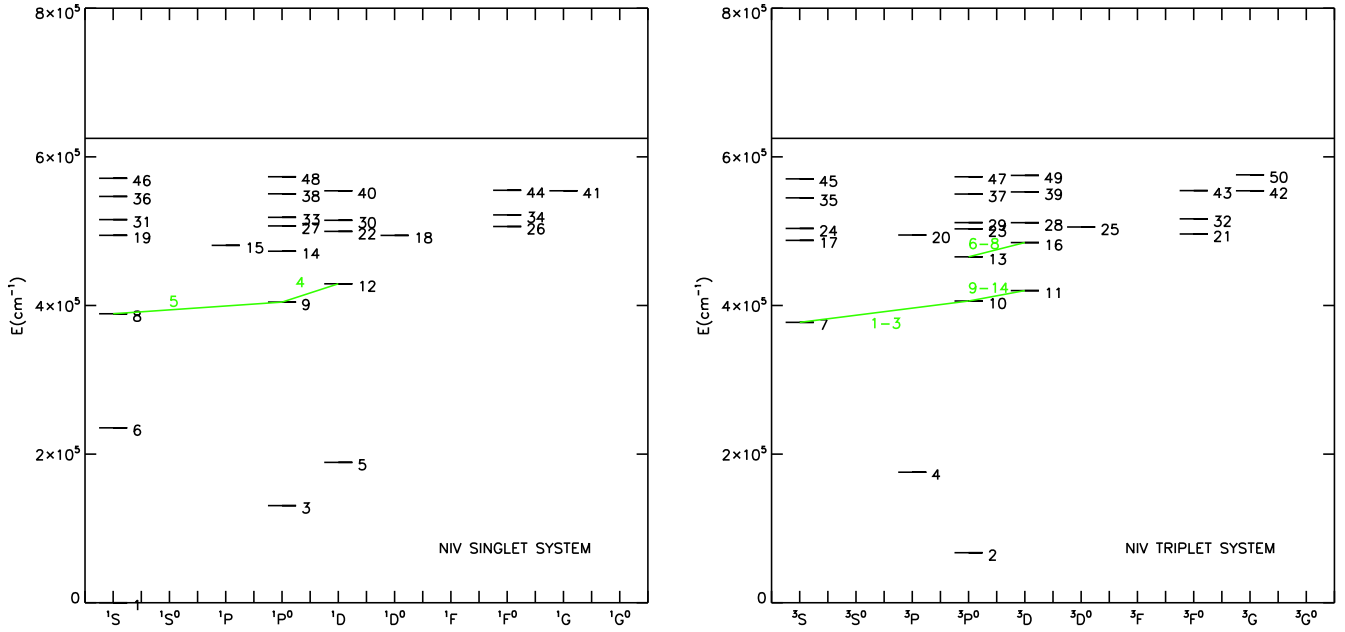


Fig. A.2. As Fig. A.1, but for the N IV singlet (left) and triplet (right) system. Level numbers refer to Table A.2.

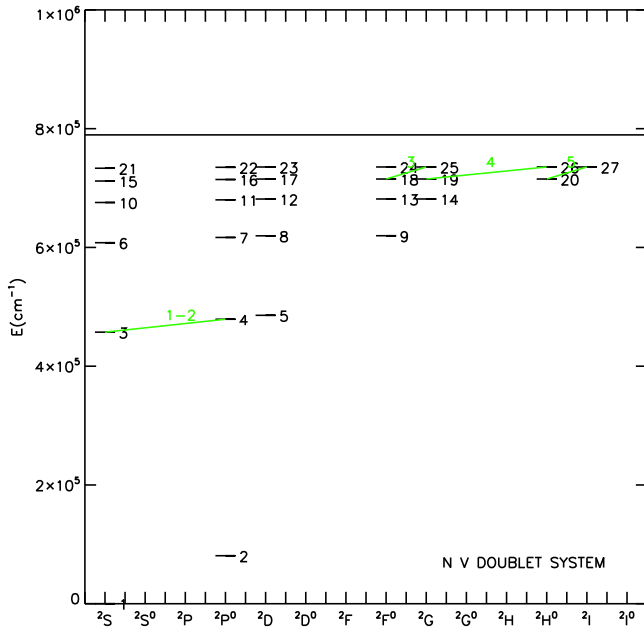


Fig. A.3. As Fig. A.1, but for the N V model ion. Level numbers refer to Table A.3.

Appendix B: Tests of the N II model ion

Figures B.1 to B.7 refer to tests of our N II model ion, as described in Sect. 2.2.1. Figure B.1 compares electron temperatures and densities for B-star parameters calculated by FASTWIND and TLUSTY, whilst Figs. B.2 to B.7 compare corresponding synthetic N II line profiles from these two codes and from calculations by Przybilla et al. (priv. comm.).

Table A.3. Electronic configurations and term designations of our N V model ion. The level numbers correspond to the entries in the Grotrian diagram Fig. A.3.

#	Configuration	Desig.	#	Configuration	Desig.
1	1s ² 2s	2s ² S	15	1s ² 6s	6s ² S
2	1s ² 2p	2p ² P ⁰	16	1s ² 6p	6p ² P ⁰
3	1s ² 3s	3s ² S	17	1s ² 6d	6d ² D
4	1s ² 3p	3p ² P ⁰	18	1s ² 6f	6f ² F ⁰
5	1s ² 3d	3d ² D	19	1s ² 6g	6g ² G
6	1s ² 4s	4s ² S	20	1s ² 6h	6h ² H ⁰
7	1s ² 4p	4p ² P ⁰	21	1s ² 7s	7s ² S
8	1s ² 4d	4d ² D	22	1s ² 7p	7p ² P ⁰
9	1s ² 4f	4f ² F ⁰	23	1s ² 7d	7d ² D
10	1s ² 5s	5s ² S	24	1s ² 7f	7f ² F ⁰
11	1s ² 5p	5p ² P ⁰	25	1s ² 7g	7g ² G
12	1s ² 5d	5d ² D	26	1s ² 7h	7h ² H ⁰
13	1s ² 5f	5f ² F ⁰	27	1s ² 7i	7i ² I
14	1s ² 5g	5g ² G			

Appendix C: Line fits for individual objects

Figures C.1 to C.22 display the observed (green) and best-fitting optical nitrogen spectra (black) for all our objects, except for N11-072, N11-032, and B1237 which are contained in the main section. Blue and red spectra show corresponding synthetic line profiles with [N] at the lower and upper limit, respectively. For N11-031 (Fig. C.7), we show the fits corresponding to the two alternative solutions for this star (see Sect. 5). For details on the line fits, see Sect. 5, and for adopted stellar parameters and derived nitrogen abundances inspect Table 4 and Table 6, respectively. All fits are based on unclumped winds except explicitly stated.

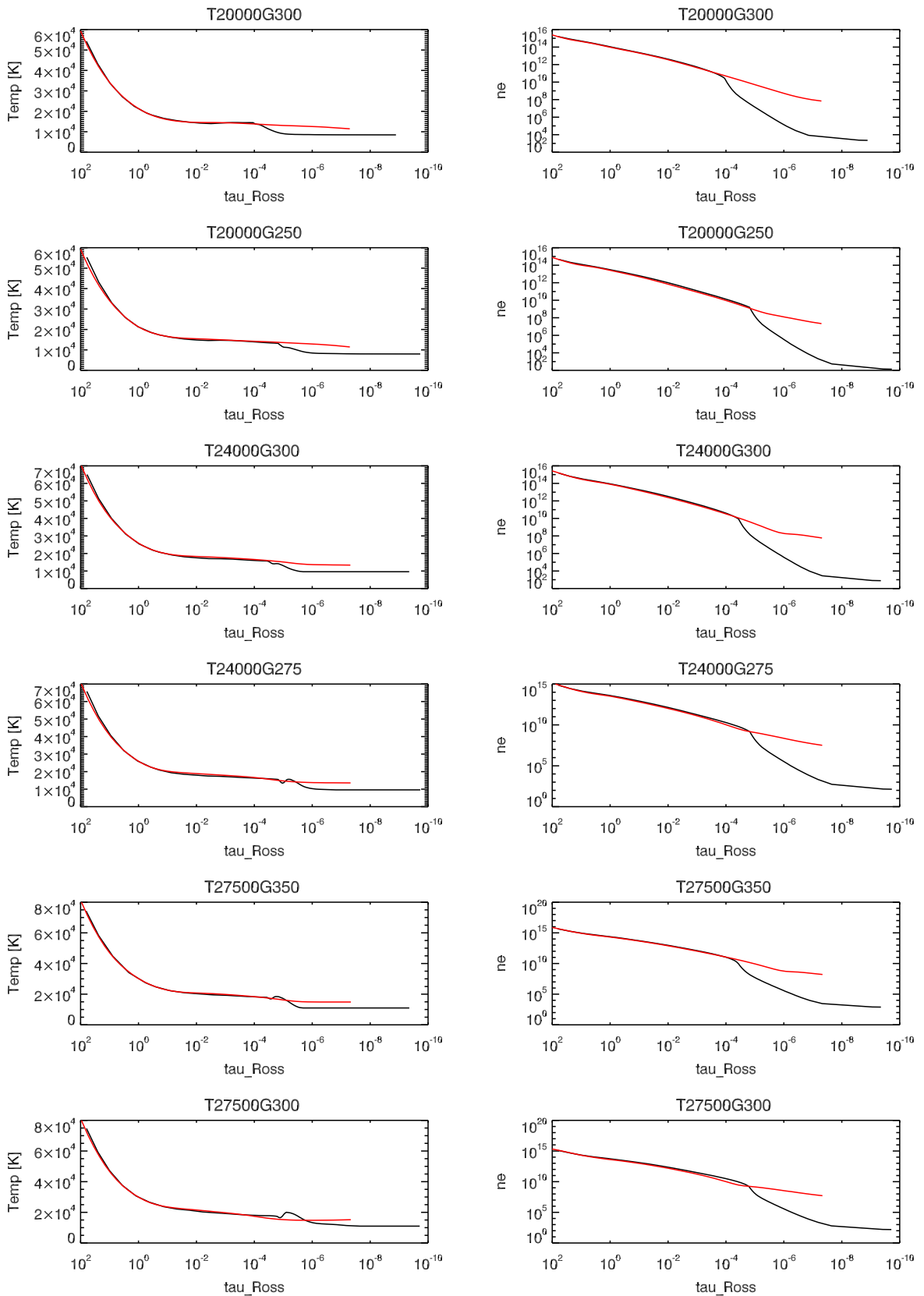


Fig. B.1. FASTWIND (black) vs. TLUSTY (red): comparison of electron temperature and electron density as a function of Rosseland optical depth, for the six models corresponding to Figs. B.2 to B.7.

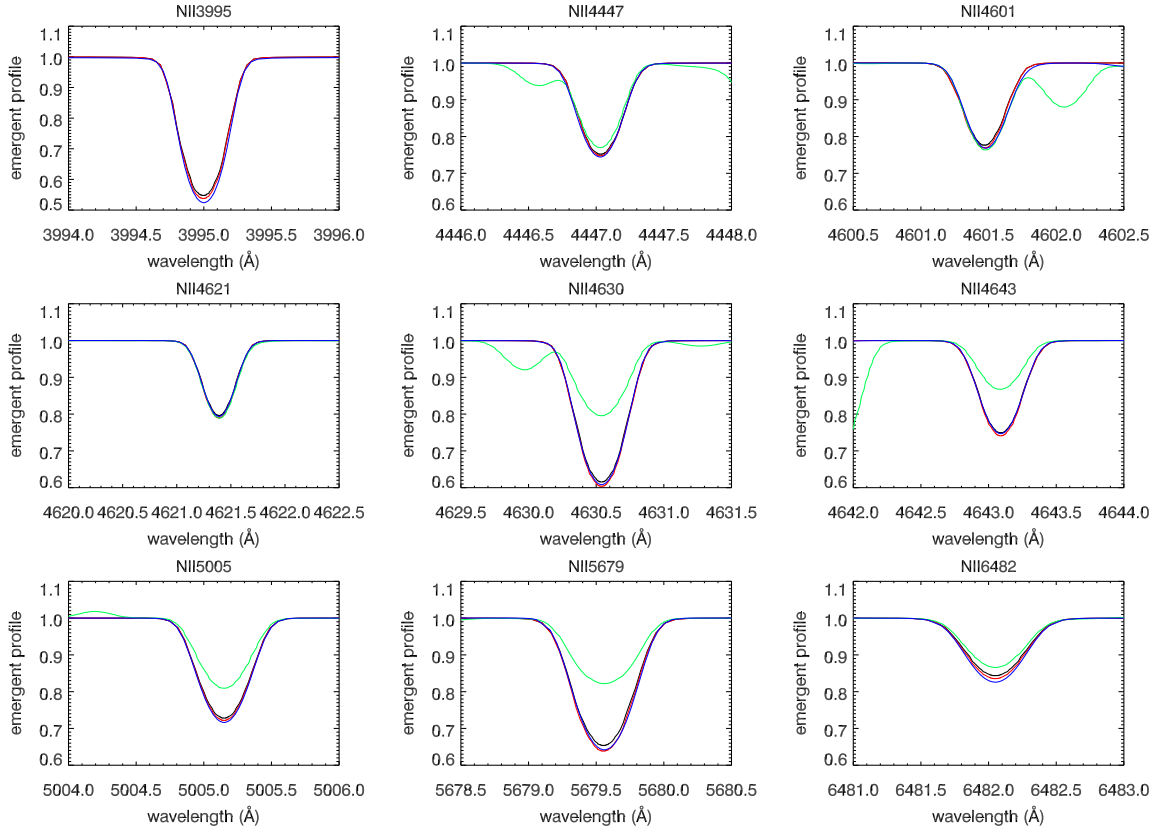


Fig. B.2. Comparison of important optical N II line profiles for a model with $T_{\text{eff}} = 20$ kK and $\log g = 3.0$, for models – see Table 1 – FW (black), FW2 (red), TL (green) and Prz (blue). Note that N II λ 3995 is not present in the BSTAR2006 grid.

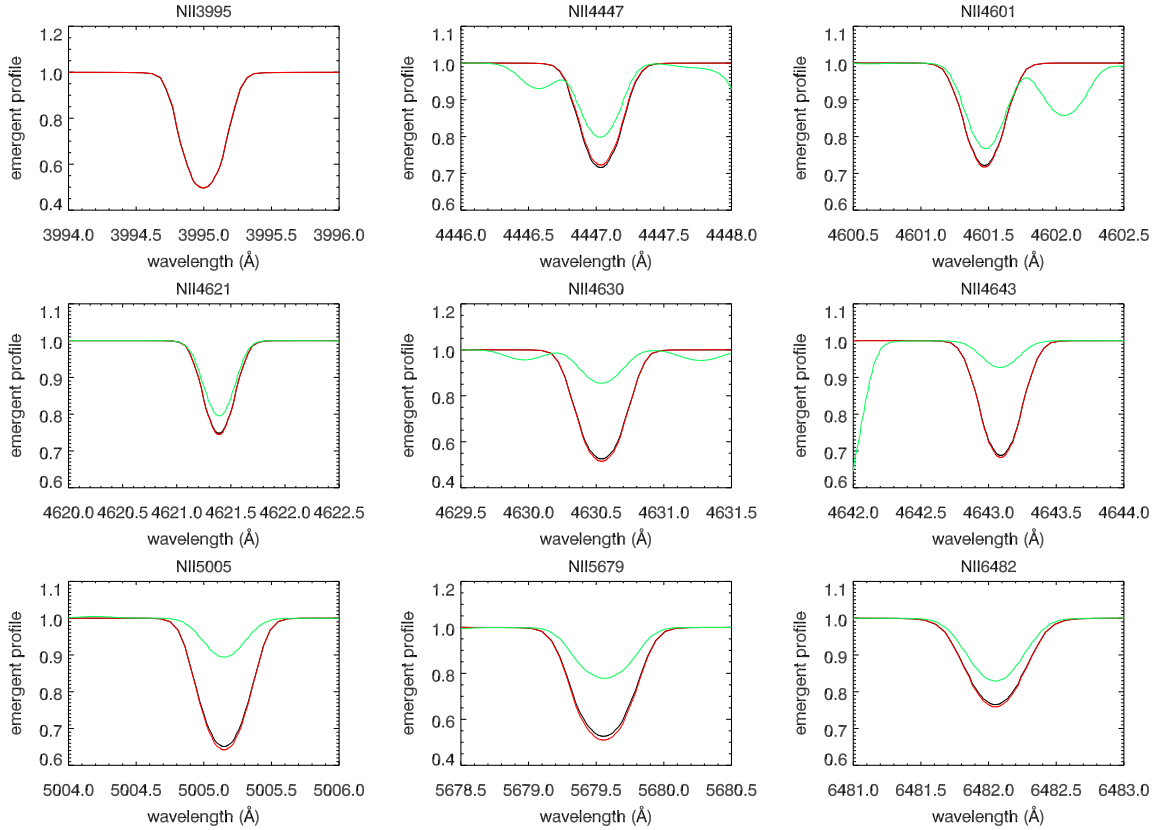


Fig. B.3. As Fig. B.2, but for $T_{\text{eff}} = 20$ kK and $\log g = 2.5$, for models FW (black), FW2 (red), and TL (green).

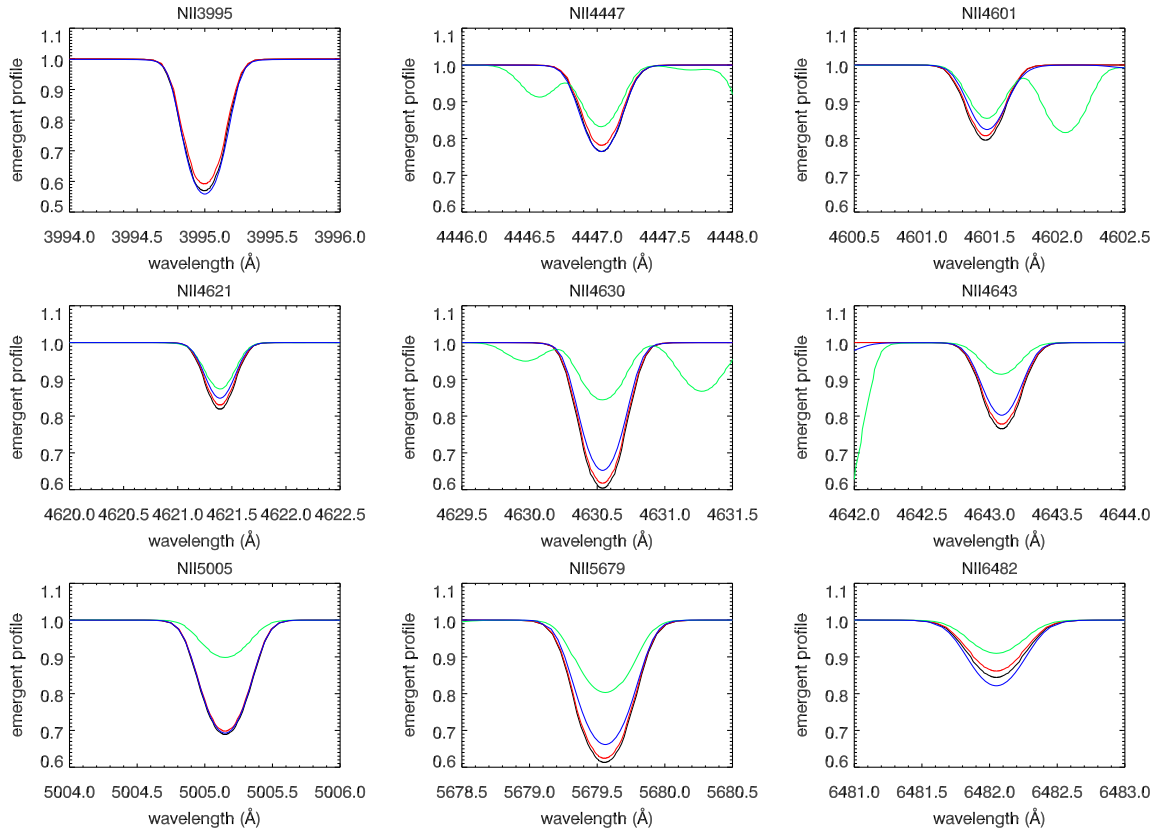


Fig. B.4. As Fig. B.2, but for $T_{\text{eff}} = 24$ kK and $\log g = 3.0$.

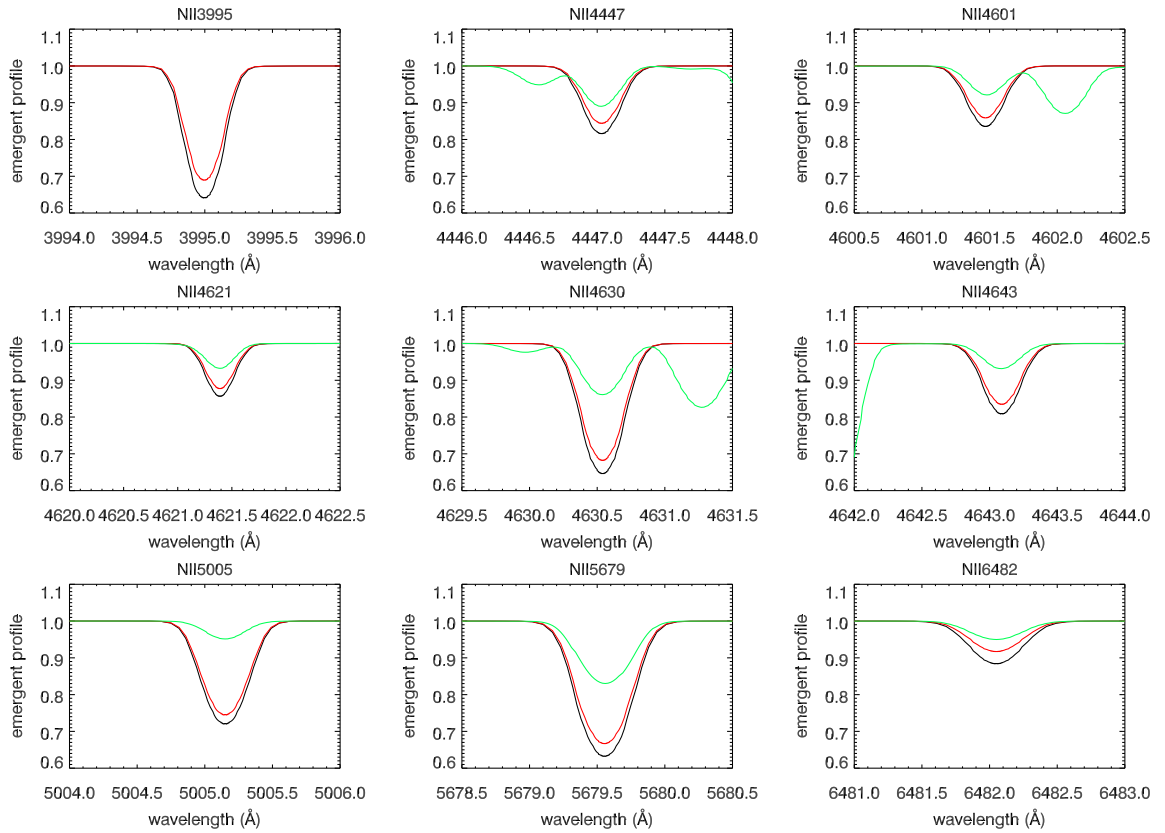


Fig. B.5. As Fig. B.3, but for $T_{\text{eff}} = 24$ kK and $\log g = 2.75$.

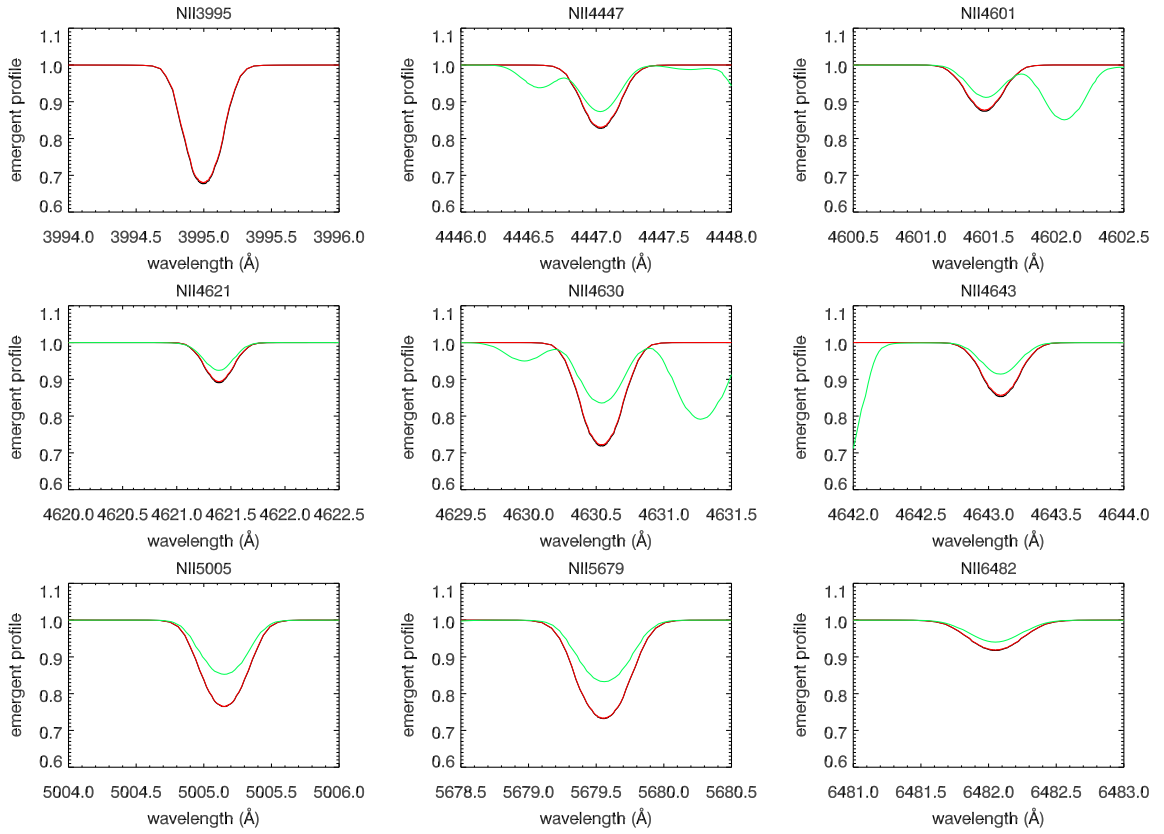


Fig. B.6. As Fig. B.3, but for $T_{\text{eff}} = 27.5$ kK and $\log g = 3.5$.

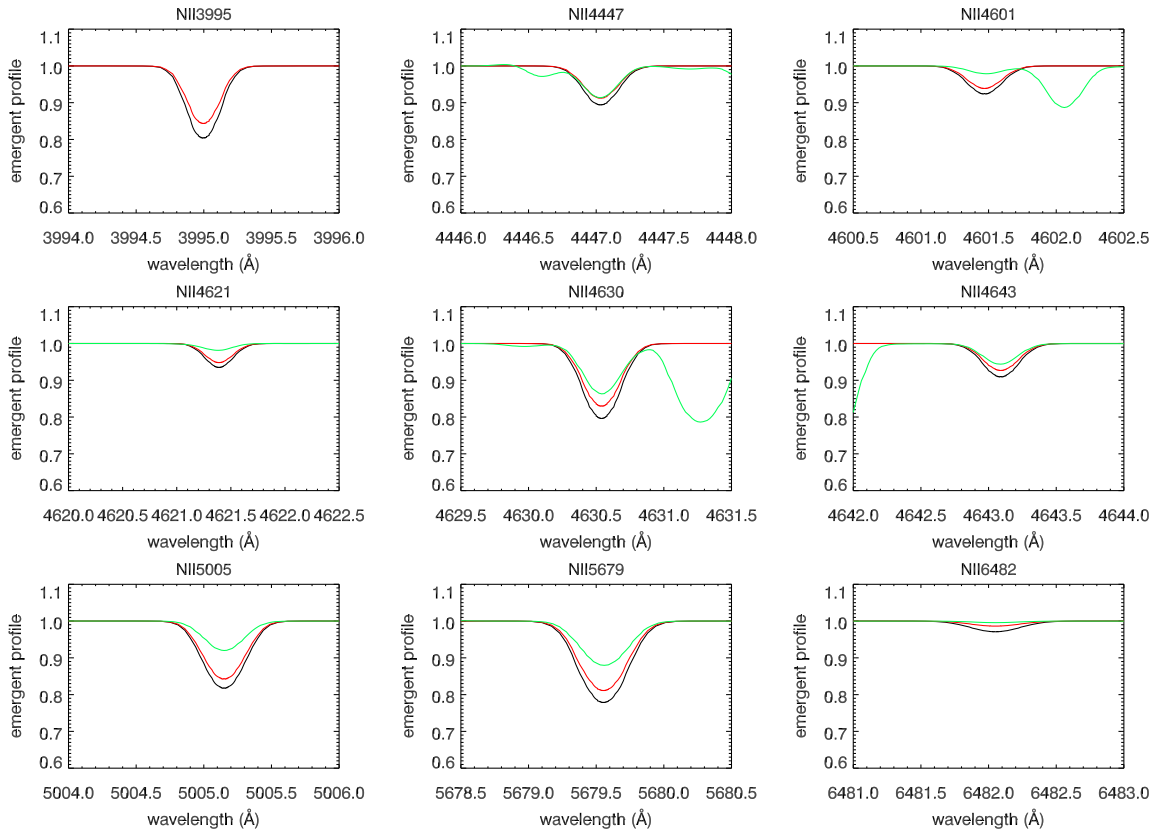


Fig. B.7. As Fig. B.3, but for $T_{\text{eff}} = 27.5$ kK and $\log g = 3.0$.

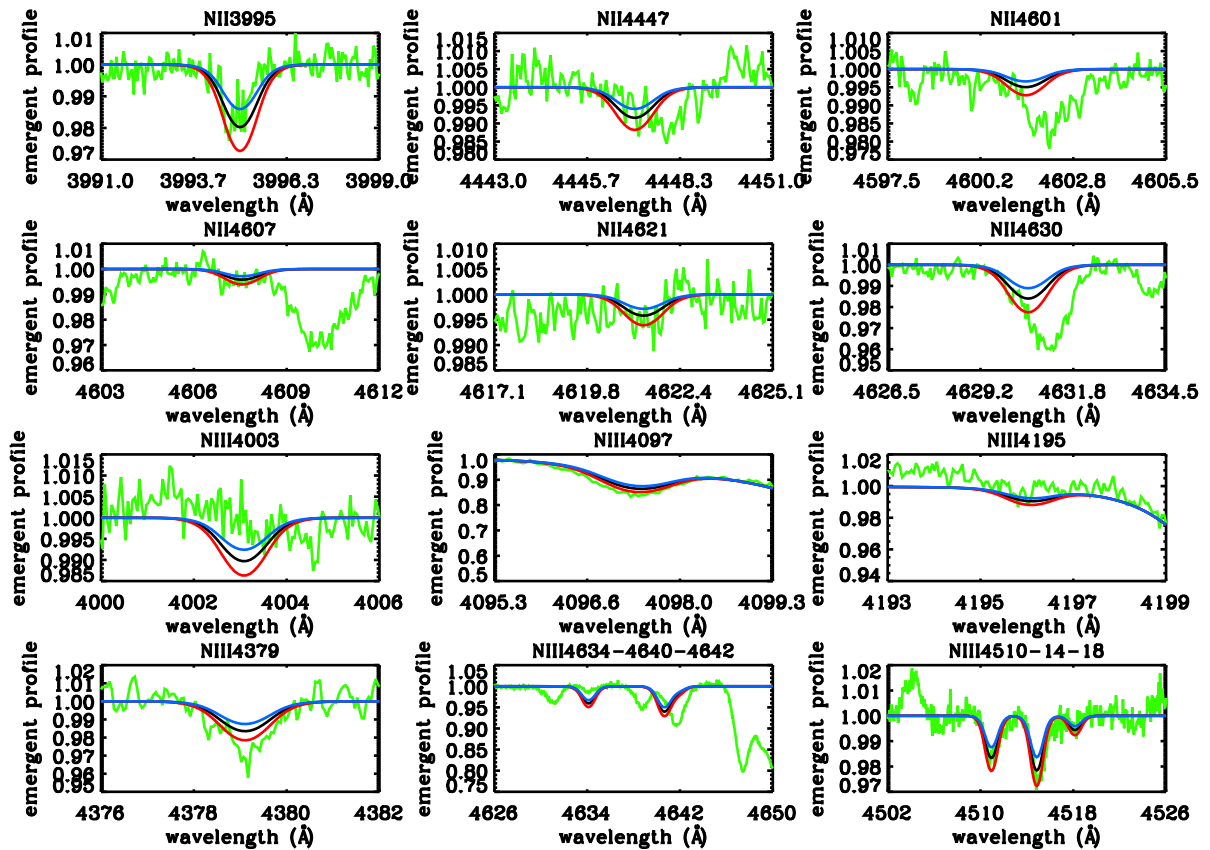


Fig. C.1. N11-029 – O9.7 Ib. Observed (green) and best-fitting optical nitrogen spectrum (black). Blue and red spectra correspond to synthetic line profiles with [N] at the lower and upper limit, respectively. For details, see Sect. 5.

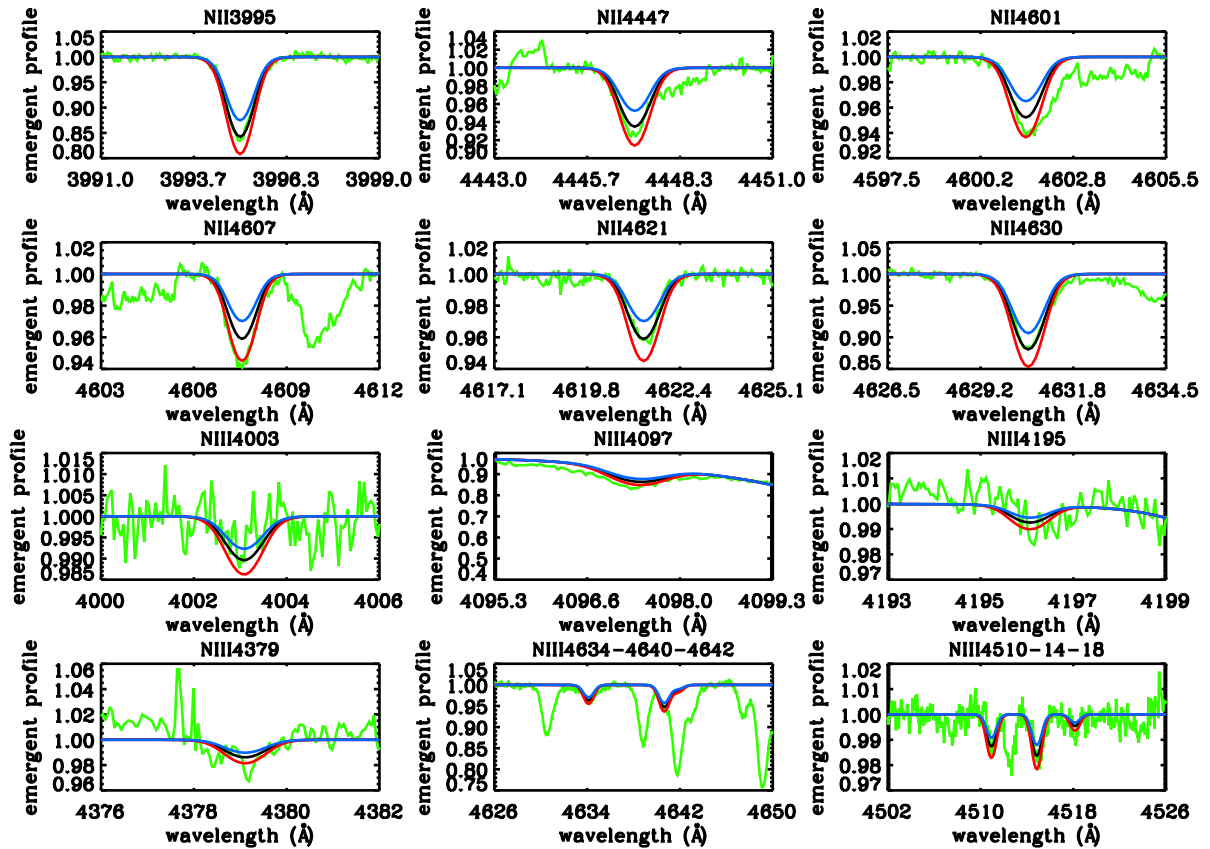


Fig. C.2. N11-036 – B0.5 Ib

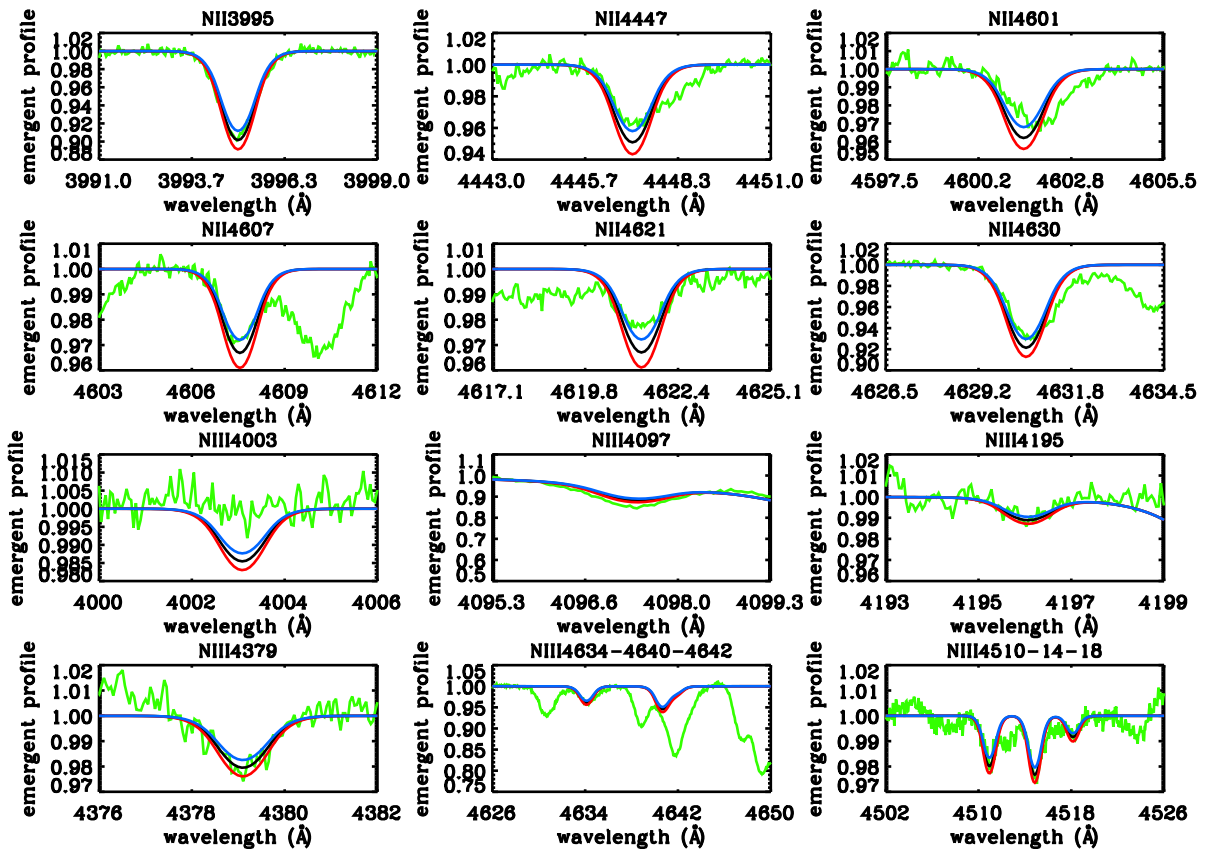


Fig. C.3. N11-008 – B0.7 Ia

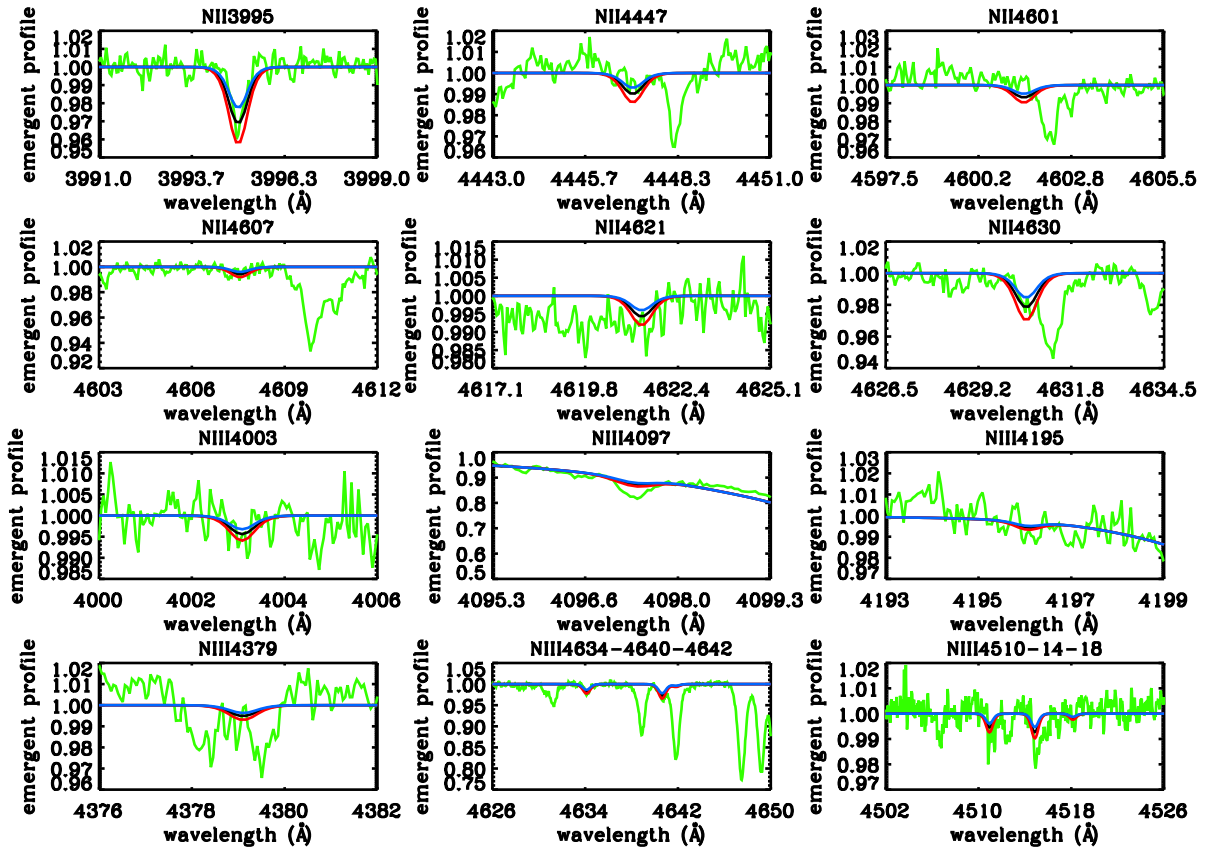


Fig. C.4. N11-042 – B0 III

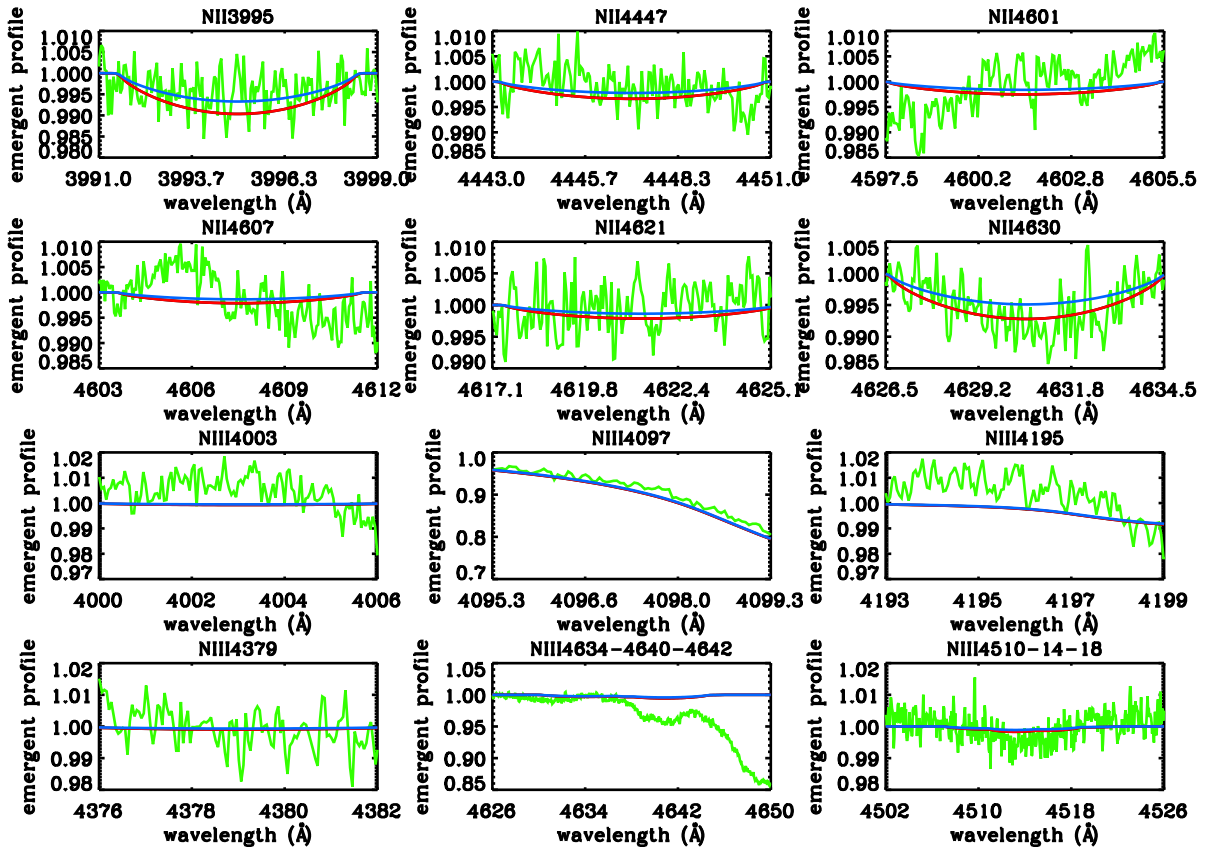


Fig. C.5. N11-033 – B0 IIIIn

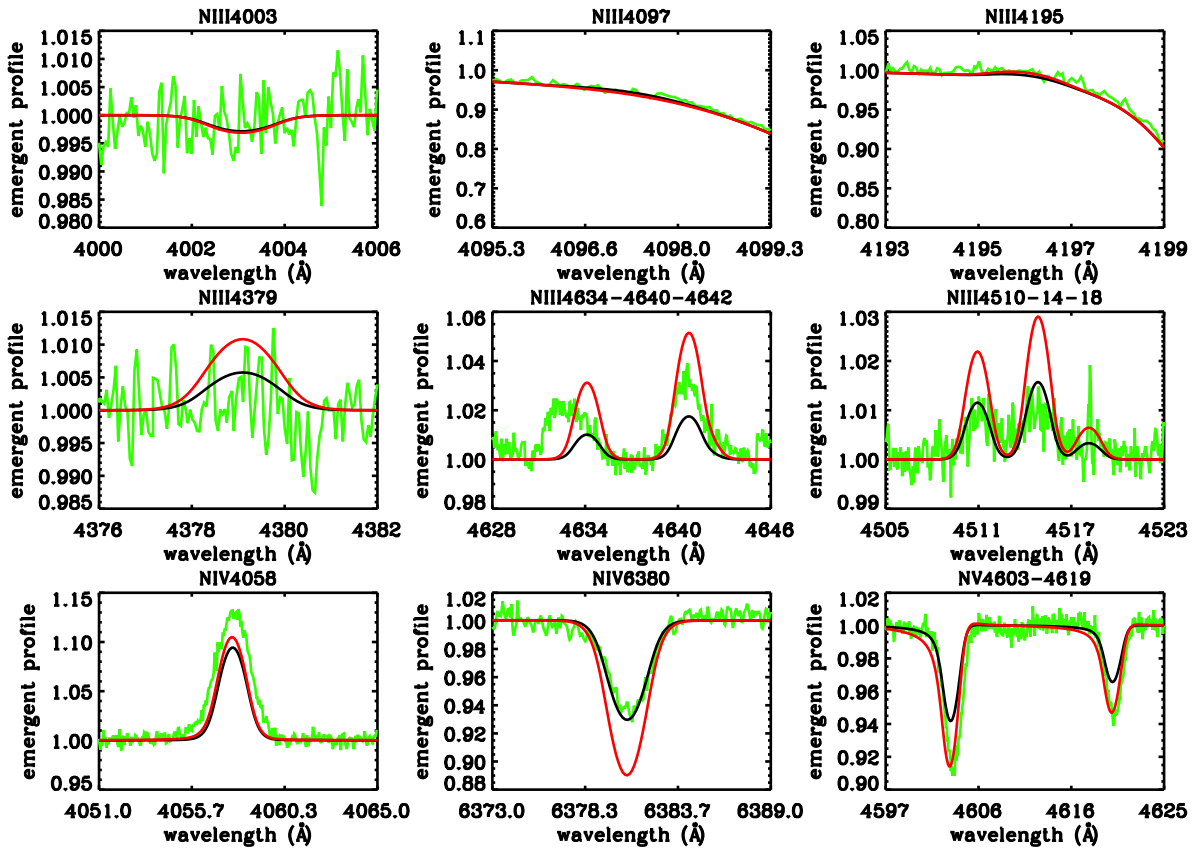


Fig. C.6. N11-026 – O2 III(f*)

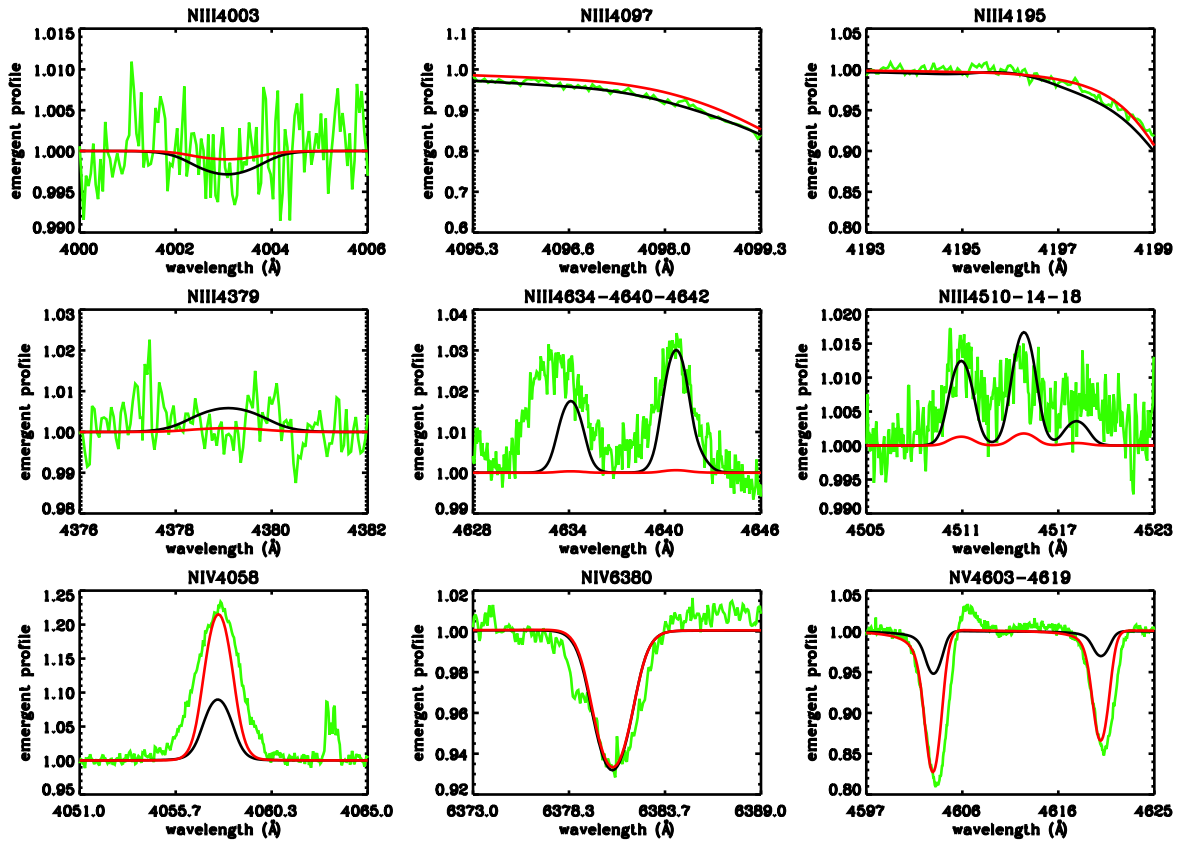


Fig. C.7. N11-031 – ON2 III(f^{*}). Black: cooler solution, supported by He I λ 4471, N III and N IV λ 6380. Red: hotter solution, supported by the N IV/N V lines (see Sect. 5).

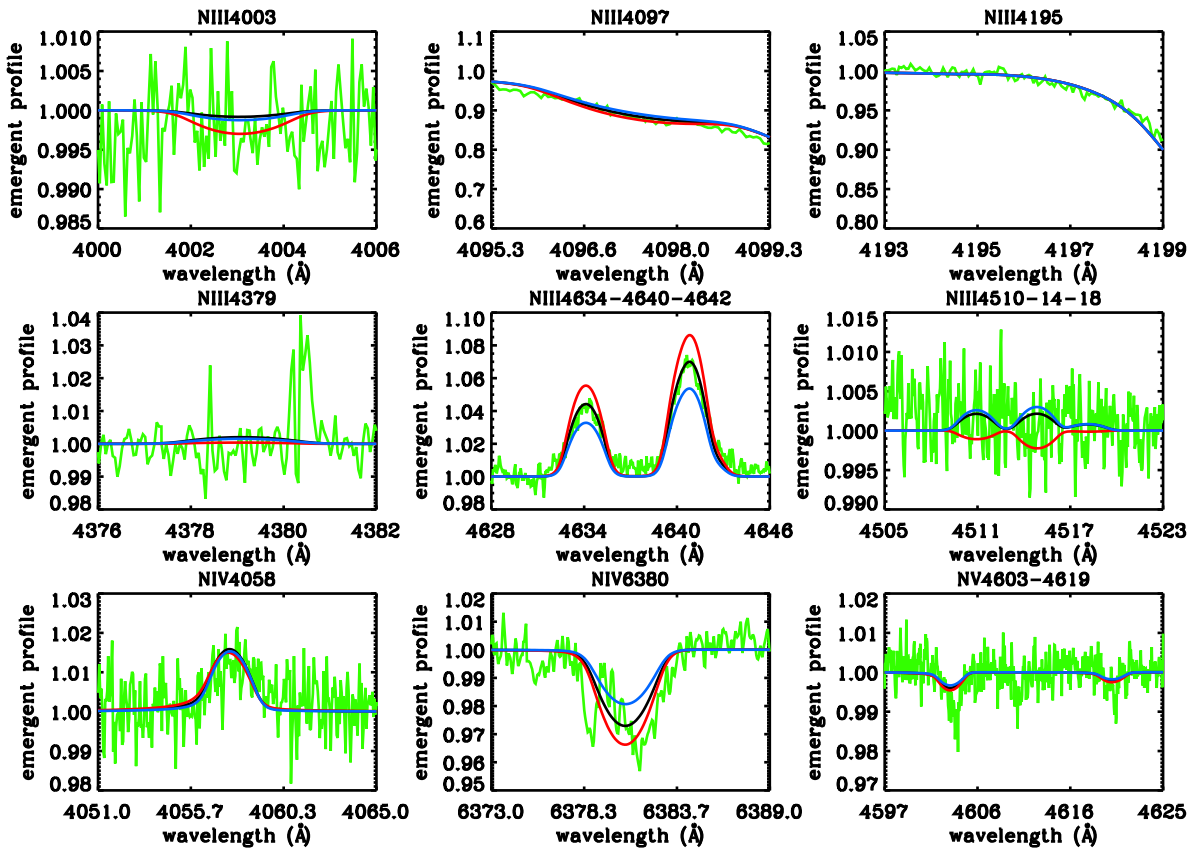


Fig. C.8. N11-038 – O5 II(f⁺)

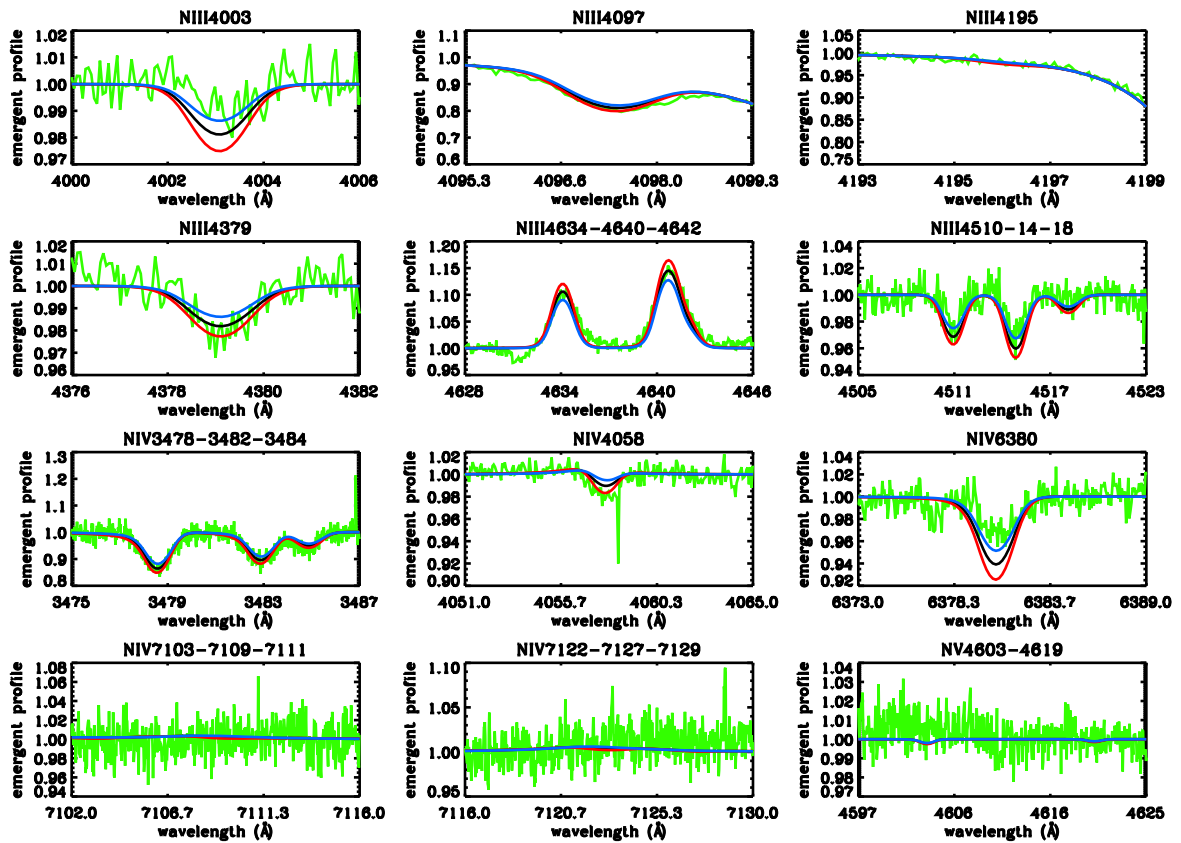


Fig. C.9. Sk-66° 100 – O6 II(f)

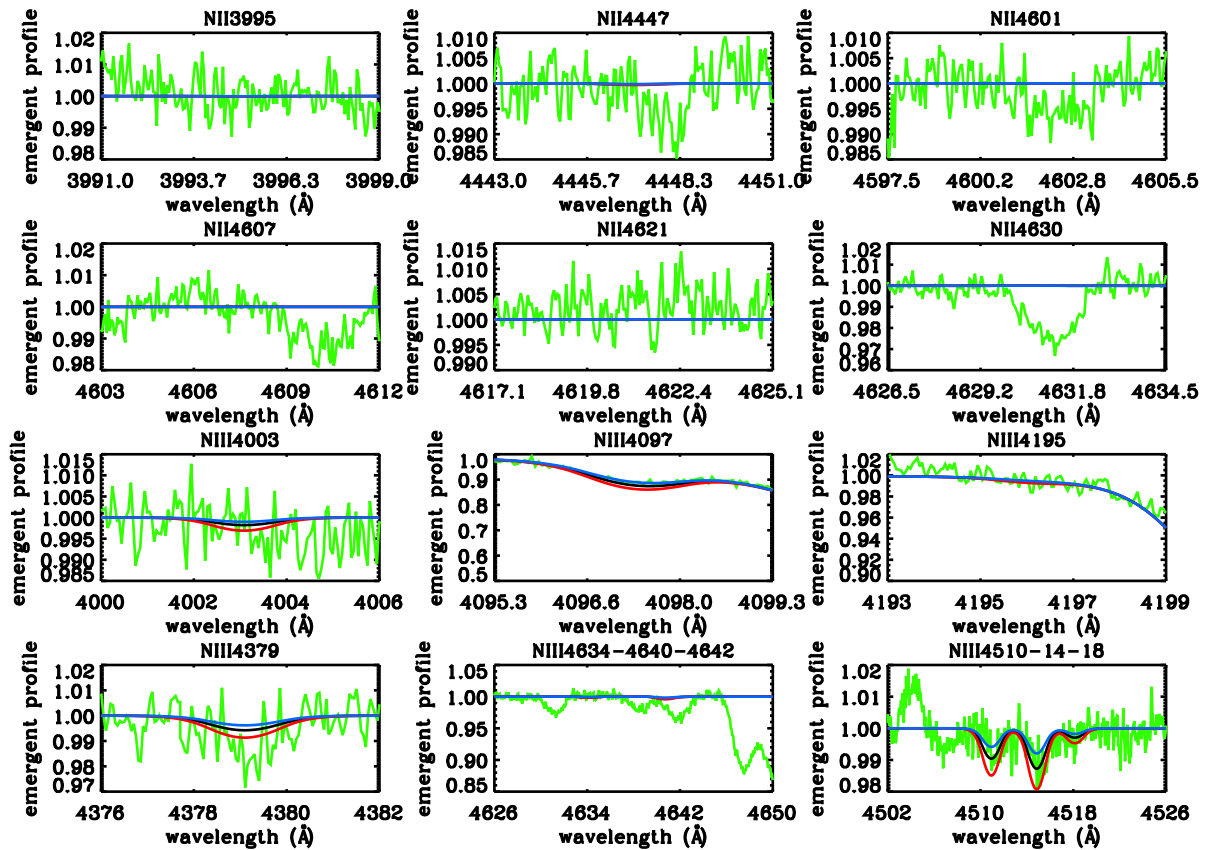


Fig. C.10. N11-045 – O9 III

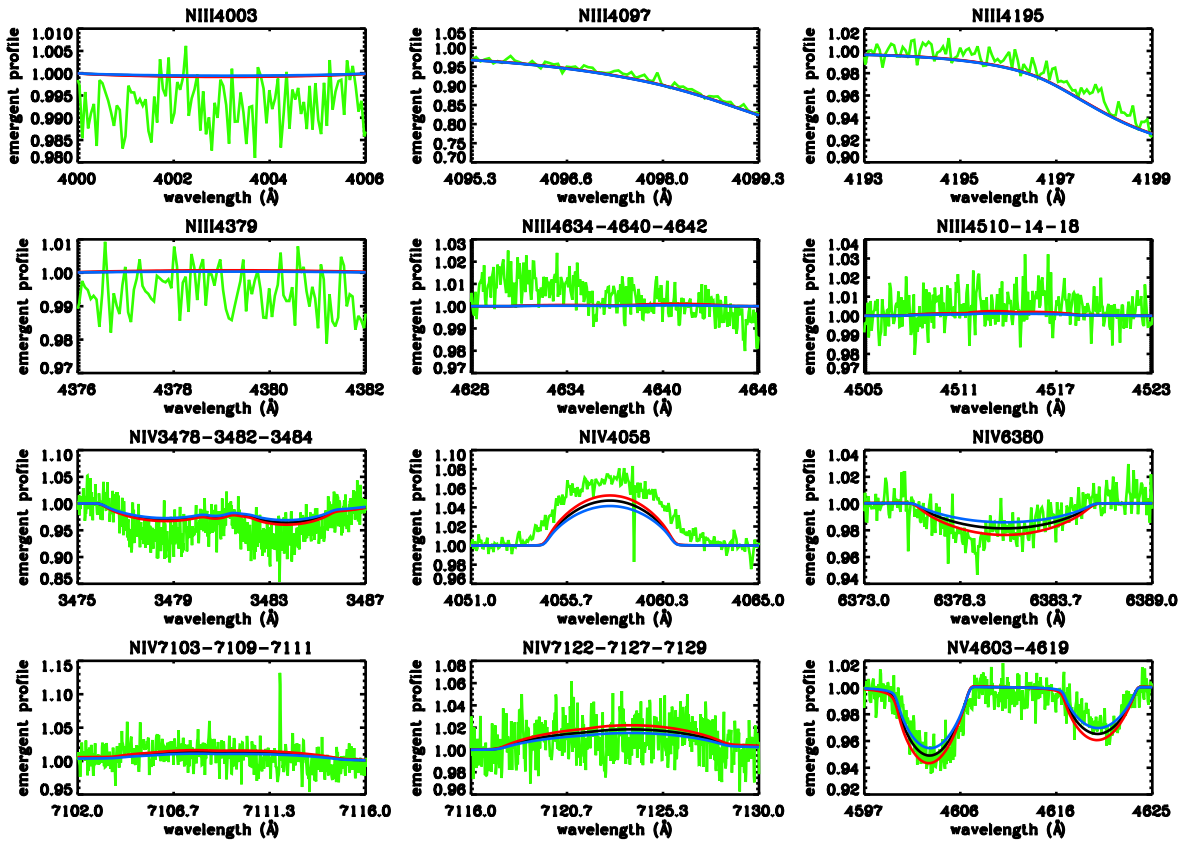


Fig. C.11. BI253 – O2 V((f*))

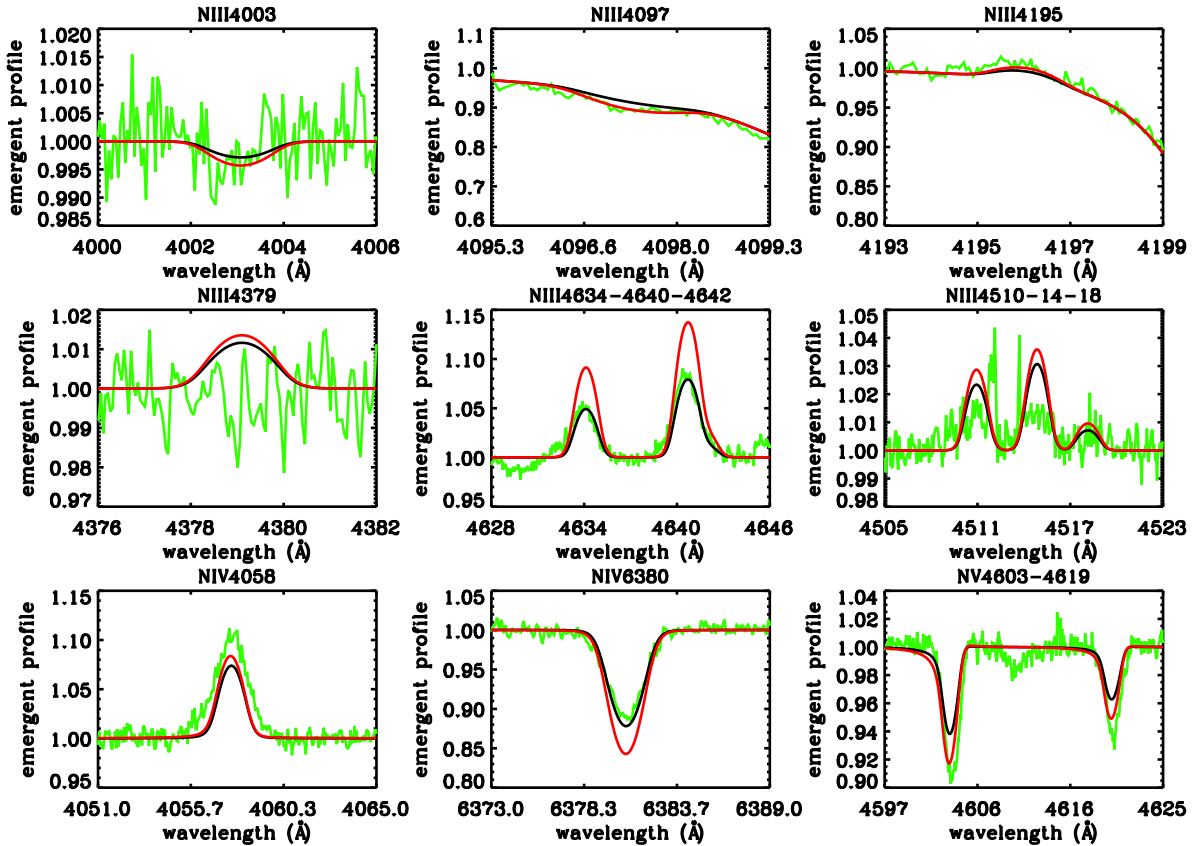


Fig. C.12. N11-060 – O3 V((f*))

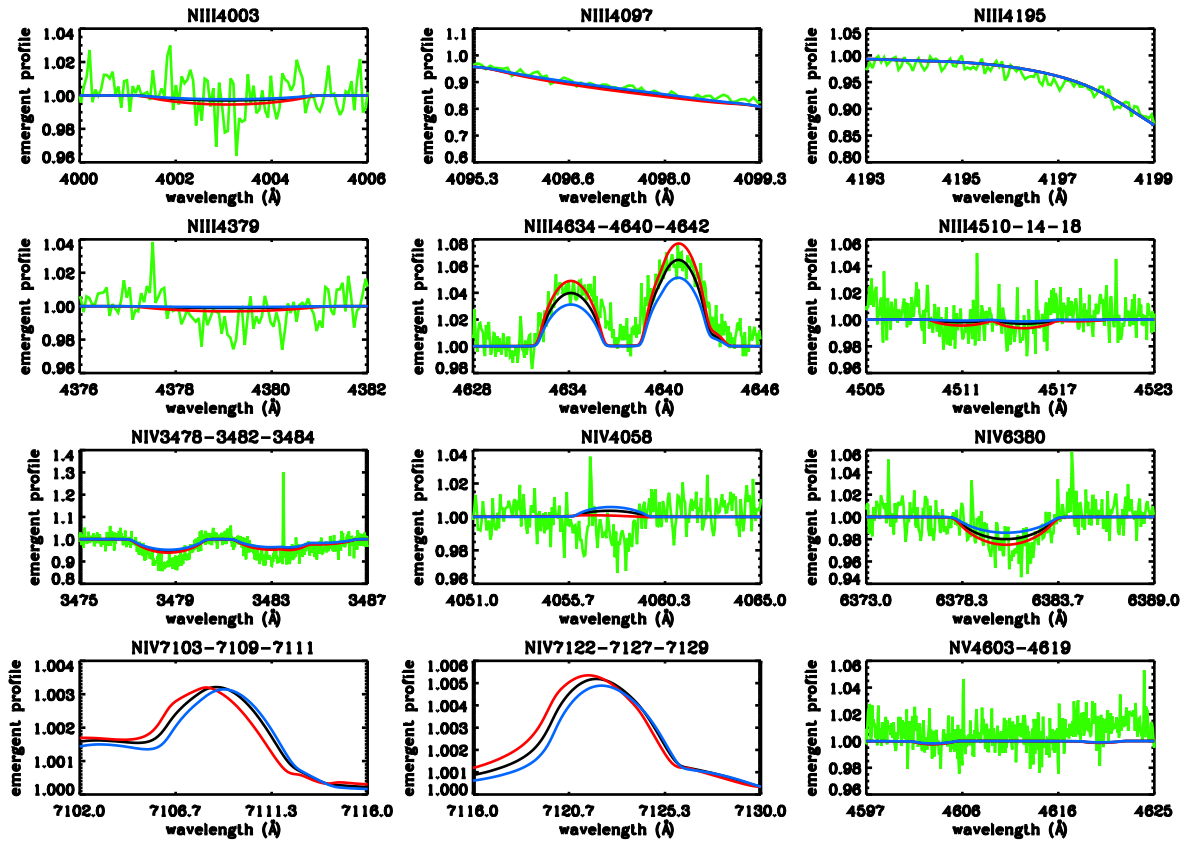


Fig. C.13. Sk-70° 69 – O5 V((f)). For this star, the N iv multiplet at 7103-7129 Å has not been observed.

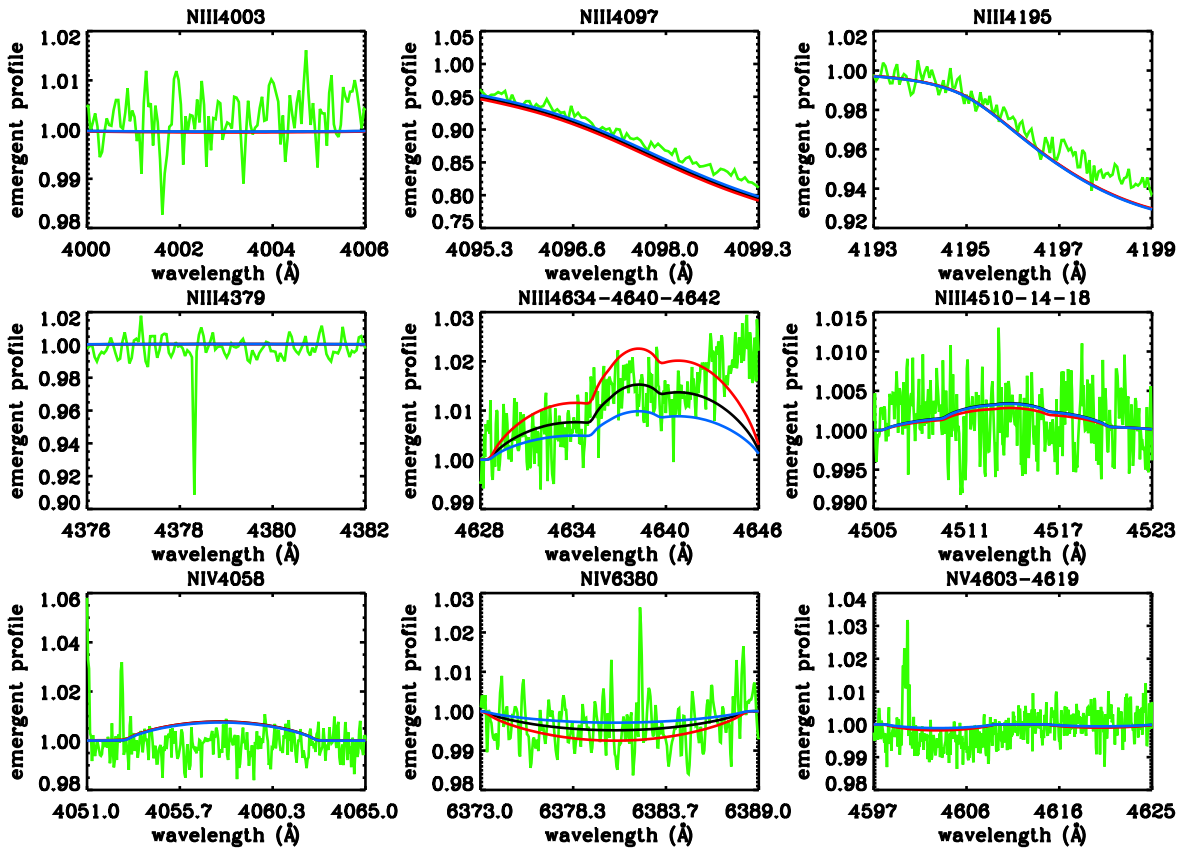


Fig. C.14. N11-051 – O5 Vn((f))

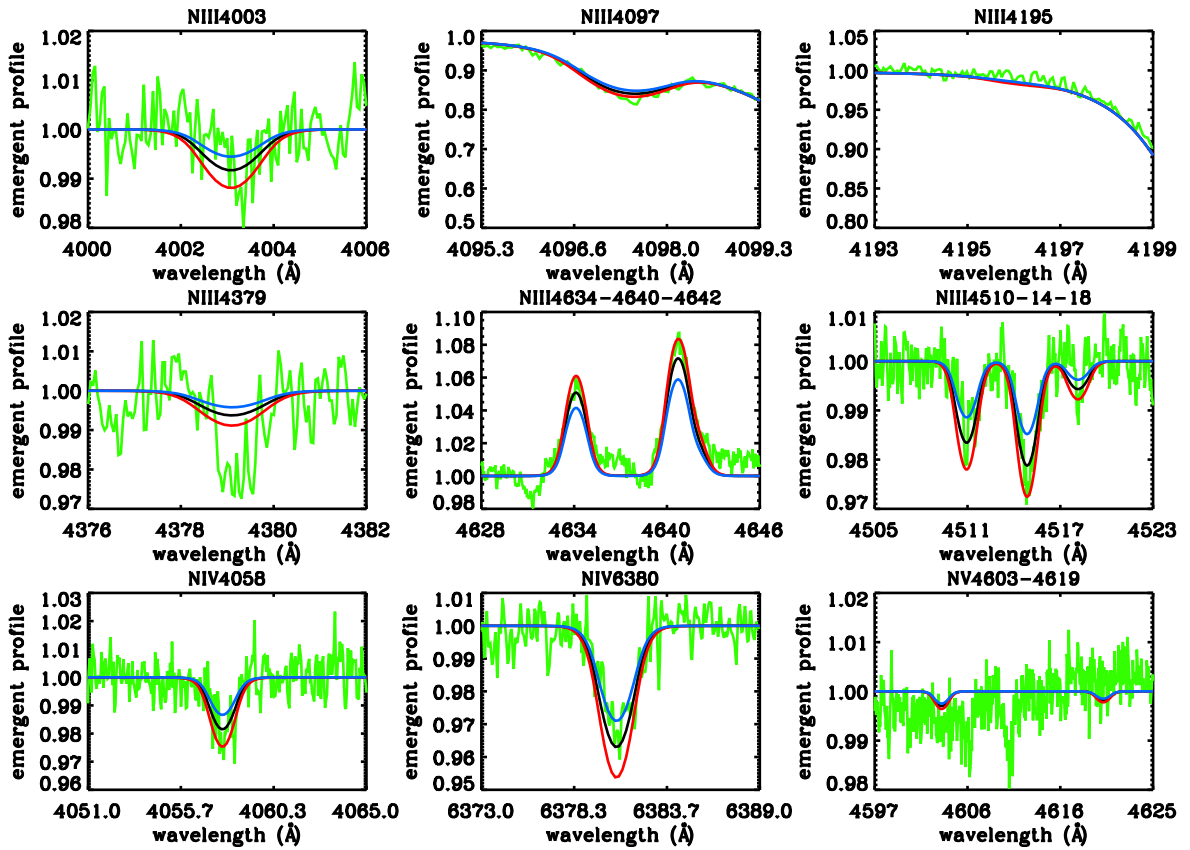


Fig. C.15. N11-058 – O5.5 V((f))

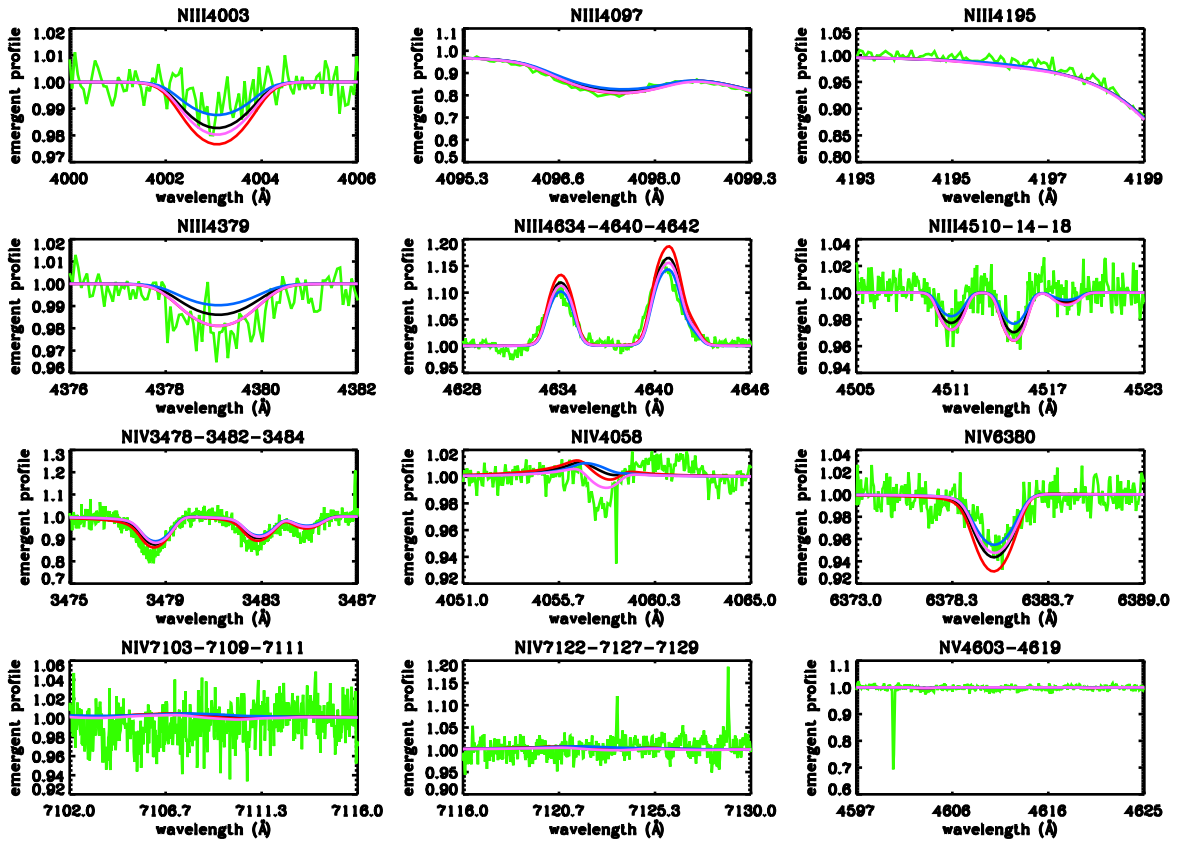


Fig. C.16. Sk-66° 18 – O6 V((f)). Magenta spectra correspond to a weakly clumped model. For details, see Sect. 5.

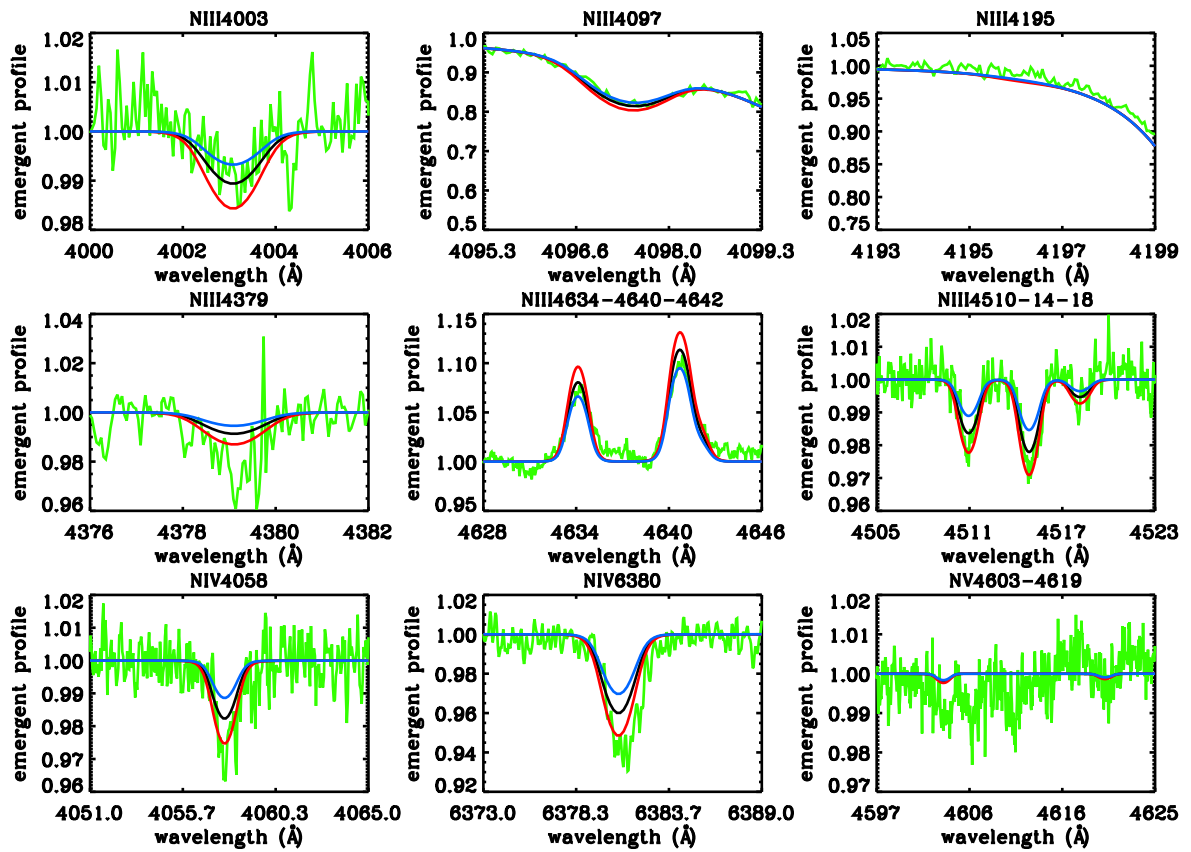


Fig. C.17. N11-065 – O6.5 V((f))

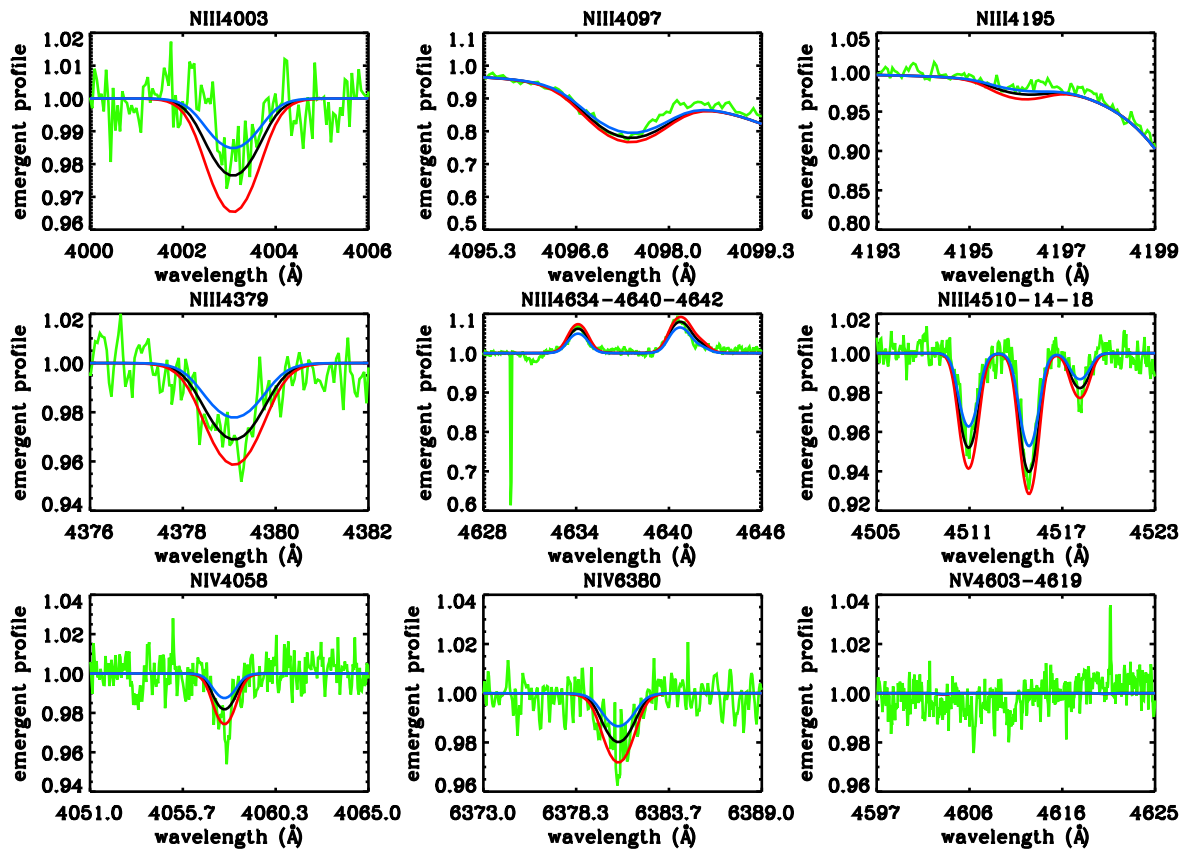


Fig. C.18. N11-066 – O7 V((f))

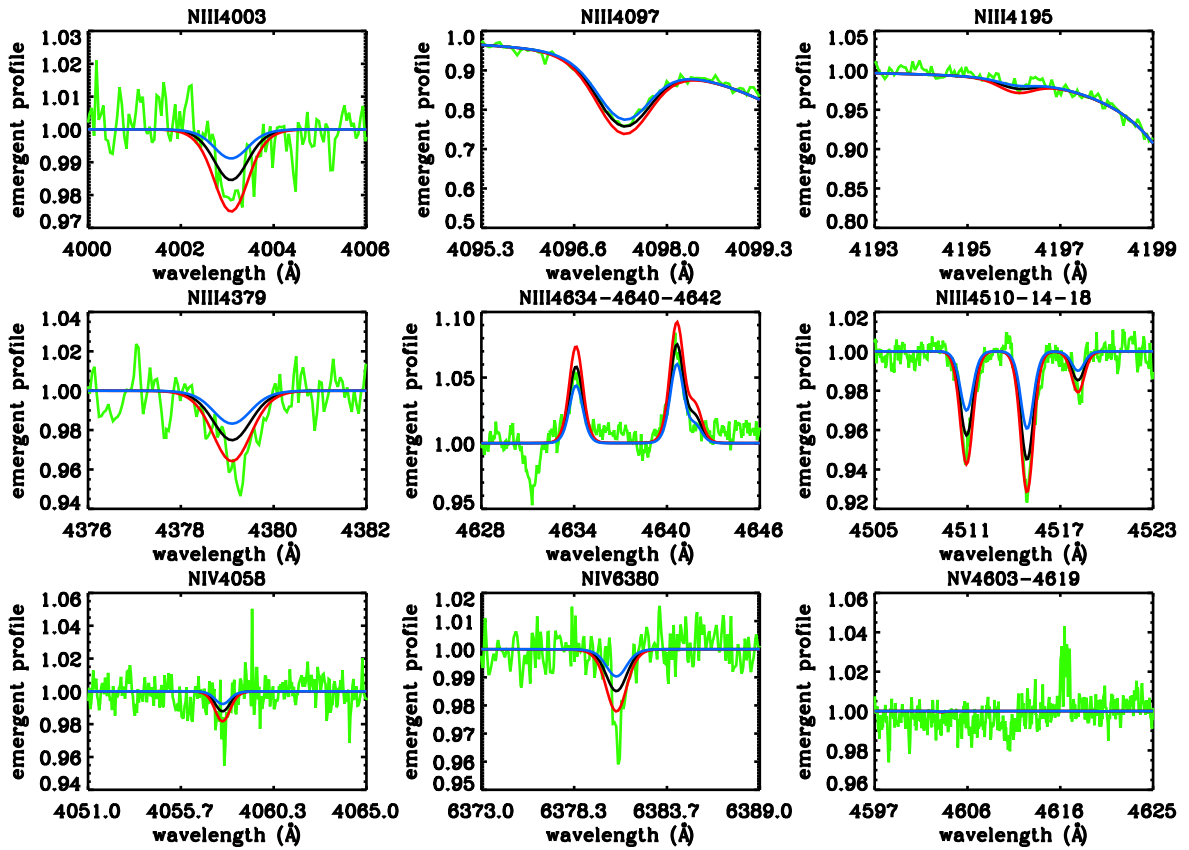


Fig. C.19. N11-068 – O7 V(f)

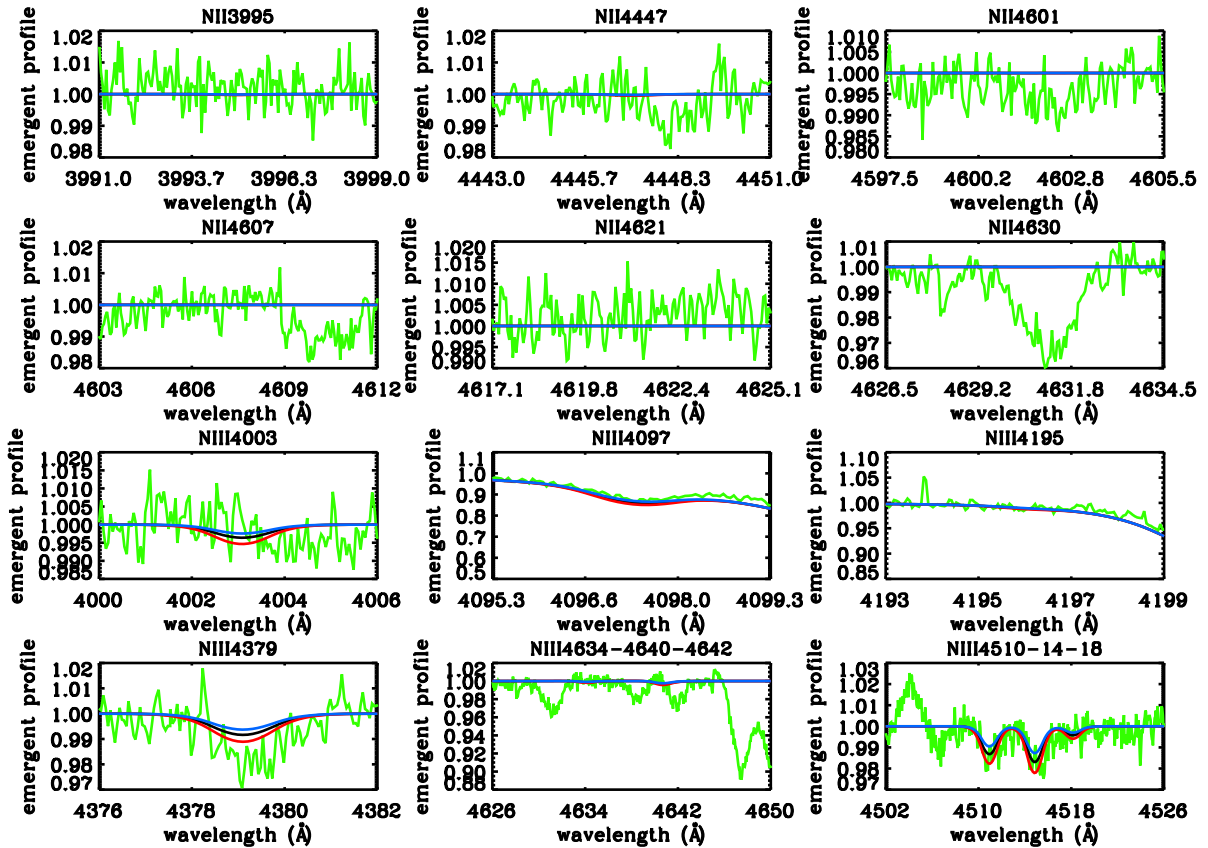


Fig. C.20. N11-061 – O9 V

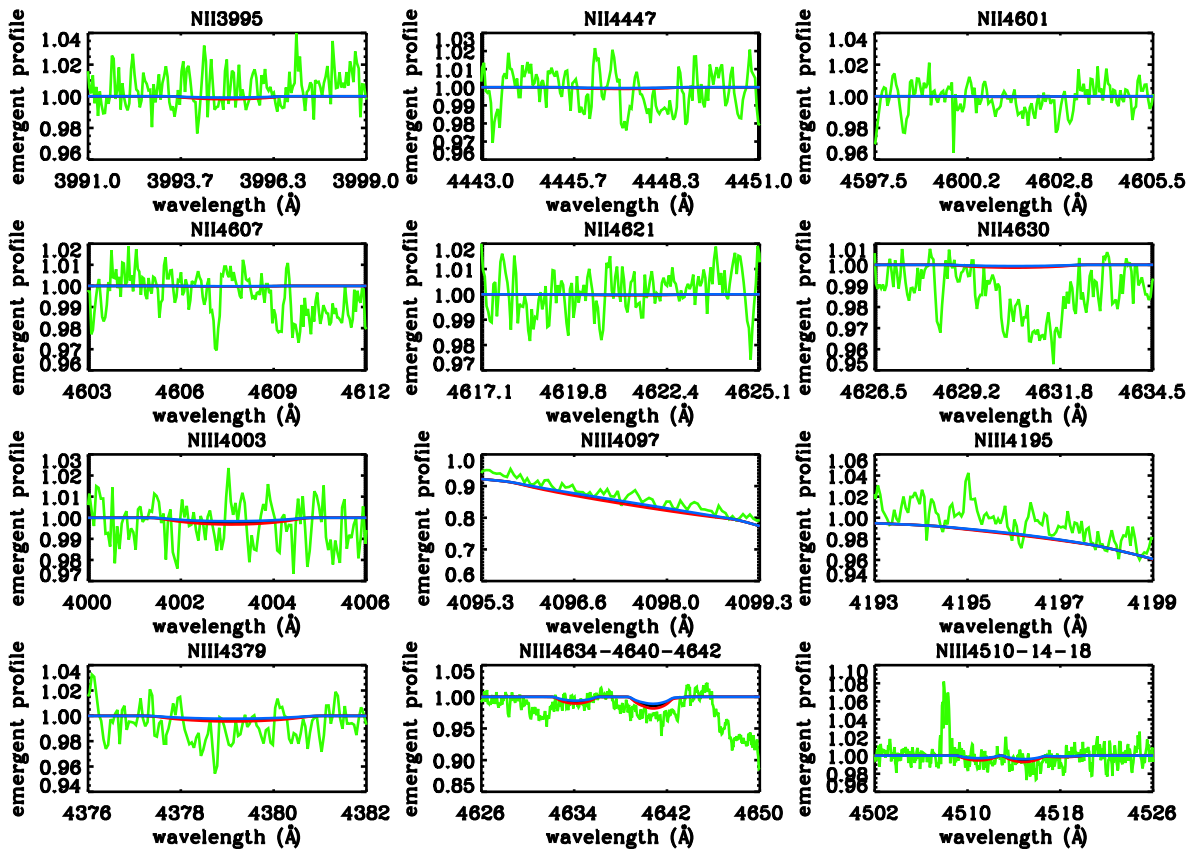


Fig. C.21. N11-123 – O9.5 V

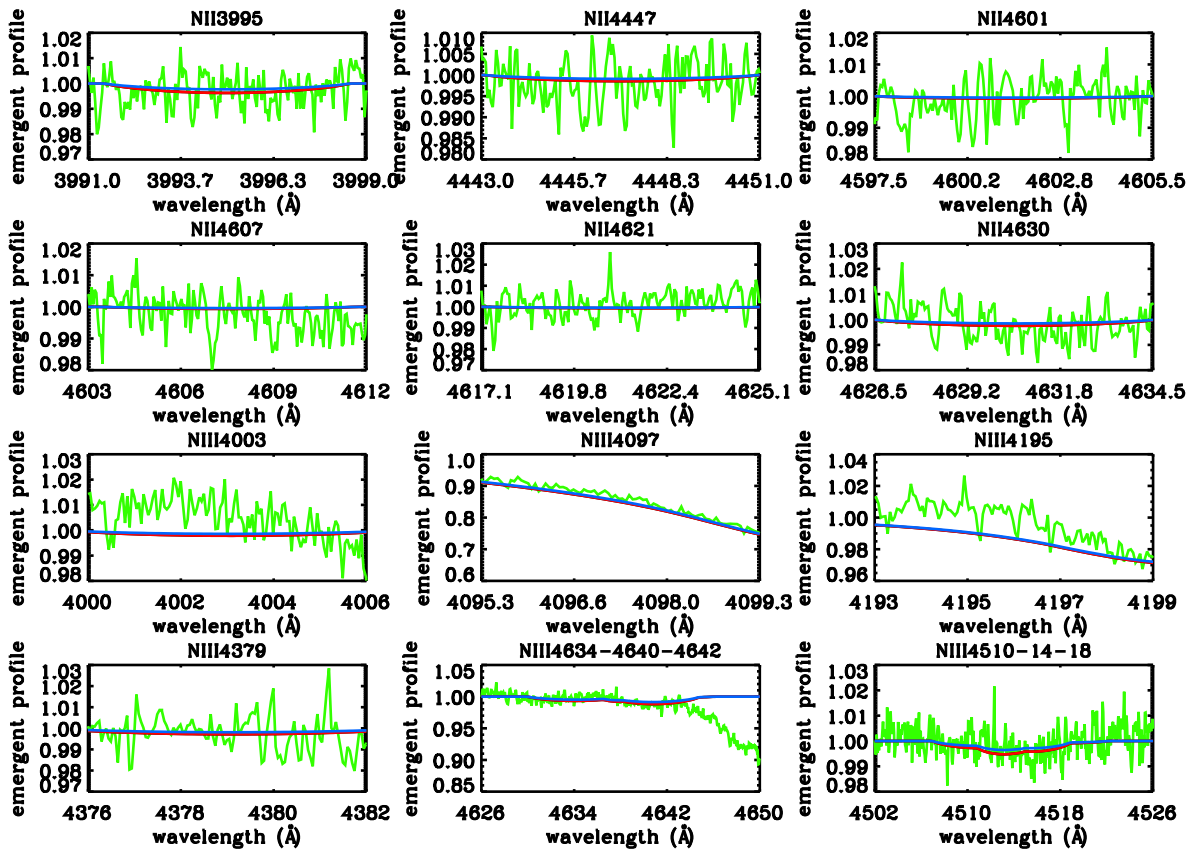


Fig. C.22. N11-087 – O9.5 Vn